Tuning structure and electronic properties of 2D materials by ion-beam irradiation

ZHAO, Yangzhou

(開始ページ / Start Page)
1
(終了ページ / End Page)
142
(発行年 / Year)
2024-03-24
(学位授与番号 / Degree Number)
32675甲第605号
(学位授与年月日 / Date of Granted)
2024-03-24
(学位名 / Degree Name)
博士(理工学)
(学位授与機関 / Degree Grantor)
法政大学 (Hosei University)
(URL)
https://doi.org/10.15002/00030500

Doctoral Dissertation Reviewed by
Hosei University

Tuning structure and electronic properties of 2D materials by ion-beam irradiation

ZHAO Yangzhou

Content

Chapter 1 Introduction

1.1 Two-dimensional (2D) materials

Two-dimensional (2D) or monolayer materials refer to a class of nanomaterials that consist of a single layer of atoms and have a 2D sheet lattice structure in which atoms are arranged on a plane, such as graphene, transition metal dichalcogenides (TMDs), silicene, and phosphorene, which have attracted considerable attention in the fields of physics, chemistry, materials science, and engineering in recent years. In 2D materials, atoms inside each layer are bonded by covalent bonds, and the layers are combined via a van der Waals-like force. This structural feature allows the isolation of 2D materials such as graphene sheets into an individual monolayer of graphite via the Scotch-tape exfoliation method, which is used to initially fabricate graphene [1].

Two-dimensional materials exhibit several advantageous properties such as layered structure with honeycomb lattice, presence of multiple constituent elements, and photo absorption capabilities [2]. These materials exhibit various electronic structures, such as zero-gap conductor (graphene), semiconductor, and metallic structures, as shown in Fig. 1.1. Owing to the unique properties derived from their 2D structure, these materials can be used in various applications. Two-dimensional materials such as MoS_2 or graphene are some of the most promising materials for next-generation devices owing to their strong material hardness, significant heat conduction, charge transfer, and impressive electronic properties.

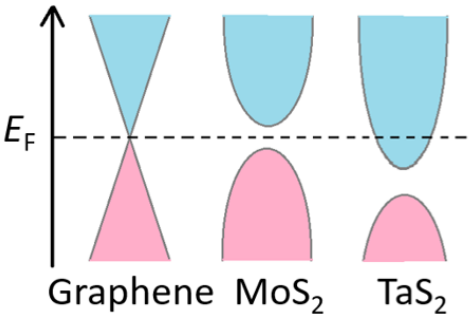

Fig.1.1 Electronic structure of Two-dimensional (2D) materials including graphene, MoS_2, and TaS_2

1.2 Graphene

Graphene is one of the most famous 2D materials and is an allotrope of carbon with only one-carbon-atom thickness, that is, it consists of a single layer of carbon atoms that arranged in a honeycomb lattice structure formed by sp^2 bonds of carbon atoms. It can be fabricated by three-dimensionally stacking sheets formed by countless carbon atoms bonded in a hexagonal mesh. In 2004, Geim et al. discovered that single-layer (1L) graphene can be easily obtained by mechanically cleaving and exfoliating bulk graphite using a Scotch tape, which is described subsequently [3].

Graphene has superior properties such as high electron mobility, thermal conductivity, mechanical flexibility, and chemical stability, and is expected to be applied to next-generation semiconductors and high-sensitivity sensors. Graphene has a peculiar electronic band structure as double cone as shown in Fig. 1.2. At the contact point, the valence and conduction bands do not overlap and the density of the electronic states is zero [4]; therefore, graphene is called a “zero-gap semiconductor.”

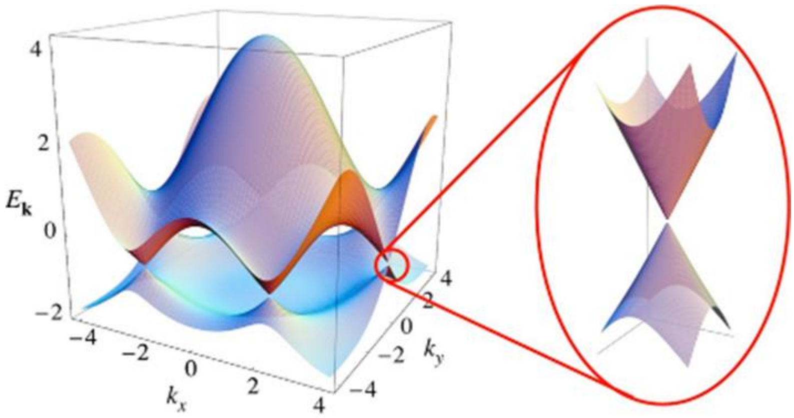

Fig. 1.2 Electronic structure of graphene [4]

Graphene is one of the strongest materials that has been found. The strength and stability of graphene results from its tough lattice and sp^2 hybridization, where the electrons of s, p_x, and p_y orbitals consist of the σ-bond, while the remaining electron of p_z orbital makes up the π-bond. The π-bond of the valence band and the π^*-band of the conduction band are contact at -4.6 eV from the vacuum, exhibits a metallic conductivity because of the free electrons inside the band. Additionally, the introduction of guest species of graphene can easily modify its electrical properties by modulating the Fermi energy with adsorbed donor or acceptor. The charge also affects its carrier mobility by coulomb scattering [3].

The hexagon lattice of graphene can be treated as a triangular Bravias lattice with two carbon atoms A and B per unit cell. In this case, graphene comprises two sublattices A and B with basis vectors ($\mathbf{a}_1$, $\mathbf{a}_2$) as shown in Fig. 1.3(a). At the corner of the Brillouin zone in the reciprocal lattice of graphene, two inequivalent points exist, which are named K and K' and are known as Dirac points (Fig. 1.3(b)), where the valence band and conduction band contact each other without a gap [4].

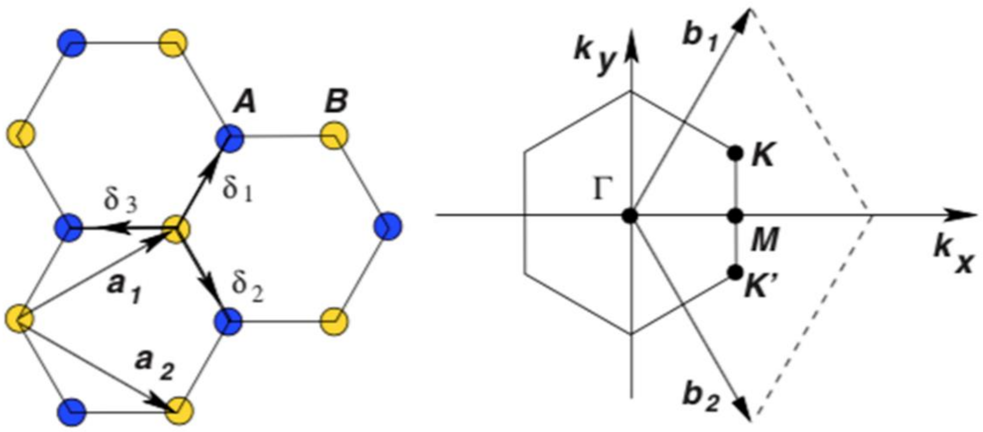

Fig. 1.3 (a) Graphene lattice structure with two atoms per unit cell;
(b) Reciprocal lattice spanned by b_1, b_2 and the first Brillouin zone (hexagon) with Dirac points K and K' [4]

1.3 Transition metal dichalcogenides

TMDs are compounds of transition metals and chalcogen elements. They are generally expressed as MX_2 (M: transition metal (Ti, V, Cr, Mn, Fe, Co, Ni, Zr, Nb, Mo, Tc, Ru, Rh, Pd, Hf, Ta, W, Re, Os, Ir, Pt); X: chalcogen (S, Se, Te)). Nearly 60 types of TMDs exist, and approximately two-thirds of them have a layered structure, which implies that they can be easily exfoliated as monolayer materials. TMDs have been receiving considerable attention because of their promising mechanical, electronic, and optical performance [5].

These monolayer TMDs have a 1L structure formed in a sandwich-like layout of X-M-X, and the layers in a bulk crystal are loosely connected by the van der Waals force. Furthermore, as the stacking of layers and physical properties vary depending on the combination of M and X, materials with various functionalities can be developed. Among TMDs, MoS_2 and TaS_2, which are compounds of the transition metals Mo and Ta, respectively, and the chalcogen element S, exhibit several advantageous physical and electrical properties. These materials have attracted attention as they exhibit superior conductivity and magnetism, and are expected to be applied in the fields of semiconductors, superconductors, and thermoelectric conversion devices.

1.3.1 MoS_2

MoS_2, a representative TMD, is a kind of famous solid lubricant owing to its layered structure. Recently, MoS_2 has attracted considerable scientific and engineering interest in the field of 2D materials because of its easy exfoliation from natural crystals. MoS_2 is a semiconductor composed of layered TMDs with a broad range of electronic, optical, mechanical, and thermal properties. It is a promising channel material for fabricating field-effect transistors (FETs) [6]. Two-dimensional materials, such as 1L-MoS_2 or its stacking structure of two, three layers (referred to as 2L- and 3L-MoS_2, respectively), have received significant attention in recent years owing to the 2D nature of the crystal lattice and electronic structure and the significantly high specific surface area [2]. In fact, when compared to bulk MoS_2 (which has an indirect bandgap), 1L-MoS_2 has a direct bandgap in its electronic band structure, and larger specific surface area; consequently, the electronic properties are significantly affected by molecular adsorption and the number of layers [7].

Fig. 1.4 shows the change in bandgap in MoS_2 caused by the number of layers [8]. The band structure of MoS_2 with different layers (4L, 3L, 2L, and 1L from the left of the figure) are shown, and the arrows in the figure indicate the direction of electronic transition. The energy level at the Γ point changes depending on the number of layers, but the energy level at the K point does not change. Therefore, MoS_2 is changed from an indirect- to a direct-bandgap semiconductor with a decrease in dimensionality (Fig. 1.4). Owing to this change in electronic structure, in addition to the general quantum confinement effect, monolayer MoS_2 characteristically exhibits enhanced photoluminescence (PL) originating from direct transitions when compared to multilayer ones.

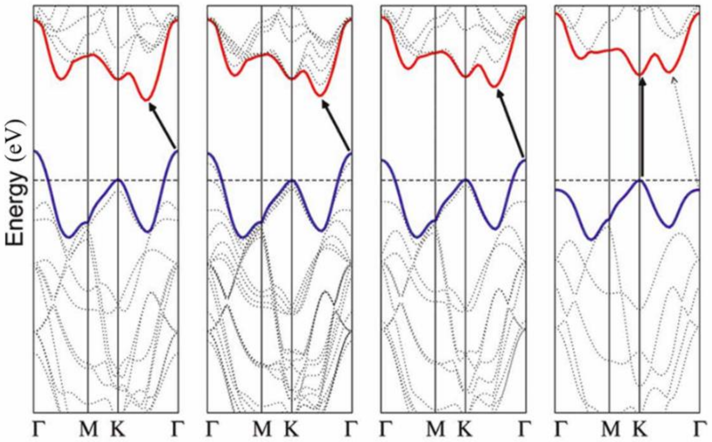

Fig. 1.4 Variations in the bandgap in MoS_2 sheet [8]

Various types of 2D devices, including FETs and light sensors, can be fabricated using 1L-MoS_2, which exhibits a significant advantage over graphene as a zero-gap semiconductor, owing to its bandgap [9]. Because of the large direct bandgap in electronic structure of 1L-MoS_2, the probability of photon absorption and release is significantly higher than those in indirect-bandgap semiconductor materials including multilayered MoS_2. Owing to this property, 1L-MoS_2 is highly suitable for optoelectronic devices such as photo detectors or light sources.

Conversely, 1L-MoS_2 exhibits another feature, that is, valley-selective polarization, which may result in its future application in the field of valley-based electronics and optoelectronics [10].

1.3.2 TaS_2

TaS_2 is a layered TMD, which has gained significant attention in the fields of material science. Its structure is characterized by layers of Ta atoms sandwiched between S atoms, and these layers are weakly combined by van der Waals forces, which is similar to the case of MoS_2, allowing for easy exfoliation [11].

TaS_2 can exhibit different electrical conductivities and exist as a conductor, semiconductor, or superconductor depending on its phase and temperature. It has several phase transitions at different temperatures that are associated with changes in its crystal structure, which significantly affects its electronic properties. Owing to these properties, TaS_2 exhibits potential in applications such as sensing and storage devices.

Several research groups have confirmed that TaS_2 has multiple charge density waves (CDWs) that vary depending on temperature; moreover, unprecedented modulation of optical properties is expected because of the generation of structural defects through annealing and adsorption of gas molecules [12].

1.4 Fabrication of 2D materials

Previously, researchers believed that 2D materials could not exist in the ambient conditions because of its instability. However, a group led by A.K. Geim of the University of Manchester successfully prepared a new 2D monolayer carbon material known as graphene in 2004, achieving the novel fabrication of a 2D material through a mechanical exfoliation method [1].

Since the isolation of graphene, a wide variety of other 2D materials have been discovered and studied such as TMDs. In general, 2D materials are fabricated via two methods: exfoliation of a monolayer from bulk crystal or growth on a substrate via thin-film-synthesis methods such as chemical vapor deposition (CVD) or physical vapor deposition.

1.4.1 Mechanical exfoliation

Monolayer 2D materials are usually fabricated using a typical technique called “Scotch-tape method,” in which a tape is used to peel off a few-layer flakes from a bulk crystal. As the interlayer van der Waals force in graphite is significantly weak, only a few layers can be easily exfoliated from crystals of these materials using the adhesive tape. For example, in the fabrication process of graphene, highly oriented pyrolytic graphite (HOPG) is exfoliated using a Scotch tape, and repeatedly dilacerated for around 5 times. Thus, few-layer graphene with a fresh surface can be obtained on the tape, and many pieces of graphene flakes can be transferred to the substrate surface by pressing this tape to the Si substrate surface. The number of exfoliations should be optimized as a parameter based on the exact experimental condition.

By using a Si substrate having a specific SiO_2 surface layer, even a 1L-graphene can be distinguished via an optical microscopic image [13]. Mechanical exfoliation is a relatively rapid and convenient method to obtain a high-quality monolayer sample, which is widely used in the study of 2D materials; therefore, it was chosen as the fabricating method in this study.

1.4.2 Chemical vapor deposition

In the CVD method, a type of solid reactive substance is created by supplying a raw material in a gaseous state and reacting it with a substance placed on a substrate such as Cu plate or SiO_2/Si on the solid surface. The monolayer sample is typically fabricated in a specially designed reactor or chamber in a condition where the gas flow, temperature, and pressure are accurately controlled. Both graphene [14] and MoS_2 [15] can be prepared using CVD at specific conditions. CVD is used to produce solid materials with high purity and quality, and is extensively utilized in the semiconductor manufacture industry for the production of thin films, and is also widely used in the study related to 2D materials for sample fabrication.

1.5 Characterization methods for 2D materials

1.5.1 Layer number evaluation via optical microscopy

When samples are prepared via mechanical exfoliation, in addition to monolayer samples, multilayer or bulk flakes also exist on the substrate. Thus, when the exfoliation method is used to obtain 2D material samples, optical microscopy (OM) and Raman spectroscopy are used to identify the monolayer samples.

Typically, the substrate is observed under an optical microscope to effectively identify the monolayer samples. Then, a digital camera that is adapted to the OM is used to capture photos with a red or green filter. OM images of 2D flake samples are used to evaluate the layer number by checking the difference in the brightness between the sample and substrate. The photos of samples captured in the red or green channel are first analyzed using an image processing software; then, the brightness contrast is determined, which can be compared with references paper to obtain the layer number [16][17].

OM is used to analyze a wide surface area in a short time. Although the thickness of graphene is only approximately 0.3 nm, it can be observed using an OM with clear contrast. However, the contrast varies depending on the thickness of the SiO_2 layer of the substrate, and it cannot be discriminated in visible light. Therefore, the contrast is considered to be affected by the interference effect of the reflected light. The thickness of the SiO_2 layer of the substrate must be precisely controlled, and by appropriately selecting the wavelength of the observation light, the number of layers of graphene can be accurately evaluated based on the correspondence between the OM image and layer number of graphene (Fig. 1.5) [13].

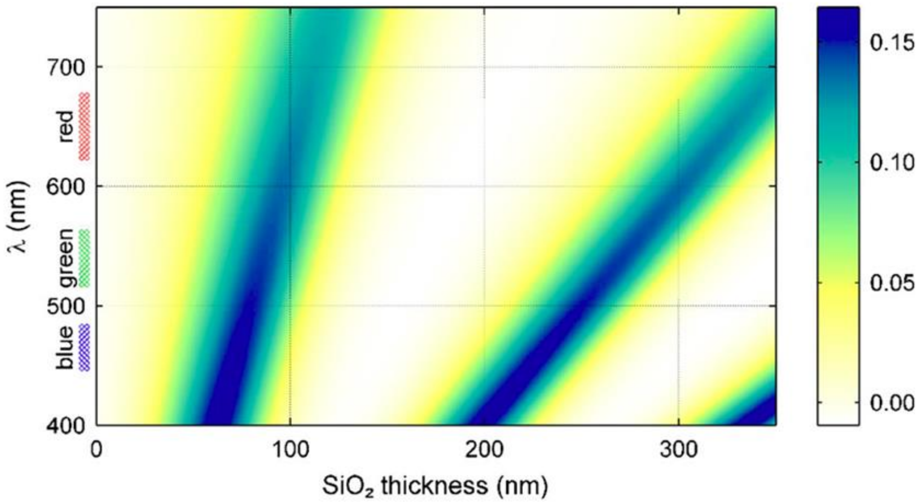

Fig. 1.5 Color plot of the contrast as a function of wavelength and SiO_2 thickness [13]

1.5.2 Raman spectroscopy

Raman spectroscopy is used to detect molecular vibrations by exposing a sample to strong monochromatic visible light and measures changes in the wavelength between the incident and Raman scattered light waves.

Usually, Rayleigh scattering occurs when the incident light is scattered by particles in a material, where the scattering light has the same wavelength as incident light owing to elastic scattering. However, a few photons can be scattered inelastically via Raman scattering, which indicates that the wavelength has changed because of the inelastic collision with the vibrating lattice.

When a laser is applied to a sample, the emitted scattered light is passed through a filter to remove the Rayleigh scattered light, and the Raman scattered light is transmitted to a detector to detect each wavelength. Then, the obtained signal is converted to a Raman shift value. The Raman scattered light contains frequency (wavenumber) information that changes depending on the molecular information of the sample, which aids in analyzing the other information such as crystallinity of the sample material [18].

1.5.2.1 Raman spectroscopy for Graphene

The typical bands in the Raman spectra of graphene are the G band and G' band. G band of 1L-graphene appearing around 1580 cm^{-1}, which is caused by the in-plane vibration of sp^2 carbon atoms. The G' band at approximately 2700 cm^{-1}, also known as the 2D band, which is a two-phonon resonance second-order Raman peak of D band, and indicates the interlayer stacking mode of carbon atoms in graphene. In the case of a disordered graphene sample or at the graphene sample edge, the D band (D stand for disorder) also appears at approximately 1350 cm^{-1} [19]. The specific frequencies of the G' and D bands are affected by the laser wavelength.

In 1L-graphene, the G' peak is sharp and symmetrical, and has a perfect single Lorentzian peak shape. Moreover, the G' peak intensity of 1L-graphene is greater than that of the G peak, as shown in Fig. 1.6 [20]. As the number of layers increases, the full width at half maximum (FWHM) of the G' peak gradually increases, associated with decreases in intensity and shifts to high wave numbers (blue shift) [21].

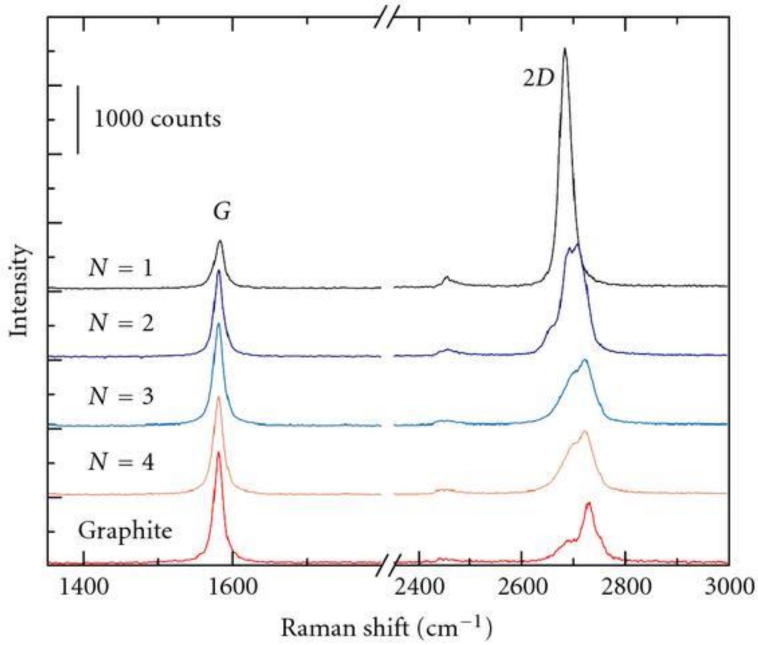

Fig. 1.6 Layer number dependence of Raman spectroscopy for graphene [20].

The G band is associated with the doubly degenerate (in-plane transverse optical (iTO) and longitudinal optical) phonon modes at the Brillouin zone center [18]. In fact, the G band is the only band occurring from first-order Raman scattering process in graphene, which is due to the selection rule related to the translational symmetry of crystalline materials. Conversely, the G' and D bands originate from second-order processes, involving two iTO phonons near the K point for the G' band and one iTO phonon and inter-valley carrier scattering by a defect potential for the D band [22]. This double-resonance mechanism is called an inter-valley process because it connects two adjacent points around inequivalent K and K' points in the first Brillouin zone of graphene (Fig. 1.7). In contrast, the D' band (~1620 cm^{-1}) is scattered from an intra-valley process that connects two points in the same double-cone at a K point (Fig. 1.7) [23]. Both the D and D' Raman bands appear because of the presence of inter- and intra-valley scattering of carriers by additional potentials of defects in graphene.

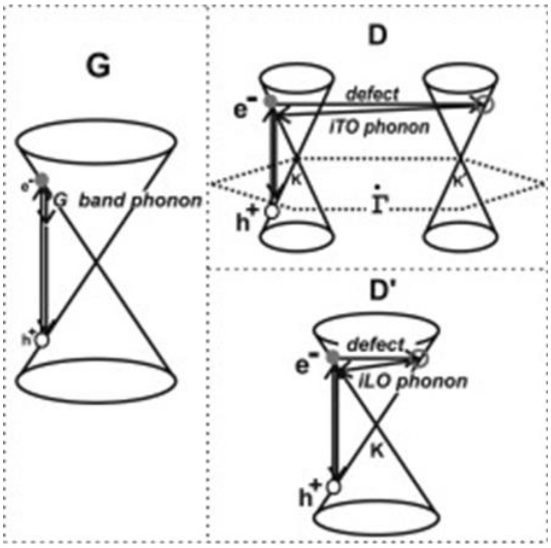

Fig. 1.7 Double-resonance mechanism of G, D, and D' bands [23]

Further, the G-band position and line width depend on the amount of carrier injected into graphene. The G-band position is determined to be around 1580 cm^{-1} by the Born-Oppenheimer approximation; however, a marginal shift due to carrier injection is explained by a correction term derived from the formation of a virtual electron-hole pair called Kohn anomaly (Fig. 1.8) [24]. When the lattice vibration energy of graphene is partially stabilized by the formation of electron-hole pairs, phonon softening occurs. As the excitation probability of an electron-hole pair varies depending on the position of the Fermi energy of graphene, the intrinsic energy of the G-band phonon depends on the Fermi energy (Fig. 1.9) [25]. The other factor that modulates the position of the G band is the charge of the force constant of carbon bonds. When the graphene honeycomb lattice is locally bent by the presence of defects or addition of functional groups, the reduction in the force constant results in a shift of G-band position toward a lower wavenumber.

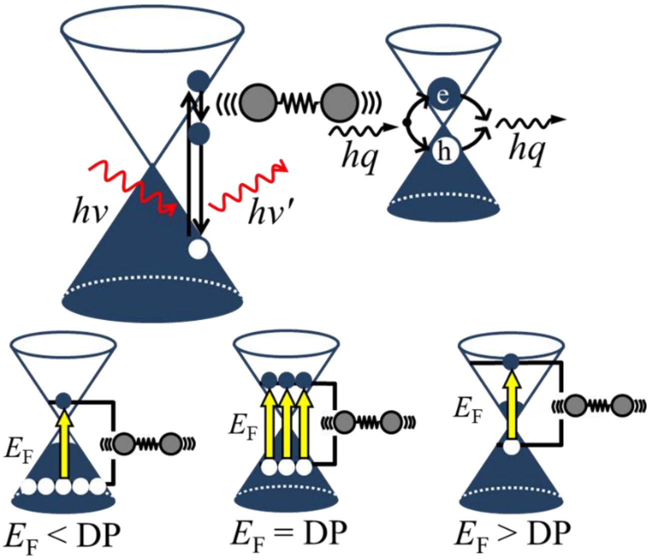

Fig. 1.8 Kohn anomaly process and Fermi energy dependence of electron-hole excitation [24]

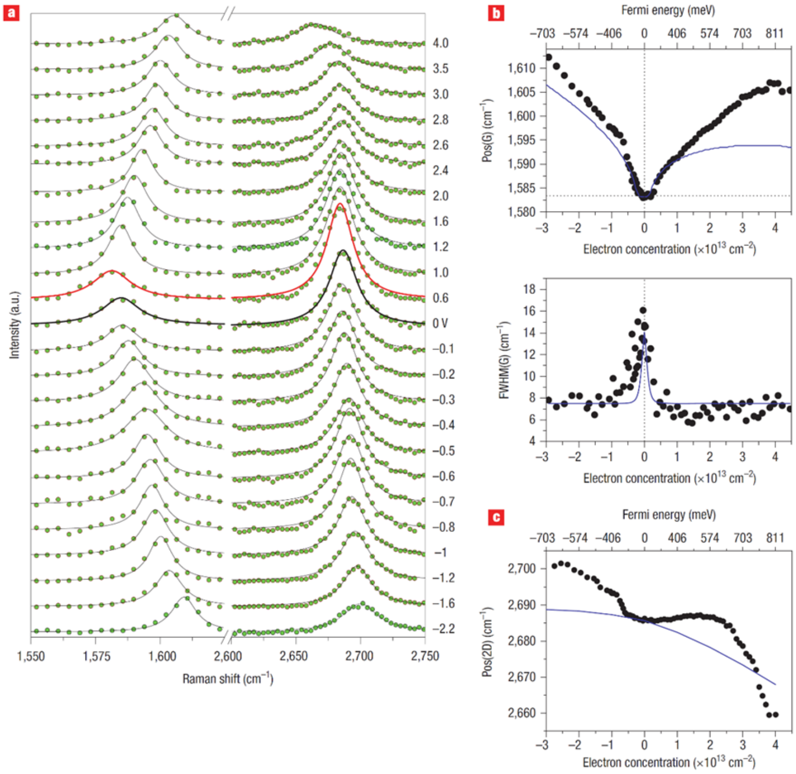

Fig. 1.9 Raman spectra of graphene as a function of gate voltage [25]

1.5.2.2 Raman spectroscopy for MoS_2

Raman peaks of MoS_2 appearing at approximately 385 and 403 cm^{-1} are identified as E_{2g} and A_{1g} (E' and A'_1 in the monolayer case), respectively, which correspond to the in- and out-plane vibration modes of MoS_2, respectively, as shown in Fig. 1.10(a).

The distance between E_{2g} and A_{1g} mode peaks is correlated to the number of layers. It increases from ~18 to ~25 cm^{-1} with the increase in the layer number until bulk mode. In the monolayer case, this distance should be appropriately 18 cm^{-1}, as shown in Fig. 1.10(b) [26]

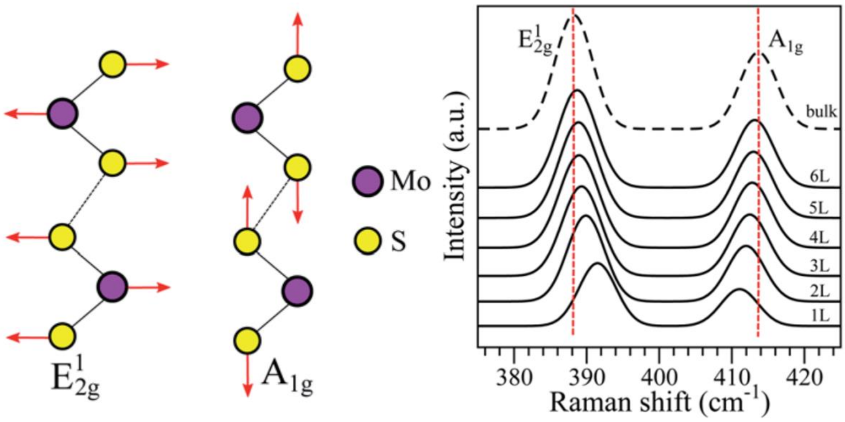

Fig. 1.10 (a) Vibration modes of E_{2g} and A_{1g}; (b) Layer number dependence of Raman spectroscopy for MoS_2 [26]

1.5.2.3 Raman spectroscopy for TaS_2

In the Raman spectra for TaS_2, a large sharp peak around 70 cm^{-1} is observed, together with some small peaks at 102, 240, 303, and 374 cm^{-1}. According to previous studies, these peaks broaden when the phase transitions from a commensurate charge density wave (CCDW) to a nearly commensurate CDW (NCCDW) [11]. Moreover, peaks are broadened more or may even disappear when the phase transitions from NCCDW to incommensurate CDW (ICCDW) .[27][28][29][30][31][32][33]

1.5.3 Photoluminescence (PL) for MoS_2

PL is a phenomenon in which light is generated when the excited electrons return to their ground state after being excited when a substance is irradiated with light. When light is applied to excite electrons, electrons and holes are generated in the conduction and valence bands, respectively, and the energy difference when these electrons and holes recombine is emitted as light. This emitted light is called fluorescence.

If the measured sample changes, for example, contains impurities or defects, an impurity or defect state will occur in areas other than the conducting or valence band, and electrons and holes may recombine from this state. The fluorescence is easily affected by impurities and defects in the material; therefore, the electronic information of a material can be obtained by detecting the change in fluorescence.

Both graphene and TaS_2 have no bandgap as they are zero-gap and metallic materials, respectively. Therefore, photo emission cannot occur from graphene and TaS_2. In this study, only MoS_2 can exhibit the PL phenomenon. As shown in Fig. 1.11 [34], in 1L-MoS_2, the A (~1.85 eV) and B (~2.02 eV) peaks correspond to the emission between two spin-split sub-bands of 1L-MoS_2 [35].

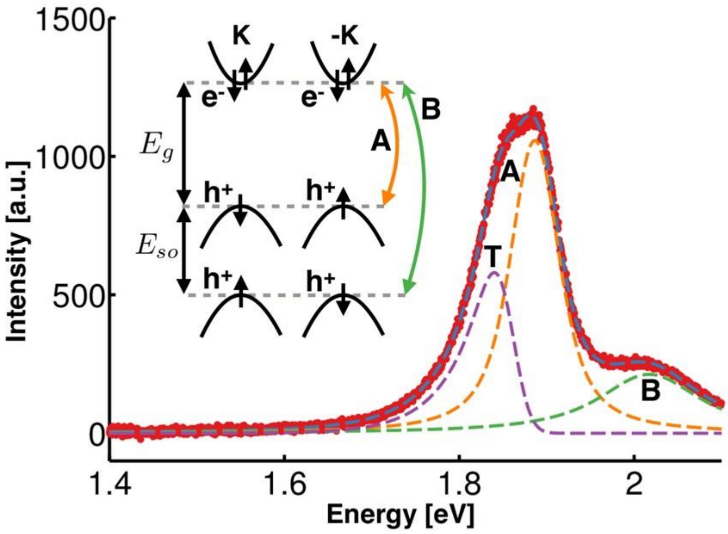

Fig. 1.11 Photoluminescence (PL) of 1L-MoS_2 [34]

1.5.4 Rutherford backscattering spectrometry

Rutherford backscattering spectrometry (RBS) is a typical elemental analysis method based on an ion scattering analysis technique for the deflected ion-beam by target sample. One of the advantages of RBS is that it determines the structure and composition of materials without a reference standard.

For RBS analysis, high-energy (MeV) He ion (i.e., alpha particles) are irradiated onto the sample, and the He ion at a given angle is detected. As the backscattering cross section for each element is already known, a quantitative compositional depth profile can be obtained from the energy and yield of the RBS spectrum.

Using RBS, the types, amounts, and distribution of elements that constitute the sample can be analyzed. It is a useful probing tool to evaluate the effect of ion implantation and gas adsorption. RBS is widely used in different fields to investigate the effect of ion implantation in 2D materials [36].

1.5.5 Conductivity measurement

Conductivity measurement is used to determine the electrical properties of 2D materials by measuring the transport curve of an FET that uses 2D materials such as graphene or MoS_2 as the channel material.

1.5.5.1 Field-effect transistor (FET) structure

FET is an electronic component that control the flow of current in a semiconductor material by applying an electric field. A schematic structure of the back-gate FET is shown in Fig. 1.12. An FET is equipped with three electrodes denoted as source, drain, and gate [37].

The gate of an FET is separated from the channel material by a thin insulating layer, typically as SiO_2 in this study. When a voltage is applied between the gate and source-drain terminals, the generated electric field surround the insulating layer and injects the carriers into semiconductor layer and changes its conductivity. By turning the gate voltage, electrons are injected or removed from the channel region, and the concentration of electrons or holes in the channel region are controlled, thereby controlling the current or resistance between the source and drain electrodes.

Typically, the current entering the channel between the source and drain terminals is defined as $I_{\mathrm{S\text{-}D}}$. The voltage between the source and drain terminals is defined as $V_{\mathrm{S\text{-}D}}$. Varying the gate voltage V_{G} changes the voltage between the gate and source-drain terminals, modulates the conductivity of this layer and thereby controls the $I_{\mathrm{S\text{-}D}}$. Generally, two electronic source meters (or one multichannel source meter) are used to support $V_{\mathrm{S\text{-}D}}$ and V_{G}.

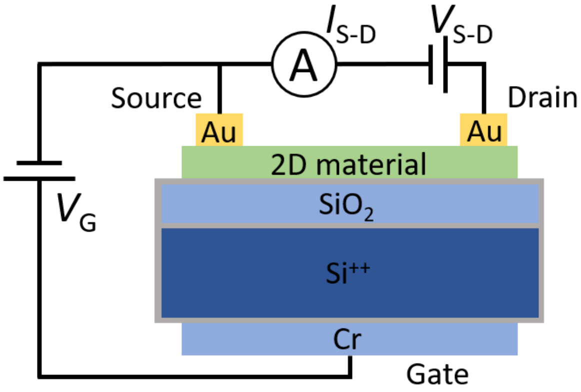

Fig. 1.12 Schematic structure of back-gate-type field-effect transistor (FET)

1.5.5.2 Four-terminal measurement

The four-terminal sensing or four-point probe method is a highly accurate technique for measuring electrical resistivity or conductivity of materials. This method is particularly useful for measuring low resistivity materials such as metals, semiconductors, and conductive thin films.

In a four-terminal measurement setup, two outer terminals are used to source a current into the material under test, while two inner terminals are used to measure the voltage. By separating the current path from the voltage measuring path, the voltage measurement is not affected by the contact resistance, resulting in a more accurate measurement, especially for low-resistance materials. This configuration helps to eliminate the effect of contact resistance and cable losses in remote-sensing (instruments connect the sample via a long cable for in situ measurements) conditions, which can significantly influence the measurement result in two-terminal methods.

1.5.5.3 FET fabrication

Generally, an FET structure is fabricated via a series of processes, including mechanical exfoliation, resist coating, lithography, development, metal deposition, and lift off, as shown in Fig. 1.13. In general, two types of lithography methods are used for exposure: photolithography using ultraviolet rays and electron-beam (EB) lithography using electron beams.

Photolithography processes are widely used in largescale semiconductor production processes. However, in the case of exfoliated 2D materials, the area of the target monolayer sample is significantly small relative to the area of the substrate, and the geometry and position of the sample varies for each sample. EB lithography is widely used in the field of 2D-material-based electronic devices as electrode patterns can be easily edited according to the size and position of graphene in each specific condition without requiring a photomask. Consequently, EB lithography was selected to fabricate electrode patterns in this study.

A 2D-material-based FET is fabricated via a series of processes as shown in Fig. 1.13 in our study. First, a spin coater is used to create a polymer-resist film on the surface of the substrate with monolayer flakes. Then, the electrode pattern designed for each specific sample is exposed using EB lithography, and only the resist in the exposed area is washed away (development). Next, gold is deposited over the entire surface of the substrate using a vacuum evaporation device. In the final lift off, the gold is washed away along with the resist in areas other than the pattern, leaving the gold only in the patterned area.

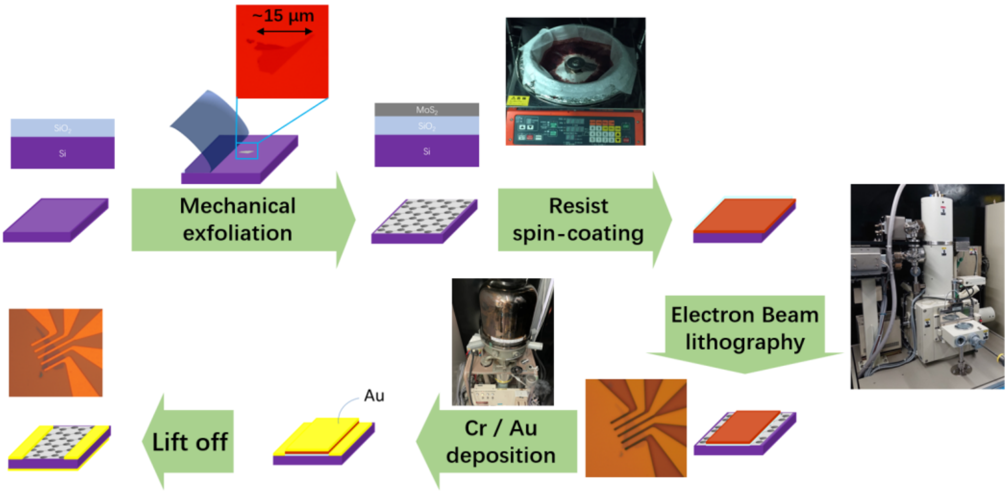

Fig. 1.13 Fabrication process of an FET including Electron-beam (EB) lithography

1.5.5.4 Transport properties

The conductivity of a material can be considered as a gas transport model that treats electrons like gas molecules in gas kinetic theory. When the average velocity of electrons is $\boldsymbol{v}$ and the elementary charge and number density of electrons are e and n, respectively, the current density j flowing through the conductor is

$$j = -nev\,. \tag{1.1}$$

Conversely, the Ohm's law relationship between current density and electric field E is as follows:

$$j = \sigma E, \tag{1.2}$$

where σ is the electrical conductivity. Inside an exact element, v is proportional to E.

$$|v| = \mu|E| \tag{1.3}$$

Here, μ is defined as carrier mobility, which can be calculated as

$$\sigma = -ne\mu. \tag{1.4}$$

1.5.5.5 Conductivity measurement for Graphene

The FET structure is a powerful probing tool that is widely used to measure the electronic properties of 2D materials. Notably, in a previous study, a new functionality was added based on graphene-hosted host-guest interactions as graphene exhibits significant change in its electronic states even with a significantly small amount of atomic and molecular adsorption. As a method for measuring the adsorption effect on graphene, a back-gate-type FET was used, and hole doping into graphene was reported by introducing oxygen molecules as a guest [38].

Fig. 1.14 shows the gate-voltage dependence of electric conductivity of graphene via oxygen molecule adsorption. In the measurement, after degassing in a vacuum environment, the charge neutral point (V_{CNP}), where the population of the hole and electron carriers are equal in the channel, is consistent with the gate voltage of 0 V. V_{CNP} corresponds to the position of the Dirac point in the energy axis. Conversely, exposure of oxygen at 0.1 MPa shifts the charge neutral point V_{CNP} toward positive voltage depending upon the exposure time [38].

The shift of the charge neutral point V_{CNP} to the positive voltage corresponds to the hole doping in the electronic bands of the channel material, whereas the shift to the negative charge corresponds to electron doping.

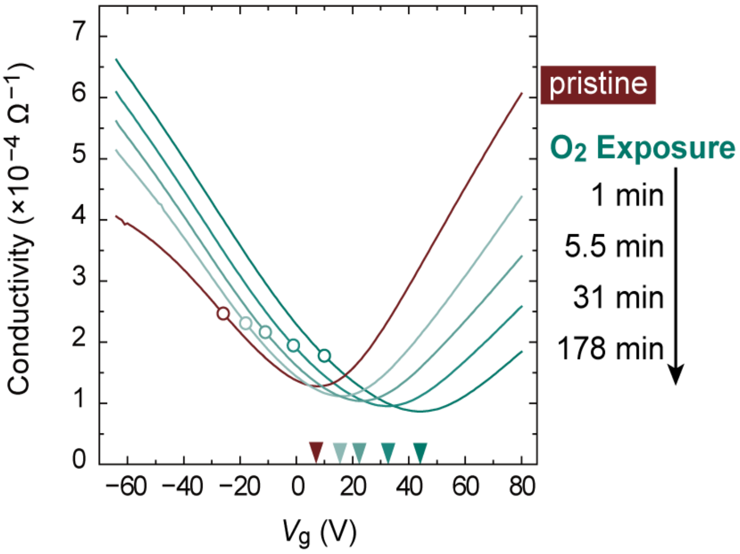

Fig. 1.14 Change in the transfer curve based on O_2 exposure [38]

1.5.5.6 Carrier density

Considering that the change in V_{CNP} is because of the charge potential resulting from the charge of carrier on the isolation layer, which can be considered as a capacitor, the doped carrier density n by the ion-beam irradiations can be calculated using the value of the shift of the gate voltage ΔV_{CNP} as

$$n = \frac{C_g}{e}\Delta V_{\mathrm{CNP}} = \alpha\Delta V_{\mathrm{CNP}}, \tag{1.5}$$

where e represent the elementary charge and C_g represent capacitance of the gate per unit area, which is calculated as $\varepsilon_0\varepsilon_\mathrm{r}/t_\mathrm{ox}$, where ε_0 represents the vacuum permittivity; ε_r and t_ox represent the relative permittivity and thickness of the gate dielectric material (285 nm of SiO_2 in this study), respectively. In this case, $\alpha = 7.56 \times 10^{10}$ cm^{-2}V^{-1}.

1.5.5.7 Carrier mobility

Carrier mobility, which is a critical property in the field of semiconductor physics, refers to how quickly an electron or hole can move through a semiconductor material when an electric field is applied. In FETs, higher mobility allows for greater current flow and faster switching speeds.

In the 2D condition, resistance R can be calculated as

$$R = \rho\frac{D}{W} = \frac{V_\mathrm{S-D}}{I_\mathrm{S-D}}, \tag{1.6}$$

where ρ is the resistivity, which is the reciprocal of electrical conductivity σ.

Conversely, equation (1.5) indicates the carrier density at charge neutral point, and the carrier density at any gate voltage V_G can be calculated as

$$n = \alpha V_\mathrm{G}. \tag{1.7}$$

By combining equations (1.4), (1.6), and (1.7), carrier mobility μ can be calculated as

$$\mu = \frac{I_\mathrm{S-D}}{V_\mathrm{S-D}V_\mathrm{G}\alpha e}\frac{D}{W}. \tag{1.8}$$

Here, $\frac{I_\mathrm{S-D}}{V_\mathrm{G}}$ is the gradient of the conductivity curve and $\frac{D}{W}$ is the aspect ratio of the channel part of the FET device.

1.5.5.8 Auto-measurement for transport properties

As shown in Fig. 1.14, the measurement of the transport curve requires a scanned control of gate voltage, and the conductivity at each gate-voltage point must be recorded.

To obtain a more accurate and consecutive curve, measurements should be performed at the maximum number of possible points. Furthermore, the interval time between each measurement point should be identical. In this case, an automatic measurement program is used to control the multiple instruments and record the data.

LabVIEW is the core software product of National Instruments. In contrast to other common programming languages, it is a graphical programming language makes programs look intuitive. LabVIEW was designed for tests and measurement, and several instruments and data acquisition equipment can be conveniently controlled by LabVIEW. Fig. 1.15 shows the control panel of a LabVIEW program for auto-measurement of FET conductivity for 2D materials that were specially developed for this study.

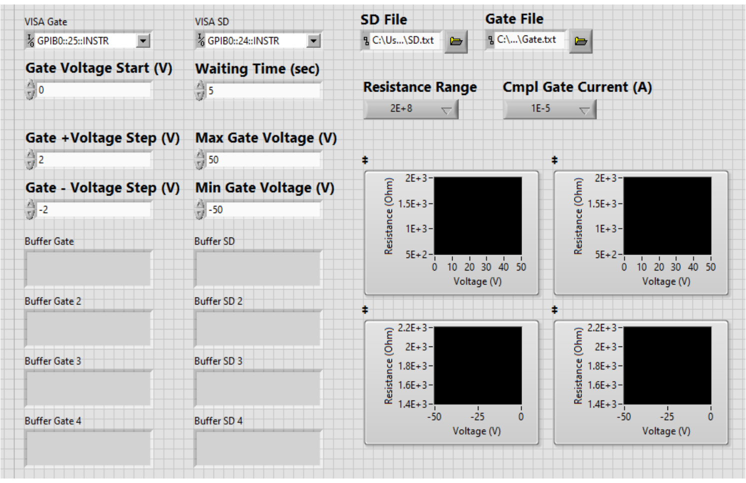

VISA Gate: GPIB0::25::INSTR
VISA SD: GPIB0::24::INSTR
SD File: C:\Us...\SD.txt
Gate File: C:\...\Gate.txt
Gate Voltage Start (V): 0
Waiting Time (sec): 5
Resistance Range: 2E+8
Cmpl Gate Current (A): 1E-5
Gate +Voltage Step (V): 2
Max Gate Voltage (V): 50
Gate - Voltage Step (V): -2
Min Gate Voltage (V): -50

Fig. 1.15 Control panel of a LabVIEW program for auto-measurement

1.6 Defects in 2D materials

2D materials are greatly sensitive to the presence of defects like lattice vacancies due to less percolation paths and weak screening effects. Owing to their low dimensionality geometry, both the real-space structure and the electron structure are vulnerable against slight perturbation of the system, and environmental effects have a greater influence on their structural, electronic, and chemical properties when compared to that of bulk materials [39]. 2D materials exhibit a high surface-to-volume ratio and all atoms are located on or significantly close to the surface; therefore, the relative surface area become larger, and the presence of defects can increase the number of adsorption sites for foreign molecules, and the adsorbed impurities has an impact on the electronic properties [40].The existence of defects affect the electronic conductivity and molecular adsorption, where defect sites act as a carrier scattering source and major adsorption sites, respectively.

Although defects have a significant influence on the structural and electronic properties of MoS_2 owing to its 2D characteristic, structural defects of MoS_2 always exist in samples regardless of whether they are prepared via CVD or exfoliated from natural minerals. This is a severe challenge in the defect engineering of 2D materials [7].

1.6.1 Defects in MoS_2

In MoS_2, structural changes due to Ar-ion irradiation have been reported, and their influences on Raman spectra are classified based on three types of vacancies [6]. As shown in Fig. 1.16(a), the defect species introduced into MoS_2 are primarily S, Mo, and MoS_6 cluster vacancies, where S vacancy indicates only an S atom loss within two overlapped S atoms, Mo vacancy implies an S atom loss, and MoS_6 vacancy indicates an S atom loss along with six surrounding S atoms.

As shown in Fig. 1.16(b), the presence of S vacancy results in a new broad peak involving the longitudinal acoustic (LA) mode at 220 cm^{-1} and a second-order LA (2LA) band appears at approximately 450 cm^{-1} owing to an overtone of LA phonons due to the presence of S vacancy. The presence of Mo vacancy results in shift to a lower wave number (redshift) in the E' mode peak. Finally, significant redshift in the E' peak and reduction in A'_1 peak by MoS_6 vacancy can be observed. Moreover, these vacancies are introduced by the order of S→Mo→MoS_6 clusters as the Ar-ion irradiation dose increases [6].

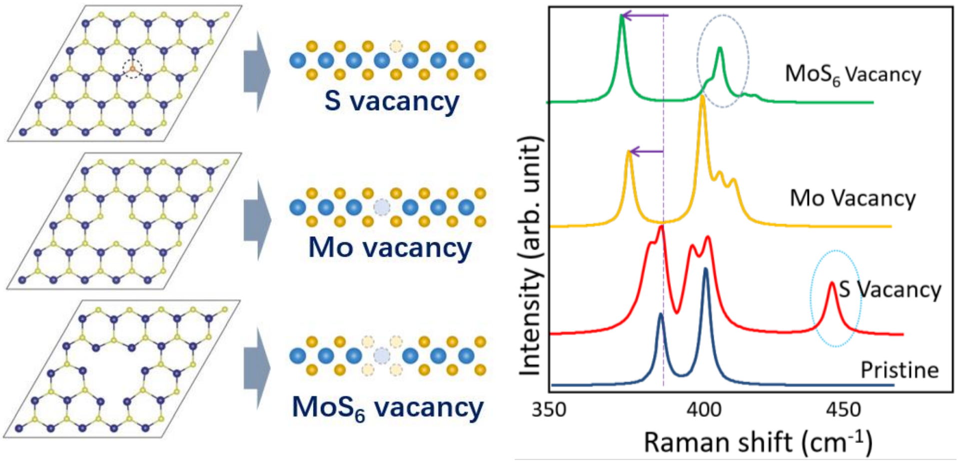

Fig. 1.16 (a) Typical vacancies in MoS_2; (b) Effect of different types of vacancies on Raman spectroscopy of MoS_2 [6]

1.6.2 Defects in Graphene

The defects present in graphene also affect its Raman spectra. As shown in Fig. 1.17, the presence of defect-like lattice vacancies and ionic impurities provide a sharp and shallow scattering potential for conduction carriers in graphene, which causes D (~1340 cm^{-1}) and D' (~1622 cm^{-1}) bands in the Raman spectrum, in addition to the G and G' bands [41]. Moreover, the intensity of the G' (2D) band decreases with the increase in the defect amount [14].

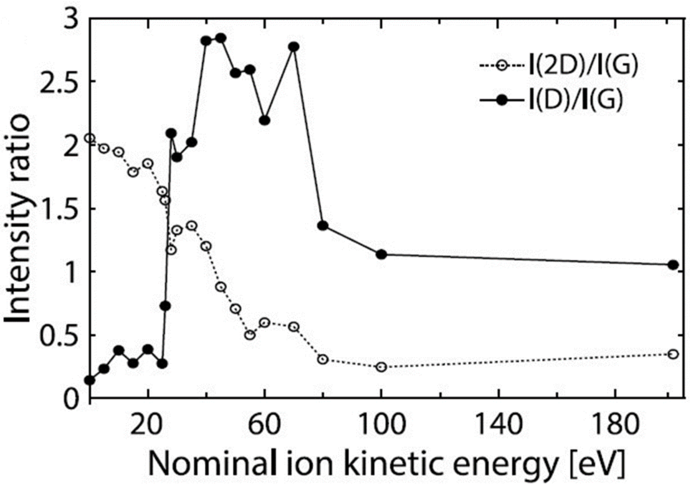

Fig. 1.17 Effect of defects on Raman spectroscopy of graphene [14]

1.7 Ion-beam irradiation

An ion beam is a bundle of charged atoms and molecules flowing at a constant speed. It is one of the excellent methods for quantitatively and reproducibly introducing defects and impurities into materials [42]. For example, Ochedowski et al. irradiated 1L-graphene and MoS_2 with U ion as fast heavy ions at different doses and investigated the effects on their electrical properties [43]. In addition, other researchers have irradiated two-dimensional materials with ions of Ag, Au, N, etc., and reported the effects on their structural and electronic properties [44][45][46]. For verifying the influence of defects on the structure and electronic properties of 1L-MoS_2 and Graphene, ion-beam irradiation to the sample is an excellent strategy to introduce defects and impurities under a well-controlled condition.

In this study, we use a low-energy gas source ion-beam gun and a solid source with a tandem accelerator for ion-beam irradiation. The schematic structure of an accelerator used in our study is shown in Fig. 1.18.

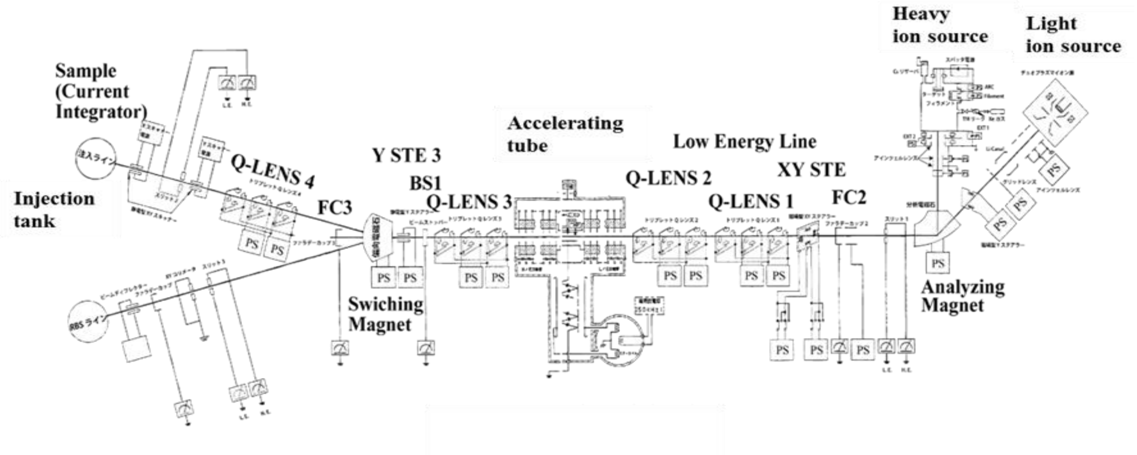

Fig. 1.18 Schematic view of an accelerator instrument.

1.7.1 Modification of electronic properties

Regarding the application in the field of electronic devices, tuning the number of charge carriers and carrier mobility are one of the major challenges of 2D materials. Especially various approaches have been explored for introducing guest species into graphene, which include adsorption onto adlayers, intercalation between 2D graphene sheets [47], and direct incorporation of foreign atoms into the graphene sheet [48]. Among these methods, the direct modulation of the electronic properties and structure of graphene via ion-beam irradiation is an appropriate technique for precisely controlling the number of guest chemical species [49][50], where charges of the injected ions in the sample are simultaneously neutralized upon irradiation. Here, it should be noted that atoms introduced by the ion beam exist in the same chemical states as those introduced by other impurity engineering methods, such as additives in material synthesis, wherein the net charge of the entire sample is electrically neutral after irradiation if no electric field is applied [51].

1.7.2 Monte Carlo simulation

To estimate the effect of ion beam, the first-principle methods could not calculate the stopping of ions in matter. Because an ion-beam irradiation into materials is a stochastic phenomenon well described by classical mechanisms, a statistical algorithm like the Monte Carlo method is always used to simulate the stopping and range of ions into matter [52].

Monte Carlo simulations are used to model the probability of different outcomes in a process that cannot be easily predicted due to the intervention of random variables. It is a technique used to understand the impact of risk and uncertainty in prediction and forecasting models. The method is used by professionals in widely disparate fields such as finance, project management, energy, manufacturing, engineering, research and development, insurance, oil and gas, transportation, and the environment.

1.7.3 Stopping and Range of Ions in Matter

The “Stopping and Range of Ions in Matter” (SRIM) [53] simulation program is widely used for calculations of stopping powers, range, and straggling distributions for any ion at any energy in any elemental target, including a compound material with multiple layers. SRIM code is a group of programs that compute the stopping and range of ions (up to 2 GeV/amu) in the target matter in the framework of classical collisions with parameters obtained by the results of experiments and fitting a quantum mechanical calculation of ion-atom collisions [52].

It is a promising tool for us to estimate the effect of ion-beam irradiation in target materials. Thu, SRIM is widely used for calculating vacancy production [54], simulating the energy loss for particles through thin film [55], and estimating the effect of ion-beam irradiation [56].

1.8 Objective

Tailoring the properties of 2D materials is an important requirement for its application in future electronic devices, such as tuning the number of charge carriers and carrier mobility, which are part of the major challenges. Various ion species were considered for irradiation to investigate the effect of ion beams on 2D materials systematically in this study. As for Ar, a noble gas particle, only mechanical defects like lattice vacancies are expected to be introduced by the Ar-ion beam. In contrast, irradiating Au-ion beam would cause not only mechanical defects but also chemical interactions like oxidation. Furthermore, I- and Fe-ion irradiation were also performed for more systematic investigation, considering their carrier scattering effect and magnetic properties.

In this study, the monolayer samples of graphene (zero-gap semiconductor), MoS_2 (direct-gap semiconductor), and TaS_2 (metallic) were fabricated by mechanical exfoliation method in view of modifying and verifying the properties of 2D materials. The beam irradiation of Ar, Au, I, and Fe ions, including noble gas, nonmetallic, metallic, and magnetic elements, modified the 2D materials to introduce defects or impurities under well-controlled conditions. The properties of 2D materials on the structure and the electronic properties were evaluated by Raman spectroscopy, RBS, photoluminescence, and conductivity measurements using FET device structure.

1.9 Structure of this paper

This thesis consists of 6 chapters.

Chapter 1 is a general introduction of 2D materials and the objective of this thesis.

In Chapter 2, we propose a low-energy Ar-ion beam irradiation method to introduce vacancies into 1L-MoS_2 in a controlled manner. Since the presence of vacancies in 2D materials, such as 1L-MoS_2, significantly affects their structural and electronic properties, a complementary study that combines multiple evaluations was performed to verify the role of vacancies in the structural and electronic properties of MoS_2. Raman spectroscopy and conductivity measurements reveal that the S vacancies, introduced into the MoS_2 lattice prior to Mo vacancies at the lower ion-beam dose region, cause electron doping. The E' lattice vibration mode was more sensitive to vacancies than the A'_1 mode in a Raman spectrum of MoS_2. According to photoluminescence studies, irradiating Ar ion at a lower dose of less than 3.8×10^{13} cm^{-2} does not change the band gap. It only introduces mid-gap states, consistent with the smaller and larger influences of vacancies in carrier scattering and doping, respectively, in the electrical conductivity. This study compares several measurement methods to confirm the mechanism of vacancy formation in MoS_2, providing a reference for future research and applications of 2D materials.

In Chapter 3, we discussed tuning the carrier transport properties of graphene as the fundamental structure of carbon materials to meet various requirements for the application to next-generation electronic devices related to carrier density, electron mobility, spin-orbit coupling, etc. We attempted to modify graphene by irradiating Au- or I-ion beam at 200 keV with dosages of 10^{13} - 10^{14} cm^{-2} using a NaCl sacrificial layer to introduce ions as guest chemical species into a two-dimensional graphene sheet as a quantitative chemical modification method. After removing the sacrificial layer, the ion-irradiated graphene was evaluated by Raman spectroscopy, electrical conductivity measurement, and Rutherford backscattering spectrometry. By irradiating the ion beam at the dosage of 10^{14} cm^{2}, both vacancies of carbon atoms, and Au atoms of 2.1×10^{13} cm^{-2}/I atoms of 1.2×10^{13} cm^{-2} are introduced into graphene, the latter of which act as charged impurities, resulting in the Raman D' band and the downshift of the Fermi energy through hole carrier doping. Using the sacrificial layer method, the modification of 2D materials by high-energy ion-beam irradiation becomes available, which could be expected in future applications.

In Chapter 4, we focus on the spin-orbit interaction of MoS_2, which can be expected to be applied to spin-valley electronics. By utilizing this valley-spin polarized state as an information carrier, a next generation communication could be developed, which is different from conventional electronics that only utilize the charge degree of freedom of electrons. Since the selective valley polarization in 1L-MoS_2 is affected by internal magnetic fields inside a material, the Fe atom, a magnetic atom, can be used to improve the valley polarization properties of MoS_2. We attempted to irradiate the Fe-ion beam at 200 keV with dosages of 10^{12} - 10^{15} cm^{-2} using a NaCl sacrificial layer to introduce the Fe ion into 1L-MoS_2 sheet as a modification method. After irradiation, circularly polarized photoluminescence measurements were used to measure the change in selective valley polarization property in room and low-temperature conditions.

In Chapter 5, we evaluated the layer number dependence of Raman spectroscopy on TaS_2, a type of metallic 2D material exhibiting a charge density wave (CDW) transition around room temperature and the Ar-ion irradiation effects. The temperature hysteresis of the Raman peak height related to the CDW transition decreases as the number of 1T-TaS_2 layers decreases. The difference in the dimensionality of the CDW superstructures and the competition between the pinning potential of defects and thermal energy explains this. The defect introduction by Ar-ion irradiation significantly broadened and decreased peaks related to the CDW superstructure.

Chapter 6 is the conclusion of this thesis.

Chapter 2 Ar-ion irradiation on monolayer MoS_2

2.1 Introduction

The presence of vacancies in two-dimensional (2D) materials, such as monolayer MoS_2 (1L-MoS_2), significantly affects their structural and electronic properties. In this study, 1L-MoS_2 was irradiated with an Ar-ion beam to introduce vacancies in a controlled manner. A complementary study that combines multiple evaluations was performed to verify the role of vacancies in the structural and electronic properties of MoS_2. Raman spectroscopy and conductivity measurements reveal that the S vacancies, introduced into the MoS_2 lattice before Mo vacancies at the lower dose region, cause electron doping. The E' lattice vibration mode was more sensitive to vacancies than the A'_1 mode. According to photoluminescence studies, irradiating Ar ion at a lower dose of less than 3.8×10^{13} cm^{-2} does not change the band gap and only introduces mid-gap states, which is consistent with the smaller and larger influences of vacancies in carrier scattering and doping, respectively, in the electrical conductivity.

This chapter is based on the journal paper published in 2023 [7].

2.1.1 MoS_2

Molybdenum disulfide (MoS_2) is a semiconductor composed of layered transition metal dichalcogenides with a broad range of electronic, optical, mechanical, and thermal properties. It is a promising channel material for fabricating field-effect transistors (FETs) [6]. In MoS_2, atoms inside each layer are bonded by covalent bonds, and layers are joined by van der Waals-like forces, enabling the isolation of its monolayer sheet as an individual material by the scotch-tape exfoliation technique [57]. Two-dimensional (2D) materials, such as monolayer MoS_2 (1L-MoS_2) and its stacking structures of two and three layers (2L- and 3L-MoS_2), have received significant attention in recent years owing to their 2D crystal lattices electronic structures, and extremely high specific surface areas [2]. Indeed, compared with bulk MoS_2 (which has an indirect band gap), 1L-MoS_2 has a direct band gap in its electronic band structure and a larger specific surface area, resulting in electronic properties that are affected mainly by molecular adsorption and the number of layers. Various 2D devices, including FETs and chemical sensors, can be fabricated using 1L-MoS_2. Their large direct bandgap is a significant advantage [9] over metallic materials (e.g., TaS_2 [11][12]) and zero-gap semiconductor 2D materials (e.g., graphene [38][58]).

2.1.1 Defect in MoS_2

2D materials are highly sensitive to the presence of defects such as lattice vacancies, which significantly limits their potential application in the fabrication of nanodevices. Owing to their intrinsic low-dimensional geometry, the real-space and electronic structures of these materials are vulnerable to slight system perturbations because of low percolation thresholds and weak screening effects [40]. Although vacancies significantly influence the structural and electronic properties of 2D-MoS_2, MoS_2 samples exhibit vacancies regardless of whether they are prepared via chemical vapor deposition or exfoliated from natural minerals. This is a severe challenge in the defect engineering of 2D materials. In this study, we introduced vacancies using ion-beam irradiation at low energy to investigate their effects on 2D materials. The low-energy ion-beam irradiation used here is a promising method for introducing vacancies. The precise control of the type and number of vacancies allows for the adjustment of the structural and electronic properties of the material through “defect engineering.” This study provides a valuable reference for future research and plays an important role in developing and fabricating 2D semiconductor materials.

2.1.2 Ion-beam irradiation

Several studies have explored the effects of ion-beam irradiation on 2D materials using various ion types, such as typical light elements and noble gas atom ions. For example, Gawlik et al. (2017) irradiated 1L-graphene with ions of He, C, N, and Kr at energies above 25 keV. They found that the structural and electronic properties were modified depending on the chemical species of the irradiated ions [59]. However, high-energy ions penetrate deeply through an atomically thin carbon film, such as graphene, on the surface of the target substrate as the energies of the ions decrease, resulting in large macroscale voids rather than atomic-scale vacancies in the crystal lattice [60]. To solve this problem in the ion-implantation of 2D materials, a NaCl inert sacrificial layer was deposited on the sample to stop ions on the surface of the 2D materials, where ion-species (B, N) dependence of the electronic properties of the irradiated graphene has been successfully reported [61]. On the other hand, simply reducing the ion-beam energy is a better strategy to introduce atomic-scale vacancies in 2D materials to modulate the crystallographic lattice in the case of irradiation with noble gas ions, which usually introduce vacancies into materials. Wu et al. (2021) systematically investigated the impact of Ar-ion beam irradiation on 1L- and multi-layer MoS_2 with a beam energy below 1000 eV using classical molecular dynamics (MD) simulations [62]. Irradiation using low-energy noble-gas-ion beams, such as He [63][64][65][66], Ar [62][67][68][69], and Xe ions [70], has been employed in both theoretical simulations [62][68][69][71] and experimental investigations, using Raman spectroscopy [63][64][65][66][67][70] to control its effect and avoid its interaction with MoS_2.

2.1.3 Molybdenum oxide

Since molybdenum oxide (MoO_2, MoO_3) attracts electrons through oxygen atoms and affects the physical properties of MoS_2, it is necessary to confirm whether oxygen is present in the prepared sample due to the oxidization process.

The peak representing MoO_2 is known to be located at a wavenumber of 200, 220, 355, 455, 490, and 740 cm^{-1}, and the peak representing MoO_3 located at a wavenumber of 158, 285, 340, 660, 820, and 995 cm^{-1} in the Raman spectrum [72][73].

2.1.4 Objective of chapter 2

Low-energy ion-beam irradiation is one of the methods to modify the structure and electronic properties of 2D materials in a well-controlled manner. However, they are highly affected by the sample preparation methods and experimental environments owing to their low dimensionality. So far, complementary research using unique samples prepared under the same conditions still needs to be completed. In this study, defects were introduced under a well-controlled condition via low-energy Ar-ion beam irradiation. Both structural and electronic properties were investigated by evaluating with combined techniques, Raman spectroscopy, photoluminescence (PL), and FET conductivity measurements on samples similarly prepared to understand the mechanism of the phenomena occurring in MoS_2 under low-energy beam irradiation.

2.2 Experimental

2.2.1 Sample fabrication

2.2.1.1 Preparation of MoS_2 sample

1L-MoS_2 was prepared by mechanical exfoliation from the surface of bulk crystal MoS_2 using scotch tape [17], as schematized in Fig. 2.1(a). In MoS_2, atoms inside each layer are bonded by covalent bonds, and layers are joined by van der Waals-like forces, enabling the isolation of its monolayer sheet as an individual material by the scotch-tape exfoliation technique.

Compared with CVD, another popular method for the fabrication of 2D materials, mechanical exfoliation is a more simple and convenient method for experimental investigation. Compared with CVD, which needs a set of vacuum chambers and gas flow/temperature control instruments, mechanical exfoliation only needs scotch tape and pure crystal to get a monolayer sample. On the other hand, seeking monolayer flakes is one of the biggest challenges in sample preparation.

Using scotch tape, a few layers of flakes could be easily exfoliated. However, most flakes on the tape were multilayer rather than monolayer. To get monolayer flakes with higher probability, the exfoliated flakes needed to be peeled 5-10 times on the tape and then transferred to the surface of a silicon substrate coated with a 285 nm-thick SiO_2 layer. After the peeling of the tape, many MoS_2 flakes were distributed on the substrate, and the substrate was cleaned with acetone and isopropanol to remove the residual glue from the tape, but with extremely weak ultrasonic processing to avoid the flakes on the substrate also be removed.

After sample preparation by mechanical exfoliation, monolayer samples exist on the substrate, but most flakes on the substrate are multilayer. Thu, few-layer MoS_2 samples are distinguished using an optical microscope in the scotch tape method [17]. Typically, the substrate was observed under an optical microscope with a 20x objective lens for large-area search. After some probable monolayer candidates were found by eyes, the 50x and 100x objective lenses were used for further confirmation. Only human eyes were used to identify samples at this stage. Then, a digital camera adapted to the OM was used to take photos using a 100x objective lens with a red/green filter. The sample position was also recorded for further investigation. The typical scale of the monolayer sample was 10–20 μm.

2.2.1.2 Layer number evaluation

The number of layers was determined by brightness contrast in the optical image and confirmed by Raman spectroscopy [26].

An optical microscope image is used for the initial evaluation of the layer number of MoS_2 by checking the brightness difference between the sample and substrate. In the sample search procedure, the photo of the probable monolayer sample was taken with a red and green filter. The contrast was found in the image processing software and compared with reference papers to get the layer number result.

This method needs to be more accurate and used as the initial evaluation. The exact layer number should be confirmed by Raman spectroscopy. Regarding the Raman spectrum, the distance between the E_{2g} and A_{1g} mode peak is correlated with the number of layers. In the monolayer case, this distance should be around 18 cm^{-1} [26].

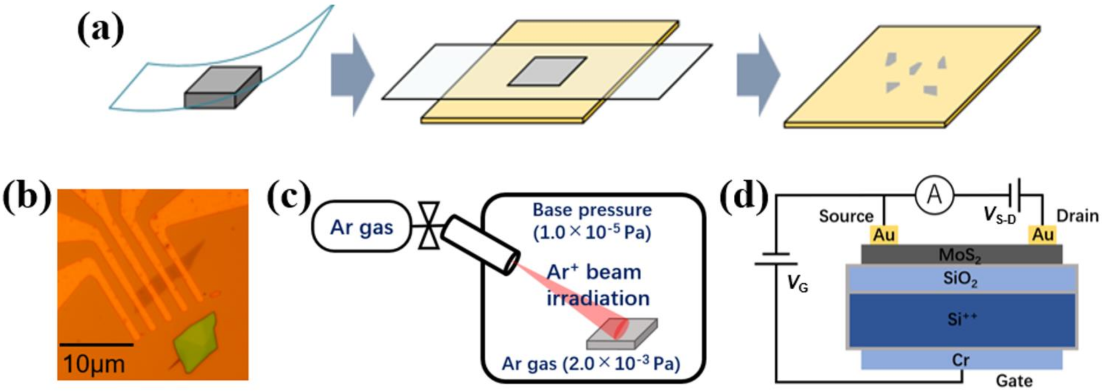

Fig. 2.1 (a) Schematics of the MoS_2 preparation process. (b) Optical microscope image of 1L-MoS_2 and the source-drain electrodes of the FET. Schematics of (c) the ion irradiation instrument and (d) the 1L-MoS_2 FET device structure.

2.2.1.3 FET device fabrication

A FET structure was fabricated based on the monolayer MoS_2 as the channel material to measure the electronic properties of semiconducting materials. As shown in the previous section, a monolayer MoS_2 sample exists on the substrate with a random position on the surface of the substrate. It means we cannot prepare the sample at a specific place, and the position and surrounding environment of the MoS_2 sample on each substrate are different. In this case, electron beam (EB) lithography is used for FET structure fabrication to ensure that the electrode circuit pattern structure aligns with the MoS_2 sample.

The electrode for the conductivity measurement was fabricated using EB drawing equipment (ELS-7500, ELIONIX). The EB pattern is designed using CAD software for each specific sample substrate with a monolayer MoS_2 sample. The size, direction, and position of the circuit of the FET structure were adjusted for each sample to match the sample flake for each substrate. Usually, we used 1um for electrode width, 2um for pitch (the distance between each electrode), and at least four electrodes per sample. However, the exact parameter depended on the specific condition of each sample.

A spin-coater is used for the resist coating procedure, as shown in Table 2.1.

a) OAP was coated on the surface of a substrate to modify its surface property and improve the adsorption ability of polymer resist. After spin-coating, it was heated at 80°C for 60 seconds to dry it out.

b) A layer of polymer resist (ZEP520A, ZEON JAPAN) was coated on the substrate surface as a resist layer for EB. It was heated at 180°C for 120 seconds to dry it and cool it down for several minutes.

c) A Charge-dissipating agent (ESPACER 300Z, Showa Denko) was spread on the substrate surface to increase the conductivity, improving the stability of the electron beam.

Table 2.1 Coating procedure of polymer resist

Cap layer coating (OAP, Tokyo Ohka Inc.)	Spin coat （500 rpm, 2 s → 5000 rpm, 30 s） Baking（80 °C, 1 min）
Resist Coating (ZEP520A, ZEON JAPAN)	Spin coat （500 rpm, 8 s → 5000 rpm, 70 s） Baking（180 °C, 2 min）
Charge-dissipating agent (ESPACER 300Z, Showa Denko)	Spin coat （500 rpm, 3 s → 2000 rpm, 90 s）
Lithography	350 μC/cm^2
Development	(Xylene) 5 min

Before the actual EB exposure, a set of markers should be exposed and developed to align the position of the FET structure with the MoS_2 sample accurately. Because the origin for the coordinate (usually a corner of the SiO_2/Si substrate) of the MoS_2 sample could not be reset very accurately confirmed by the sample stage of the EB instrument in micrometer scale, it is impossible to determine the position only with the coordinate relative to the origin. In this case, markers are fabricated around the MoS_2 sample. After the development of the markers, the relative position between them and the MoS_2 sample was observed and recorded using the optical microscope. Then, based on the markers, we can accurately calculate the relative position of the MoS_2 sample and adjust the CAD file for FET exposure. The width of the source and drain electrodes was 1 μm, and the gap between the electrodes was 2 μm (Fig. 2.1(b)).

The alignment should be performed as soon as possible to avoid non-intentional EB exposure during SEM observation of the marker. After aligning the position of the pattern with the sample, EB exposure was performed with 1 nA, 50kV. For development, xylene was used to remove the exposed resist. Then, a vacuum depositing instrument was used to deposit metal electrodes on the MoS_2 sample under high vacuum conditions (VPC-260, ULVAC) to fabricate the FET structure.

Metal electrodes were deposited on the MoS_2 sample under high-vacuum conditions (VPC-260, ULVAC). The source–drain electrode was fabricated by placing a 1 nm-thick Cr layer below a 10 nm-thick Au layer, and the gate electrode was a 15 nm-thick Cr layer.

2.2.1.4 Annealing

To remove the atmospheric gas species adsorbed on the sample surface and the interface between the sample and electrodes or substrate, the sample was heat-treated in a custom-built vacuum chamber before the introduction of vacancies and the FET conductivity measurements. The device was pre-annealed at 180 °C for 12 h at a pressure of 5×10^{-4} Pa to prevent the adsorption of gas atoms and to ensure that the electrodes were in optimal ohmic contact with the sample.

2.2.2 Ion-beam instrument setup

To introduce vacancies, an ion-beam gun able to support a low-energy even irradiation over a large area (OMI-0010, Omegatron) was attached to the vacuum chamber and connected to an Ar gas cylinder (>99.9999%), as shown in Fig. 2.1(c). The ion fluence was calculated from the beam current, measured by a copper plate, and the trace on a dummy substrate detector detected the irradiated area. The irradiated area was sufficiently large to cover the entire MoS_2 sample. The samples were irradiated using an Ar-ion beam in a high-vacuum chamber at room temperature with an acceleration voltage of 100 eV and a dose of $0–3.7 \times 10^{16}$ cm^{-2}. The angle of the beam was 60° with respect to the normal direction of the sample plane. 60° is the optimal setting for vacancy introduction owing the large projected atomic density of the target in the ion direction [74]. Hereafter, 0 cm^{-2} indicates the non-irradiated sample after annealing in the high-vacuum chamber. The argon gas pressure was 2.0×10^{-3} Pa inside the vacuum chamber upon irradiation, and the base pressure was below 1.0×10^{-5} Pa.

Here, the dose was calculated using beam current and irradiated area. The beam current was measured by placing a copper plate instead of a Si substrate at the sample stage, and an accurate current meter was connected between the copper plate and the ground. After adjusting the ion-beam gun to the same condition as Ar-ion beam irradiation, the beam current could be obtained from the current meter, which is 0.32 μA. On the other hand, a dummy substrate plate was placed at the sample stage. After a very long time irradiation, the trace of the ion beam could be observed on the dummy substrate. Here, we used various kinds of dummy substrate, including photo paper, thermal sensitive paper, and Si substrate coated with a gold layer. Here, the thermal paper worked best. The beam-irradiation area is 326 mm^2.

2.2.3 Sample characterization

2.2.3.1 Raman spectroscopy/PL

Raman spectroscopy and PL analyses were performed using a microscopic spectrometer (LabRAM HR Evolution, HORIBA) before and after Ar-ion beam irradiation at an excitation laser wavelength of 532 nm on a temperature-controllable stage. After irradiation and filling the vacuum chamber with high-purity Ar gas (>99.9999%), the sample was taken out and immediately measured using a microscopic spectrometer under ambient conditions. In the temperature dependence experiments on PL, the samples were sealed inside the cryostat chamber with a temperature control stage and under a nitrogen gas atmosphere. Raman spectroscopy was performed at 296 K, and PL was measured at 118 and 296 K. The temperature throughout the experiment was controlled using a cryostat with liquid N_2.

2.2.3.2 FET conductivity

FET conductivity measurements were performed before and after Ar-ion beam irradiation in a high-vacuum chamber using two electronic source meters (2400A, KEITHLEY). The $I_{S\text{-}D}$–V_G curve was measured at a source–drain voltage of 0.1 V, and the gate voltage was varied between -50 and +50 V in 2 V steps. Schematics of the MoS_2 preparation process and the MoS_2-FET device structure are presented in Fig. 2.1(d).

2.2.4 LabVIEW automatic measurement and recording

The LabVIEW program was developed to control multiple instruments automatically and collect data from them in the conductivity measurement. With an automated measurement system, changing the measurement parameters and collecting data for several devices simultaneously within a very short period is more manageable.

In this study, the LabVIEW program was designed for two objectives: electrical conductivity measurement with FET structure and automatic long-term monitoring of the source-drain current.

2.2.4.1 Conductivity measurement

In this study, two electronic source meters were used to control the voltage and measure the current of the FET conductivity measurement. We used one to set up the gate voltage V_G and record the leak current and another to set up the source-drain voltage $V_{S\text{-}D}$ and record the source-drain current $I_{S\text{-}D}$. Again, it should be noted that achieving this operation manually with a specific fixed interval (waiting time) is extremely difficult.

LabVIEW was used to control the instrument automatically to measure and record data. LabVIEW program was developed based on the loop function. It repeatedly increased or decreased the gate voltage V_G by step and recorded $I_{S\text{-}D}$ after waiting x seconds until the V_G achieved the limitation. The detailed structure of the program is shown in Fig. 2.2.

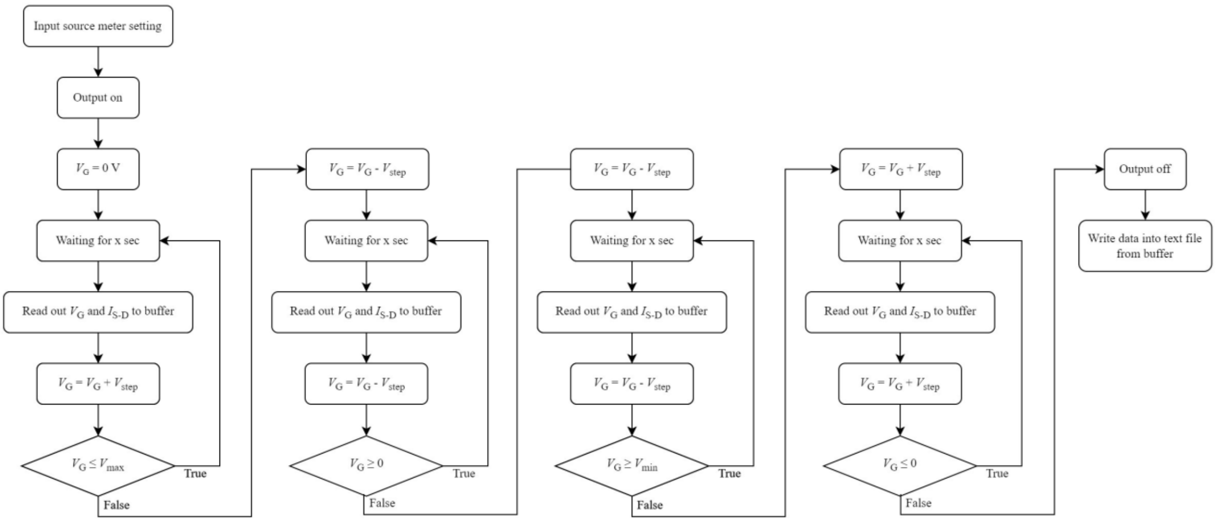

Fig. 2.2 Structure of electrical conductivity auto-measurement program

2.2.4.2 Long-term monitoring

In addition to automatic conductivity measurement, we also need to monitor the change in the transport parameters during a long term, for example, to record the variation of $I_{S\text{-}D}$ under light exposure or during gas introduction and adsorption. To achieve this purpose, a LabVIEW program was developed based on the loop function, which recorded $I_{S\text{-}D}$ after waiting x seconds until the STOP button was pressed. The detailed structure of the program is shown in Fig. 2.3.

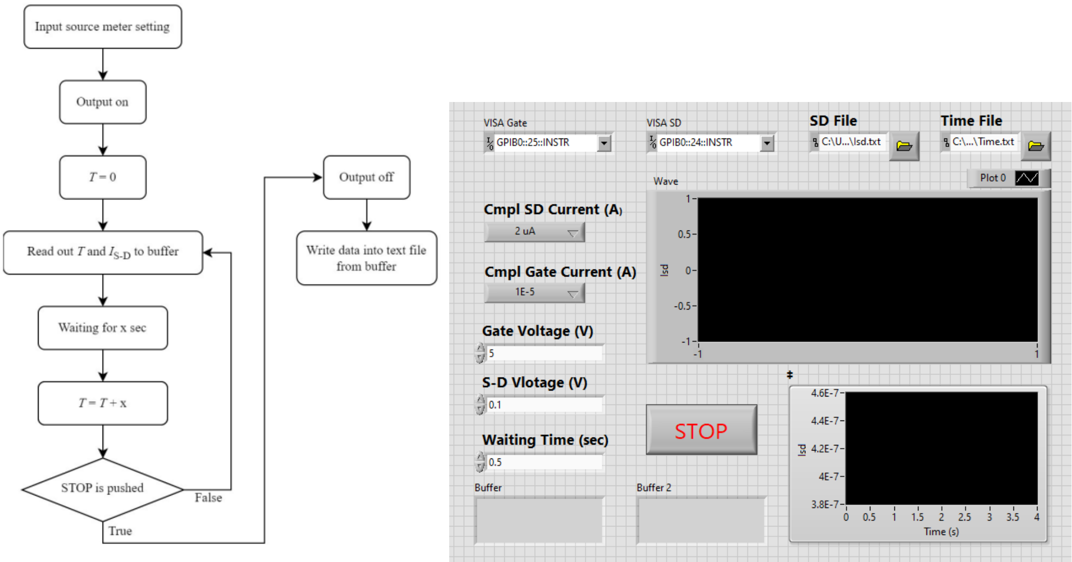

VISA Gate GPIB0::25::INSTR

VISA SD GPIB0::24::INSTR

SD File C:\U...\Isd.txt

Time File C:\...\Time.txt

Cmpl SD Current (A) 2 uA

Cmpl Gate Current (A) 1E-5

Gate Voltage (V) 5

S-D Vlotage (V) 0.1

Waiting Time (sec) 0.5

Buffer

Buffer 2

Fig. 2.3 Structure and control panel of long-term monitoring program.

2.3 Results and discussion

2.3.1 Raman spectroscopy

The Raman spectra of 1L-MoS_2 before and after annealing (denoted as 0 cm^{-2}) and after each Ar-ion irradiation with a dose of up to 3.7×10^{16} cm^{-2} are shown in Fig. 2.4. In the MoS_2 sample spectra, the peaks corresponding to the E' (in-plane vibration) and A'_1 (out-of-plane vibration) modes, which are the characteristic Raman peaks of 1L-MoS_2, appear at approximately 385 and 403 cm^{-1}, respectively. Before Ar-ion irradiation, the difference between the E' and A'_1 peak positions was approximately 18 cm^{-1}, which indicates the 1L-characteristic of the MoS_2 sample film [26].

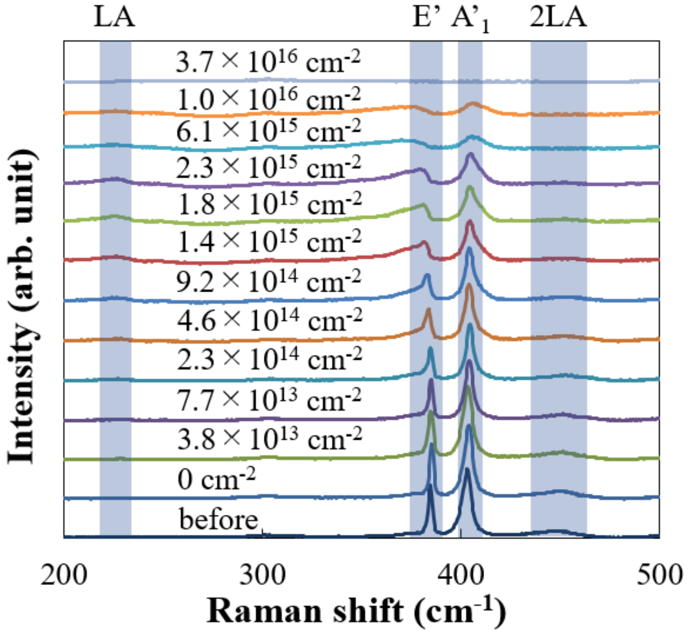

Fig. 2.4 Raman spectra obtained at various irradiation doses. The baselines of the spectra are shifted in the vertical axes each other to clarify.

As shown in Fig. 2.5, satellite peaks were identified near E' and A'_1 after Ar-ion irradiation. Both E' and A'_1 peaks were apparently broadened in the linewidths due to widening and merging with the satellite peaks as the irradiation dose increases. In a previous study, the vacancies in MoS_2 introduced by ion-beam irradiation were classified into three types: S, Mo, and MoS_6 cluster vacancies [6]. Local phonon modes derived from the local vibration around the vacancies generate satellite peaks on the low-wave-number side of the E' peak and high-wave-number side of the A'_1 peak. Hereafter, the satellite peaks of E' and A'_1 located at around 375 cm^{-1} and 410 cm^{-1} are denoted as E'_{sat} and A'_{1sat}, respectively. The Raman peaks of 1L-MoS_2 before and after annealing (0 cm^{-2}), and after each Ar-ion irradiation dose were analyzed by Lorentzian peaks fitting as typically shown in Fig. 2.5 (a). The positions and intensities of the Raman peaks are summarized in Fig. 2.5 (b) and 2.6. The apparent increase in the linewidth seen in Fig. 2.4 is attributed mainly to superimposing satellite peaks caused by the introduction of vacancies into the main peak (E' and A'_1).

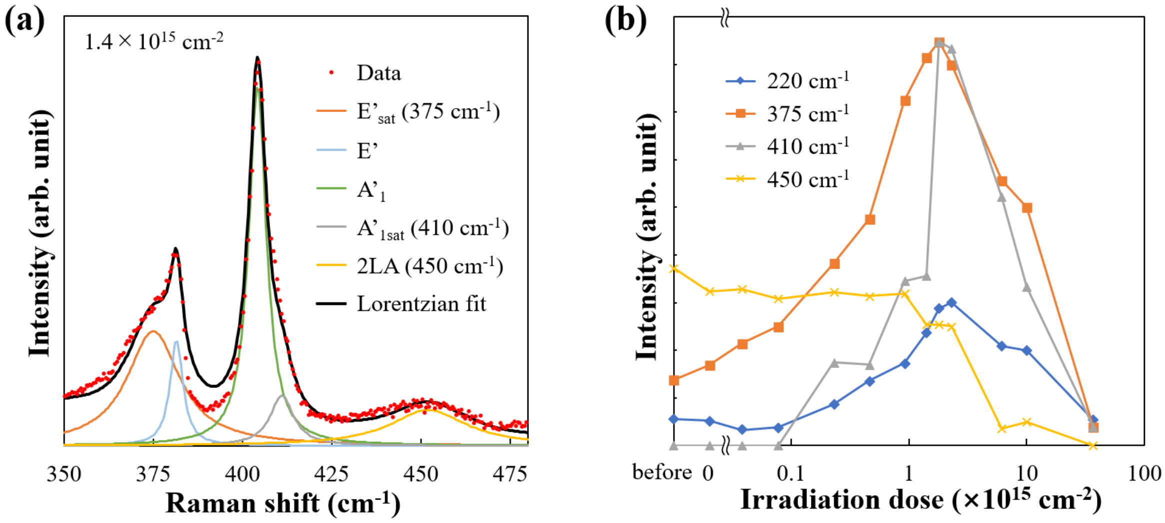

Fig. 2.5 (a) An example of Lorentzian peaks fitting and (b) Raman peak intensities at various irradiation doses.

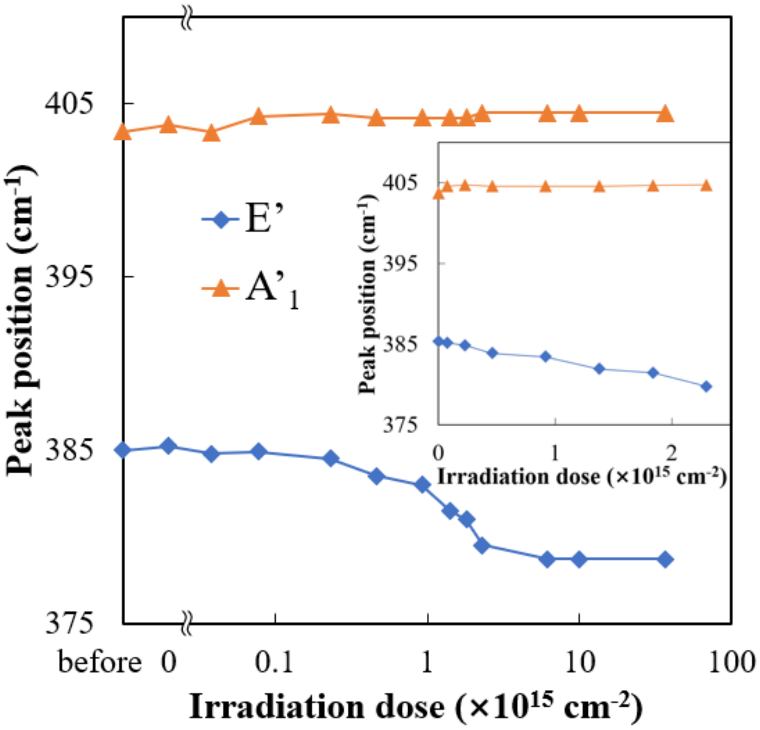

Fig. 2.6 Irradiation dose dependence of the Raman peak positions of E' and A'$_1$ modes of 1L-MoS$_2$ irradiated with an Ar-ion beam. The inset is the Raman peak position at a low Ar-ion dose.

The peaks at approximately 220 cm^{-1}, called as the LA mode peaks, originate from S vacancies [75] and gradually increase in intensity up to the irradiation dose of approximately 1 × 10^{15} cm^{-2}. However, their intensities then decrease, which indicates that S vacancies are mainly generated at dose levels up to approximately 1 × 10^{15} cm^{-2}. In contrast, the peak at approximately 450 cm^{-1} corresponding to the second-order harmonic of the LA mode (2LA) is not directly correlated with the number of vacancies. 2LA originates from the double-resonance Raman process and appears even in non-defective MoS$_2$ crystals [76]. Indeed, 2LA maintained its initial intensity with a slight decreasing trend regardless of the irradiation dose up to approximately 5 × 10^{15} cm^{-2}. The E'$_{sat}$ peak at approximately 375 cm^{-1} corresponds to a satellite peak of the E' peak, derived from both the S and Mo vacancies [6]. The intensity of this peak increases at doses below 1 × 10^{15} cm^{-2} and rapidly decrease at higher doses.

The A'$_{1sat}$ peak at approximately 410 cm^{-1} corresponds to a satellite peak of the A'$_1$ peak, derived from the Mo vacancies [6]. The peak intensity is not noticeable at lower doses, but appears at approximately 1 × 10^{14} cm^{-2}, rapidly increases at doses higher than 1 × 10^{15}

cm^{-2}, and decreases at doses higher than 5 × 10^{15} cm^{-2}. This indicates that Mo vacancies appear mainly above approximately 1 × 10^{15} cm^{-2}, causing a rapid increase in the intensity of satellite peaks.

The formation of MoS_6 vacancies at irradiation doses above 5 × 10^{15} cm^{-2} is responsible for the decrease in the intensity of satellite peaks caused by S and Mo vacancies.

Thus, in the lower irradiation dose region, S atoms were knocked out prior to Mo atoms. MoS_6 cluster vacancies formed at significantly high irradiation doses where even 2LA peaks decreased. The difference between introducing S and Mo vacancies is due to their atomic masses and lattice structure. The displacement threshold energy of the Mo atom is six times higher than the S atom [74] which is located at surface and its bonding energy is significantly lower than the atoms inside crystal lattice like the Mo atoms. On the other hand, as the irradiation dose increases, the lattice become loosens [77], and the Mo atom is exposed to the ion beam due to the S atom being knocked out as shown in Fig. 2.7. This explains why a large quantity of Mo atoms start to be knocked out of the lattice at higher dose, which is later than S atoms.

Fig. 2.7 Schematic of Ar-ion beam irradiation before and after S vacancy introduction.

This is also supported by the position of the E' mode peak. The E' peak gradually red-shifted as the irradiation dose increased, as shown in Fig. 2.6. This is in good agreement with theoretical simulation results for 1L-MoS_2 containing S vacancies [75]. The red-shift in the E' peak was more pronounced at an irradiation dose of 1 × 10^{15} cm^{-2}, suggesting the role of Mo vacancies centered in the MoS_2 crystal structure that further weaken the in-plane vibration. Irradiating with a dose of 5 × 10^{15} cm^{-2} led to a significant red-shift in the E' main peak and a decrease in the A'$_1$ peak intensity, cause by the introduction of MoS_6 vacancies. Irradiation has a more pronounced effect on the E' peak than on the A'$_1$ peak, contrasting the charge transfer by molecular adsorption, where the A'$_1$ peak position is significantly more sensitive to molecular adsorption doping owing to its large electron-phonon coupling. The presence of S vacancies weakened the strength of the covalent bonding between adjacent Mo atoms, resulting in a more significant reduction in the in-plane vibration energy than that in the out-of-plane vibration. In contrast, the peak position of the A'$_1$ peak up-shifted slightly as the irradiation dose increased (Fig. 2.6). This is attributed to the gradual reduction in total lattice system mass owing to vacancy introduction, leading to a very small increase in vibration frequency.

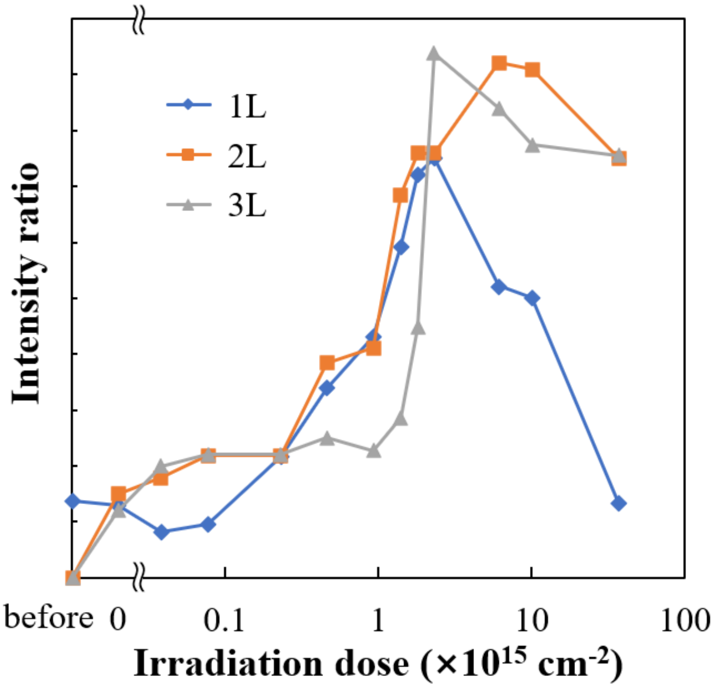

Fig. 2.8 Irradiation dose dependence of the Raman peak intensity ratio of 220 cm^{-1} to the Si substrate peak for 1L-, 2L-, and 3L-MoS_2.

Fig. 2.8 shows the Raman peaks intensity ratio of LA (220 cm^{-1}) to the Si substrate peak for MoS_2 with different layer numbers. As indicated by the ratio of the S-vacancy peak (220 cm^{-1}), the influence of irradiation on lattice vibration of the 1L-MoS_2 samples increase rapidly at doses lower than 1 × 10^{15} cm^{-2}, indicating that it is easier to introduce S vacancies to MoS_2, and then decrease because of the formation of Mo vacancies and MoS_6 cluster vacancies.

The formation of S-vacancies reached a maximum at similar doses in the 2L- and 3L-MoS_2 samples. However, the intensity of LA did not decrease significantly even at doses higher than 1 × 10^{15} cm^{-2}. This is explained as following. The underlying layers in 2L- and 3L-MoS_2 were hard to access for Ar ions before a sufficient number of lattice vacancies developed in the topmost layer. At doses higher than 1 × 10^{15} cm^{-2}, the second and third layers in 2L- and 3L-MoS_2 becomes accessible for Ar ions through the MoS_6 cluster vacancies formed in the topmost layer as indicated by the reduction of LA peak intensity for 1L-MoS_2 sample. Thus, S vacancies formed in the second and third layers still give significant intensity of the LA peak for 2L- and 3L-MoS_2 samples at doses higher than 1 × 10^{15} cm^{-2}, where the topmost layer does not contribute to the LA peak due to the conversion of S-vacancies to the MoS_6 cluster vacancies.

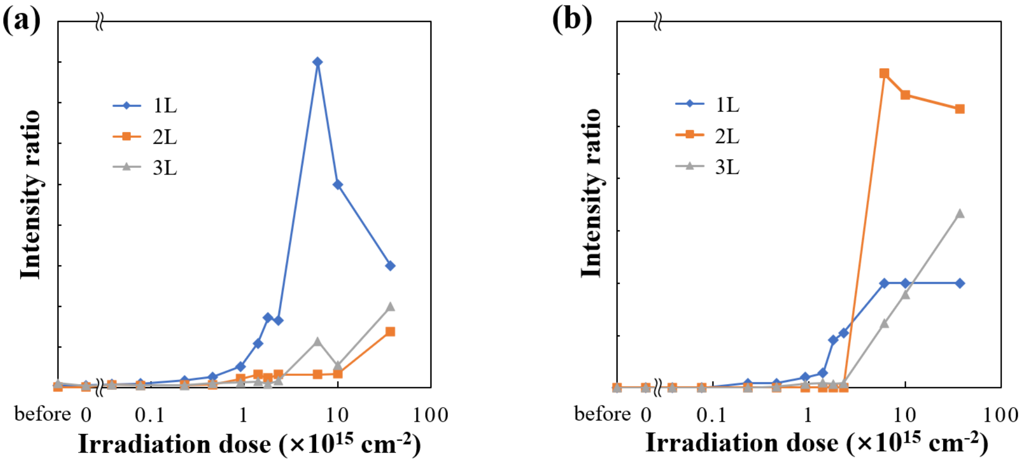

Fig. 2.9 Irradiation dose dependence of the Raman peak intensity ratio of (a) 375 cm^{-1} to E' and (b) 410 cm^{-1} to A'_1, for 1L-, 2L-, and 3L-MoS_2.

The peak intensity ratio of E'_{sat} (around 375 cm^{-1}) to E' peak and the peak intensity ratio of A'_{1sat} (around 410 cm^{-1}) to the A'_1 peak at different doses for 1L-, 2L-, 3L-MoS_2 are shown in Fig. 2.9 (a), and (b), respectively. Here, it should be noted that the contribution of the effects of vacancies in E'_{sat} and A'_{1sat} are indicated as the ratio to the total lattice vibrations of the whole layers of MoS_2 samples in Fig. 2.9 (a) and (b). The peak intensity ratio of E'_{sat} corresponding to both of S and Mo vacancies increases up to around 5 × 10^{15} cm^{-2} and becomes decreasing at the higher doses due to the formation of the MoS_6 cluster vacancies. In the case of 2L- and 3L- MoS_2 samples, the ratio of the contribution of S and Mo vacancies to the total vibrations in the whole layers remains increasing due to the vacancy formation in the second and third layers even at the higher doses than 5 × 10^{15} cm^{-2}. Interestingly, the peak intensity ratio of A'_{1sat} to the A'_1 peak corresponding to the Mo vacancies significantly increases in 2L- and 3L-MoS_2 samples in contrast to the E'_{sat}. This is attributed to the difference in the vibration modes between E' and A'_1. The E' modes are in-plane vibrations of the lattice, and each vibration comparatively behaves independently. Thus, the effects of the introduction of vacancies are roughly additive. In contrast, A'_1 modes are out-of-plane vibrations of the lattice, intricately influenced by the adjacent layer(s). In the case of 2L-sample, the presence of Mo or MoS_6 cluster vacancies in the topmost layer also significantly affects the second layer at higher doses than 5×10^{15} cm^{-2}. In contrast, the change of the circumstances of the second layer upon introduction of Mo and MoS_6 cluster vacancies in the topmost layer is moderate in the 3L-sample due to the presence of the underlying less defected third layer. Such the sensitivity of A'_1 modes to the adjacent layers in contrast to the E' mode are well known in MoS_2 lattice systems [26].

2.3.2 PL

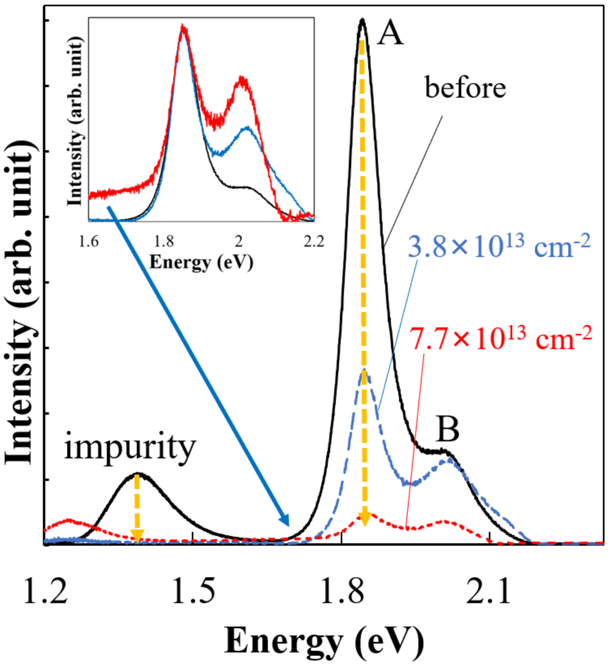

Fig. 2.10 PL spectra of 1L-MoS_2 samples irradiated with an Ar-ion beam at doses of 0, 3.8×10^{13}, and 7.7×10^{13} cm^{-2}. The inset shows spectra after normalized by A peak.

Fig. 2.10 shows the PL spectra of 1L-MoS_2 at each Ar-ion dose. In all spectra, the A (1.85 eV) and B (2.02 eV) peaks correspond to the emission between two spin-split subbands of 1L-MoS_2 [35]. The intensity of the A peak after Ar-ion irradiation decreased significantly with an increase in irradiation dose, and a tail (could be observed after normalization by A peak as shown in the inset) emerged on the lower-energy side in the highest dose (7.7×10^{13} cm^{-2}) as the blue arrow in the Fig. 2.10. The peak at approximately 1.35 eV, assigned to the emission related to impurity levels, also rapidly decreased in intensity upon ion-beam irradiation. When vacancies are introduced into MoS_2, new vacancy states with various energy eigenvalues are generated just below the conduction band in the gap, and the radiative relaxation of the excitons from various states generates a tail over a wide energy range for the A peak. However, nonradiative relaxation paths are also provided by the vacancy states introduced by ion-beam irradiation. Therefore, the emission from the deep impurity levels in the gap is suppressed, as is the main emission from the conduction band minimum at the K point (A peak). However, because the energy level associated with the B peak is unoccupied (in the spin-splitting sub-band structure), its photoemission is considered to be weaker than that of the A peak and insensitive to the change in the Fermi energy due to the presence of vacancies; therefore, it is less affected by the number of vacancies formed by irradiation (Table 2.2).

Table 2.2 B/A peak intensity ratio at various irradiation doses.

Irradiation dose (cm^{-2})	B/A (Intensity)
0	0.17
3.8×10^{13}	0.48
7.7×10^{13}	0.74

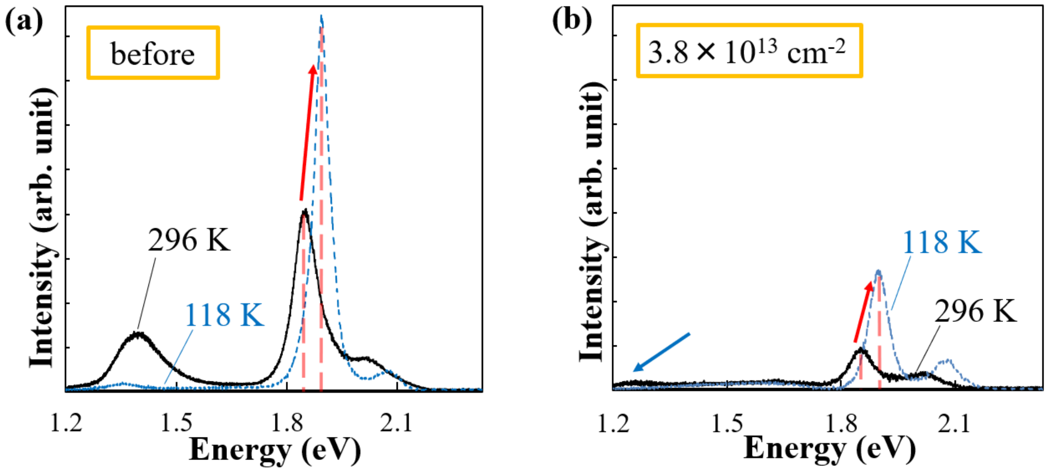

Fig. 2.11 PL spectra before (a) and after (b) irradiation at 296 and 118 K. The red and blue arrows denote the shift in the A and vacancy PL peaks, respectively.

The PL spectra of 1L-MoS_2 before and after Ar-ion irradiation with a dose of 3.8×10^{13} cm^{-2} at 296 and 118 K are shown in Fig. 2.11. An upshift is observed for both A (1.85 to 1.89 eV) and B (2.02 to 2.08 eV) peaks at 118 K compared with those at 296 K, indicating that the band gap increases owing to thermal shrinkage of the lattice. This can be explained by the Varshni relation, which describes the reduction of the bandgap in semiconductors with increasing temperature (Table 2.2) [78]:

$$E_g^T = E_g^0 - \frac{\alpha T^2}{T+\beta} \tag{2.1}$$

Using previously reported parameters for the A peak, where E_g^0 = 1.92 eV (band gap at 0 K), α = 0.001 eV/K, and β = 1090 K, it follows that E_g^{118} = 1.909 eV and E_g^{296} = 1.857 eV, which are consistent with our experimental results (Table 2.3). The reason for the minor difference in values observed at 118 K, with a slightly smaller measured value, is that the real temperature of the sample is slightly higher than that of the cooling stage sensor.

Table 2.3 A and B peak positions at 296 and 118 K, before and after irradiation.

	A peak (eV)		B peak (eV)		Δ(B-A) (eV)	
Temperature	118 K	296 K	118 K	296 K	118 K	296 K
Before	1.895	1.846	2.078	2.017	0.183	0.171
After	1.899	1.851	2.082	2.015	0.183	0.164

Additionally, the positions of the A and B peaks remained almost unchanged before and after irradiation, indicating that the ion-beam irradiation did not affect the bandgap of 1L-MoS_2, where the introduced vacancy provided only mid-gap states between the conduction and valence bands. The similar energy differences between the A and B peaks Δ(B-A) before and after irradiation indicate that the energy difference between the spin sub-bands also remained unchanged upon irradiation. The atomic character of Mo, with d-orbitals that have large spin-orbital coupling, mainly determines the spin-splitting in the energy bands of MoS_2 [35]. Thus, the energy difference of the sub-bands does not change by introducing S-vacancies in the lower dose region up to 3.8×10^{13} cm^{-1}.

The increase in the intensity of the A peak with decreasing temperature indicates that thermally activated nonradiative recombination is suppressed at low temperatures. Excitons in vacancies that have a significantly high binding energy may suppress thermally activated nonradiative recombination, including vacancy trapping, resulting in a very high PL quantum efficiency. Additionally, the increase in charge transfer between oxygen (likely during the cooling process) and MoS_2 containing S vacancies is also an important factor contributing to the enhancement of the properties of PL [79], even though the samples were sealed inside the cryostat-chamber with a temperature-control stage under a nitrogen gas atmosphere. This could also be verified in Fig. 2.14, which shows that oxidation in air after irradiation significantly increased PL intensity over four-fold.

The intensity of the impurity peak at approximately 1.35 eV before irradiation was greatly reduced at 118 K, indicating a negative thermal quenching (NTQ) of PL. Radiative relaxation disappears at low temperatures, a phenomenon that can be explained using the Shibata model [80]:

$$I(T) = I_0 \frac{1+Nexp\left(-\frac{E_n}{k_B T}\right)}{1+Dexp\left(-\frac{E_d}{k_B T}\right)}, \qquad (2.2)$$

where $I(T)$, I_0, E_d, and E_n denote the observed PL intensity, normalized factor of the emission, activation energy of non-radiative relaxation paths, energy difference between the emission levels (conduction band bottom or radiative vacancy levels), and non-radiative vacancy levels, respectively. N and D are phenomenologically adjustable parameters for fitting experimental results. The denominator indicates a normal enhancement of the PL intensity as temperature decreases regarding the suppression of non-radiative relaxations with an activation energy E_d. E_n describes the contribution of the thermal excitation of excitons to the emission levels from the non-radiative vacancy states in the lower energy region, which provides carriers to the emission levels as the temperature increases leading to the negative thermal quenching. Before irradiation, single S vacancies created during sample preparation (the exfoliation process in this study) caused shallower (approximately 0.1 eV) energy states with a smaller E_n [80] and result in the disappearance of the vacancy peaks at 118 K by negative thermal quenching. However, at higher irradiation doses, more vacancies are introduced to 1L-MoS_2, and the vacancy states in the electronic band are widened to lower electronic states [80]. Compared with a single S vacancy, which has a shallower energy state, the vacancy states for a pair of near S vacancies extend to approximately 0.3 eV, and their gap is approximately 1.4 and 1.2 eV, respectively [81]. In this case, the presence of additional vacancies widened the vacancy states. Additional radiative relaxation from the lower vacancy states to the ground state occurs, leading to a low-energy shift of the vacancy PL peak after irradiation, as shown as a blue arrow in Fig. 2.11 (b).

2.3.3 Oxidation

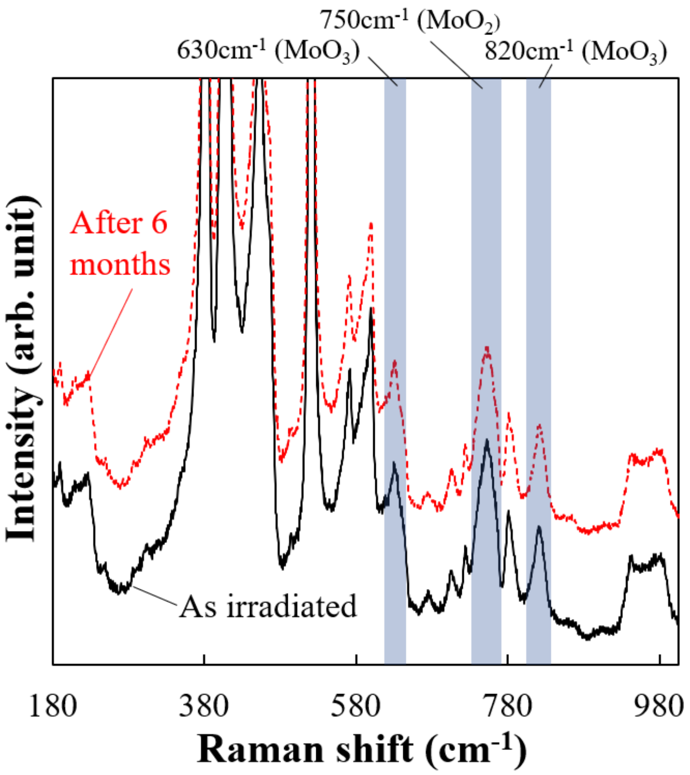

Fig. 2.12 Raman spectra before and after atmospheric exposure. The baselines of the spectra are shifted vertically to clarify.

The oxidation effects of the MoS_2 vacancies were observed by prolonged exposure of the irradiated sample to ambient conditions, where the atmospheric gas species adsorbed on the sample surface gradually underwent chemical reactions. The observed Raman spectra did not change after long-term exposure to air, as shown in Fig. 2.12–2.13, which indicates that oxidation due to atmospheric exposure does not significantly affect the lattice-vibrational properties of MoS_2.

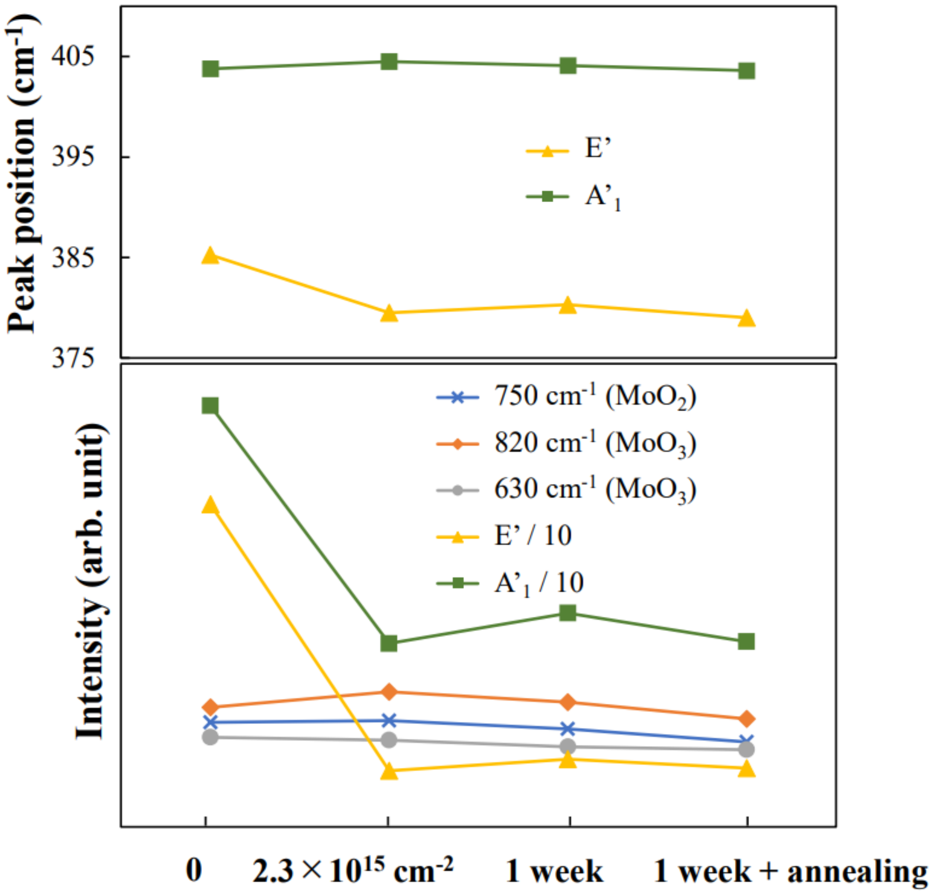

Fig. 2.13 MoS_2 peaks and molybdenum oxide peaks of 1L-MoS_2 before irradiation, just after irradiation at 2.3 × 10^{15} cm^{-2}, after 1 week of atmospheric exposure after irradiation, and annealed after the 1-week atmospheric exposure. The intensity of E' and A'_1 was multiplied by 1/10.

The intensities of the MoS_2 characteristic (A'_1 and E') and molybdenum oxide peaks [72] did not increase after atmospheric exposure for a long period of time after irradiation, and their intensities slightly decreased regardless of atmospheric exposure. Alternatively, it suggests that there was no large-scale oxidation process that could affect the lattice-vibrational properties of MoS_2.

In fact, in the case of some other study related to the oxidation of MoS_2 under laser beam, the MoS_2 could only be oxidized at the moment when it be irradiated. Since the defect of MoS_2 only take oxidation at high energy state, even exposed in air after irradiation, it would not be oxidized further. Since our experiments are taken in a high vacuum chamber, our MoS_2 sample did not have oxidation in and after irradiation, and this result also agree with that MoS_2 oxidation study.

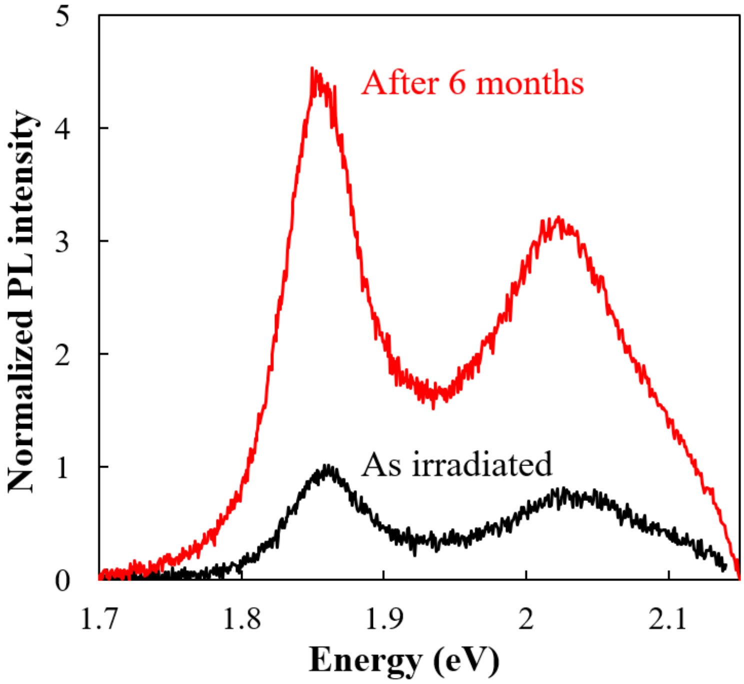

Fig. 2.14 PL spectra of 1L-MoS_2 irradiated at 3.8 × 10^{13} cm^{-2} before and after atmospheric exposure for 6 months. The vertical axis is normalized by the peak around 1.85 eV for the sample as irradiated.

The PL spectra of MoS_2 samples after 3.8 × 10^{13} cm^{-2} Ar-ion beam irradiation before and after long-term air exposure are shown in Fig. 2.14. The intensity of the spectrum increased four-fold after six months of atmospheric exposure due to the bonding between atmospheric oxygen and vacancies introduced by the ion irradiation, which gradually proceeds upon long-term air exposure. The charge transfer between oxygen and MoS_2 containing S vacancies is an essential factor contributing to the enhancement of PL [79]. The more charge transfer through the stronger interactions by forming the chemical bonding with oxygen caused more emission of MoS_2.

Here, it should be noted that the electronic properties are more sensitive to vacancies and their chemical reactions than the structural properties of MoS_2, such as the lattice dynamics as seen in the Raman spectra. This is also confirmed in the electronic conductivity shown later.

As shown in the Raman spectra, oxidation due to atmospheric exposure did not introduce new vacancies into the crystal structure of MoS_2. However, the vacancy sites introduced in a controlled manner by the ion beam were responsible for the reaction with oxygen. This suggests that a new vacancy level was generated by changing the chemical structure of the vacancy, although the fundamental crystal structure of MoS_2, which includes the density and distribution of vacancies that govern the lattice vibrational properties, remain unchanged.

2.3.4 FET Conductivity

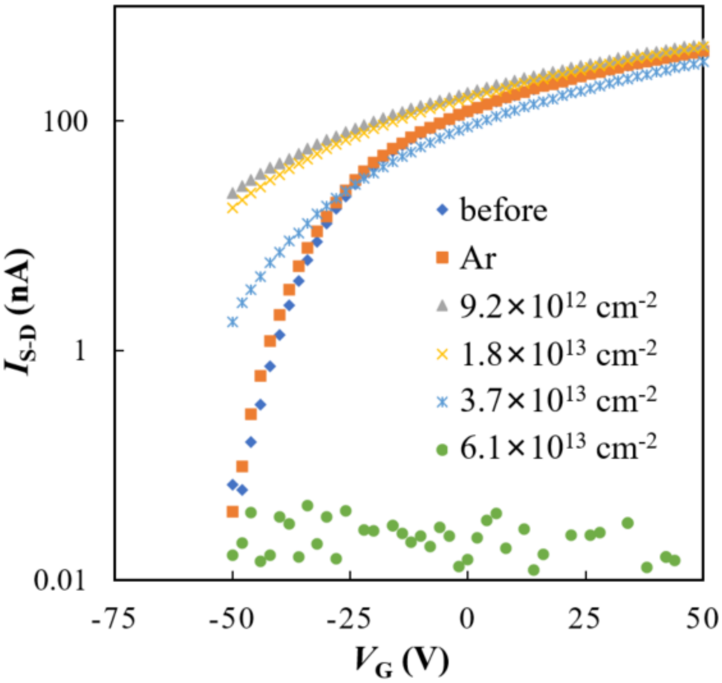

Fig. 2.15 FET conductivity at an irradiation dose of 9.2×10^{12}– 6.1×10^{13} cm^{-2}.

The $I_{S\text{-}D}$–V_G curves of 1L-MoS_2 before and after Ar gas introduction and after irradiation with 9.2×10^{12}– 6.1×10^{13} cm^{-2} doses are shown in Fig. 2.15. The introduction of Ar gas does not affect the electrical transport properties of the MoS_2 FET. However, a negative shift in V_G appeared after irradiation with an Ar-ion beam dose of 9.2×10^{12} cm^{-2}, which indicates that the electron doping of MoS_2 caused by vacancies occurs after the irradiation, together with minor decreases in carrier mobility. Additionally, both conductivity and carrier mobility decreased with increasing irradiation dose. This shows that S-vacancies introduced by irradiation, with lower doses up to 3.7×10^{13} cm^{-2}, increase the electrical conductivity to a certain extent because the isolated sulfur vacancies can collect electrons around it, and a higher number of sulfur vacancies indicates a smaller distance between vacancies. However, a large number of S vacancies can lead to the formation of clusters and interfere with electron motion, implying that the charge-trapping effect hinders electron mobility [40]. According to the photoluminescence measurements, irradiating Ar ion at a dose lower than 3.8×10^{13} cm^{-2} does not change the band gap but introduces mid-gap states below the conduction band, forming thermally excited electron carriers at room temperature. This is consistent with the lower influence of vacancies on carrier scattering and greater effect of carrier doping on conductivity in the lower dose region. The electronic properties are more sensitive to the introduction of vacancies than the structural properties. Indeed, electron conductivity was significantly reduced and the FET device did not work after irradiation with a dose of 6.1×10^{13} cm^{-2}. However, the Raman spectrum did not change significantly. The sensitivity of the electronic properties to the introduction of vacancies is also seen in the PL spectra shown in Fig. 2.10, where a significant decrease in spectral intensity is observed at a dose of 7.7×10^{13} cm^{-2}.

2.4 Conclusion

Although ion-beam irradiation is a proper modification tool, it still remains challenging to apply to 2D materials. In this study, the effects of the Ar-ion beam irradiation on the structure and electronic properties of 1L-MoS_2 were evaluated by a combination of Raman spectroscopy, PL, and FET conductivity on samples similarly prepared. Raman spectroscopy and conductivity measurements reveal that the vacancies are introduced in the order of S, Mo, and MoS_6 in a controlled manner by low-energy Ar-ion beam irradiation at the lower ion-beam dose region and causing electron doping. According to PL, irradiating Ar ion at a lower dose of less than 3.8×10^{13} cm^{-2} does not change the band gap but introduces mid-gap states below the conduction band, generating thermally excited electron carriers at room temperature.

This study compares several measurement methods to confirm the mechanism of vacancy formation in MoS_2 and summarizes the effect of vacancy in various aspects of characterization. These results can provide a reference for future research and applications of 2D materials and support a tool for device quality and damage evaluation in fabrication and radiative environmental application.

Chapter 3 Au- or I-ion irradiation on Graphene

3.1 Introduction

Graphene in its isolated form is a promising material for applications in next-generation electronic devices; however, a strategy for modifying graphene to tune its carrier transport properties to meet the various requirements related to carrier density, electron mobility, and spin-orbit coupling in needed. In this study, we have modified graphene by irradiating it with an Au- or I-ion beams at 200 keV with doses of 10^{13}–10^{14} cm^{-2} using a NaCl sacrificial layer to introduce ions as guest chemical species into a two-dimensional graphene sheet as a quantitative chemical modification method. Ion-irradiated graphene was evaluated by Raman spectroscopy, electrical conductivity measurements, and Rutherford backscattering spectrometry after removing the sacrificial layer. Both carbon vacancies and heavy atoms (Au, I) are introduced into graphene by ion-beam irradiation; the introduced heavy atoms act as charged impurities, which resulted in the Raman D' band and the downshift of the Fermi energy caused by hole carrier doping. The clarified knowledge of the influence of heavy-ion beam irradiation of graphene on electron transport properties will lead to the development of a new class of materials for electronics and spintronics.

This chapter is based on the journal papers published in 2024 [51].

3.1.1 Graphene

Graphene, the fundamental structure of carbon materials, is a two-dimensional (2D) material consisting of carbon atoms arranged in a honeycomb lattice. Recently, graphene has attracted considerable research attention since it was exfoliated as an atomically thin monolayer from bulk graphite two decades ago [1][3]. Further, graphene is a potential candidate for application in next-generation electronic devices [58][82], magnets [83][84], and catalysts [85][86] owing to its properties, such as high mechanical flexibility, abundance, thermal conductivity, and carrier mobility. Atoms inside the graphene layer are bonded by sp^2 orbital hybridization, and van der Waals-like forces join the layers in bulk graphite. This structural feature allows isolating the graphene sheet into an individual monolayer of graphite via the scotch-tape exfoliation method, which is initially used to fabricate graphene [1].

The electronic properties of graphene need to be modified to apply it to the field of future electronic devices; however, tuning the charge carrier density and carrier scattering (mobility) remains a major challenge. Further, tuning the spin-orbital interactions in addition to carrier density and scattering is important to apply graphene to future spintronics devices. Graphene is an all-carbon material with lightweight atoms; therefore, its spin-orbit interaction is negligible. Consequently, it is meaningful to investigate the experimental introduction of spin-orbital coupling into graphene [78]. A past study found that the spin–orbit coupling was much enhanced in Au-intercalated graphene on Co(0001) [87]. The energy scale of spin-orbital coupling is proportional to the quartic charge of the nuclei in an atom [88], and therefore, introducing heavier atoms into graphene is an appropriate strategy for tuning spin-orbital coupling.

3.1.2 Ion beam irradiation with sacrificial layer

Graphene undergoes a remarkable change in its electronic states even when a tiny number of guest atoms or molecules are introduced owing to its intrinsic 2D structure where all atoms belong to the surface [3]. In this viewpoint, several attempts have been made to overcome the abovementioned challenges to add new functionality via graphene-hosted host–guest interactions. Fabricating a back-gate-type field-effect transistor (FET) is widely used as a probing method to evaluate the effect of introducing guest chemical species into graphene. For example, the hole doping of graphene has been reported using the FET structure of graphene after introducing guest oxygen molecules [38]. Thus far, various approaches have been explored for introducing guest species into graphene, which include adsorption onto adlayers, intercalation between 2D graphene sheets [47], and direct incorporation of foreign atoms into the graphene sheet [48]. Among these methods, the direct modulation of graphene's electronic properties and structure via ion beam irradiation is an appropriate technique for precisely controlling the number of guest chemical species [49][50], where charges of the injected ions in the sample are simultaneously neutralized upon irradiation. Here, we would note that atoms introduced by the ion beam exist in the same chemical states as those introduced by other impurity engineering methods, such as additives in material synthesis, wherein the net charge of the entire sample is electrically neutral after irradiation if no electric field is applied.

Here, it should be noted that the irradiating energy of ions to tune 2D materials like graphene makes it easy for high-energy ions to penetrate through the thin-layer structures of 2D materials. The high-energy ions can not only introduce large voids but can also not stay at a depth at which 2D materials are located [60]. In a previous study, the ion-beam energy was reduced to ~100 eV for introducing atomic-scale vacancies in 2D materials when irradiated with easily ionized noble gas ions [7]. However, relatively high energy for ions of approximately several tens of kilo electron volts to million electron volts is applied [44][45][46][59] because of the limitation of an ion-generating instrument with a solid source such as a tandem accelerator.

To solve this problem, we successfully developed a new method that uses a sacrificial layer to stop ions on the surface of 2D materials, including graphene, where the sacrificial layer on graphene decelerates the ions and reduces the irradiation energy for distributing irradiated ions at the graphene surface [61]. Further, we examined several materials such as a photoresist, ZnO, and NaCl, and we found that a Cr/NaCl vacuum-deposited layer is the optimal solution for the sacrificial layer, which was a minimal influence on 2D materials and easily removable by boiling water with fewer charging problems during ion-beam irradiation. In the proposed method, the thickness of the sacrificial layer was calculated to ensure that the ions accurately reached the graphene surface without excessive energy. Namely, the “Stopping and Range of Ions in Matter” (SRIM) simulation program—a statistical algorithm similar to the Monte Carlo method—was used to simulate the stopping and range of ions in matter [23] to estimate the thickness of the sacrificial layer.

3.1.3 Objective of chapter 3

Although the developed NaCl sacrificial layer method is promising for achieving intrinsic defect engineering in 2D materials by ion implantation, this approach has several challenges. In the previous study, the absolute value of the exact number of ions that arrived in the sample in the actual experiment of ion-beam irradiation is unknown, thereby causing a loss in the quantitative introduction of guest species, which is one of the most significant advantages of ion irradiation for chemical modification.

In this study, considering their spin-orbital interactions, we modulated graphene's electronic properties and structure using the ion-beam irradiation method with Au and I ions. A NaCl sacrificial layer formed on graphene before irradiation and was removed after irradiation. The densities of Au or I ion remaining on the surface of the substrate were determined by Rutherford backscattering spectrometry (RBS) owing to their higher reflected energy. The structure of graphene was evaluated using Raman spectroscopy. The changes in the electrical properties of graphene, which include the characteristics of the carrier-scattering sources, were investigated along with conductivity measurements performed using FET devices.

3.2 Experimental

3.2.1 Sample fabrication

Monolayer graphene samples were fabricated via the mechanical exfoliation of highly oriented pyrolytic graphite (HOPG, GE, ZYB). Then, it was transferred to the surface of a SiO_2 (285 nm)/Si substrate obtained by thermal oxidation treatment. The typical scale of the monolayer sample was 10–20 μm. The number of layers was evaluated using the brightness contrast of the optical microscopy (OM) images [13] and Raman spectroscopy [21].

3.3.2 Monte Carlo simulation

The distribution of stopping ions and damage to the lattice (vacancies) in the target materials were simulated using "Detailed Calculation with full Damage Cascades" in the TRIM program in the SRIM2013 package [53] with Au or I as incident ion on a target slab model that consists of Cr (10 nm)/NaCl/C (0.3 nm)/SiO_2 (285 nm). The Si layer in the target was not considered because all ions stopped before the rear end of the SiO_2 layer, and therefore, the Si layer did not affect the simulation results. A simulation was performed using 40000 incident ions with a 200 keV energy for irradiating the target.

3.3.3 Deposition of sacrificial layer

Three types of film materials were examined to select the most appropriate sacrificial layer suitable for graphene. The photoresist, ZnO, and NaCl film were chosen for sacrificial layer evaluation.

Photoresist diluted with butyl acetate as a solvent to control film thickness was coated using a spin coater. Detailed process conditions are shown in Table 3.1. ZnO and Cr/NaCl thin film was deposited at a rate of ~0.02 nm/s in vacuum conditions (~10^{-4} Pa) by a resistive heating evaporation system (VPC-260, ULVAC). Based on the thickness estimation by the Monte Carlo simulation, the thickness of photoresist, ZnO, and Cr/NaCl film was fixed at 140 nm, 68 nm, and 10/200 nm, respectively. The topmost Cr layer was deposited at a rate of ~0.03 nm/s with a fixed thickness (10 nm) to avoid the charging-up effects during the ion-beam irradiation.

Table 3.1 Process conditions for photoresist-based sacrificial layer formation.

Cap layer	OAP (Tokyo Ohka Inc.)
Photoresist	TSMR-8900LR (Tokyo Ohka Inc.)
Cap layer coating	OAP Spin coat(1000 rpm 5 sec → 4000 rpm 30 sec)
HMDS process	Baking(70°C 2 min)
Photoresist coating	TSMR-8900LR Spin Coat(1000 rpm 5 sec → 4000 rpm 30 sec)

3.3.4 Ion beam irradiation

A tandem accelerator (Research Center of Ion Beam Technology, Hosei University) was used for irradiating Au or I ion at an acceleration voltage of 200 keV, which is the lowest energy condition for the practical usage of an ion beam in this system, at doses of 10^{13} cm^{-2} (for Au ion) and 10^{14} cm^{-2} (for Au and I ions). We used a dose of 10^{14} cm^{-2} to obtain a sufficient number of ions for detection by RBS. Using a raster scan operation, the ion-beam irradiated the entire SiO_2/Si substrate that supports graphene. We only applied a 10^{14} cm^{-2} dose of the I-ion beam because the higher intensity of the I-ion beam made it difficult to achieve homogeneous irradiation into substrates in a short time for the smaller dose condition. After irradiation, the Cr/NaCl layer was removed and rinsed by boiling deionized water before all sample characterization measurements.

3.3.5 Sample characterization

3.3.5.1 Rutherford backscattering spectrometry

The RBS measurements were performed using a Van de Graaff accelerator (High-voltage Engineering AN2500, Research Center of Ion Beam Technology, Hosei University). The accelerator generated a He-ion beam focused on a spot diameter of 2 mm at an accelerating voltage of 1500 keV. The normal direction of the samples was tilted by 7° with respect to the beam incidence direction. The detector for the backscattered ions was located at 153° with respect to the incident direction of the beam. The measurement was performed under bias voltages of 200 V and 50 V for the samples and the RBS detector, respectively, with an accumulation of ionic charge up to 150 nC, repeated 26 times.

3.3.5.2 Raman spectroscopy

Raman spectroscopy measurements were performed on graphene samples using a microscopic spectrometer (LabRAM HR Evolution, HORIBA) before and after ion-beam irradiation at an excitation laser wavelength of 532 nm under atmospheric conditions at room temperature. The excitation laser spot had a diameter of 2 μm, almost similar to the measured sample area.

3.3.5.3 Conductivity measurement

The FET structure for conductivity measurements was formed before sacrificial layer deposition. EB drawing equipment (ELS-7500, ELIONIX) was used to fabricate electrodes designed according to the size and position of the graphene on a layer of polymer resist (ZEP520A, ZEON, JAPAN). The width of the source and drain electrodes was 1 μm, and the gap between the two terminals was 2 μm. Further, Cr/Au (1/10 nm) and Cr (15 nm) for the source drain and the gate electrodes, respectively, were deposited under high-vacuum conditions (VPC-260, ULVAC) at a pressure of 10^{-4} Pa. FET conductivity measurements were performed using two electronic source meters (2400A, Keithley) before and after ion-beam irradiation in a high-vacuum chamber with a heating stage. The device was pre-annealed at 200 °C for five h at a pressure of 5×10^{-4} Pa to prevent gas adsorption and ensure optimal ohmic contact between the electrodes and graphene. The resistance was measured at the gate voltage, which varied between −40 and +40 V in 5 V steps, and then, the conductivity curve was calculated using the reciprocal of its resistivity.

3.3 Results and discussion

3.3.1 Evaluation of sacrificial layer

After Au-ion irradiation, each kind of sacrificial layer should be removed before next procedure. In this case, the protection performance and the damage introduced by sacrificial layer is an important characteristic for each sacrificial material and should be evaluated before application.

3.3.1.1 Photoresist thin film

After Au-ion irradiation, the sacrificial layer was attempted to be removed with acetone and piranha solution; however, it was found that almost unable to be removed from the substrate. Raman spectroscopy was performed before and after Au-ion irradiation to evaluate the characteristic of graphene.

The G and G' band, which are characteristic bands for graphene, disappeared after irradiation as shown in Fig. 3.1. A broad peak in G-band region was detected from the unremovable photoresist film covering the substrate after irradiation. This broad peak is corresponding to amorphous carbon. The optical image and Raman intensity mapping of graphene sample are shown in Fig. 3.2. Here, it can be found that the characteristic band of graphene significantly changed after irradiation, and the detected Raman intensity in this region after irradiation was generated from the unremovable photoresist. This is attributed to high energy beam during Au-ion irradiation which lead to the crosslinking reaction and carbonization between polymer chains inside the photoresist. This change resulted in the difficulty for removing the sacrificial layer after irradiation because of the strong bonding between the substrate and photoresist.

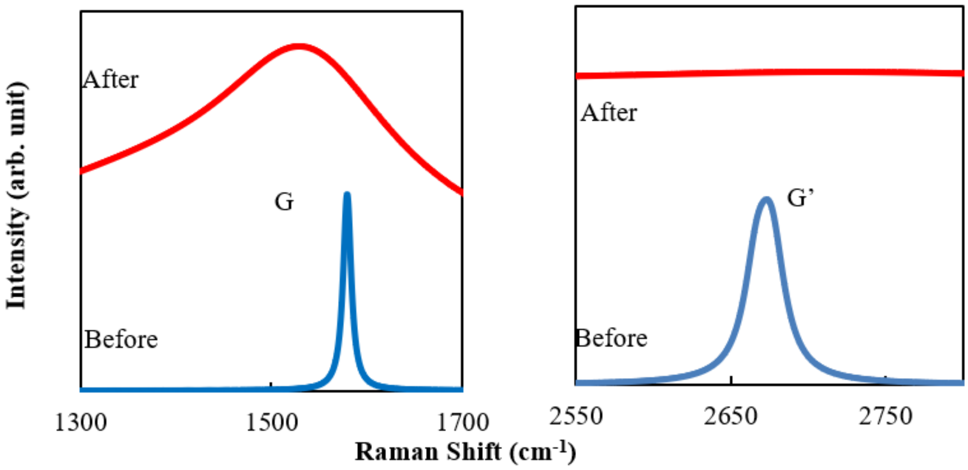

Fig. 3.1 Raman spectra of graphene before and after Au-ion irradiation with photo resist sacrificial layer

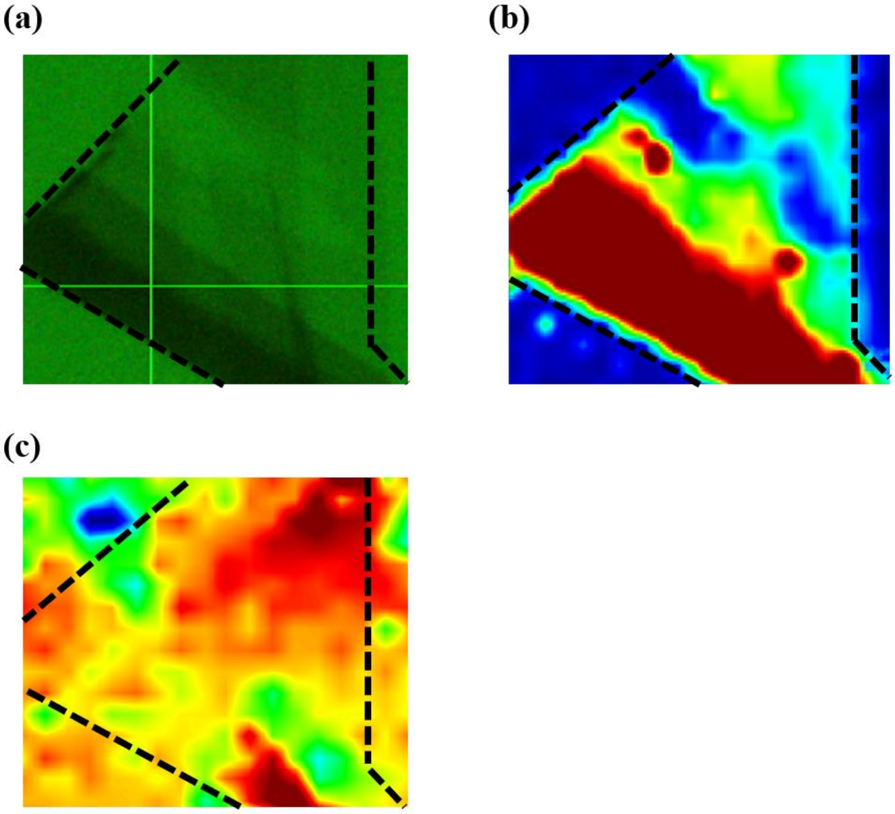

Fig. 3.2 (a) Optical image of graphene (b) Raman mapping of G band intensity before and (c) after Au-ion irradiation

3.3.1.2 ZnO thin film

ZnO film was also be evaluated because it can be removed with HCL solution. Unlike photoresist layer, it can be removed even after Au-ion irradiation. Unfortunately, ZnO also have a problem in the application of sacrificial layer. The Raman spectra of graphene before and after ZnO deposition are shown in Fig. 3.3. It can be found that D band corresponding to the presence of defect in graphene was introduced even without irradiation, which means only ZnO deposition is harmful for graphene. On the other hand, G band disappeared after irradiation means ZnO layer cannot support sufficient protection from Au-ion irradiation. Fig. 3.4 shows that the I_D/I_G ratio, which corresponding to the damage of graphene, becomes higher as the layer number decreases after ZnO deposition, indicating that the topmost layer of graphene is damaged after irradiation.

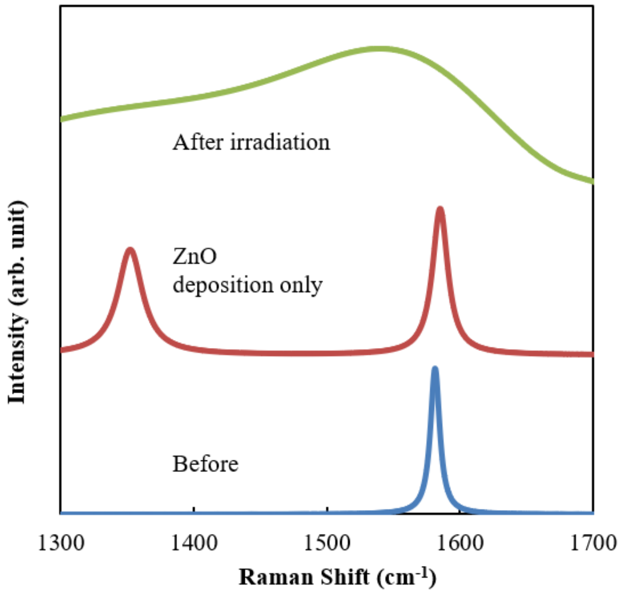

Fig. 3.3 Raman Spectra of graphene before and after ZnO deposition, and after Au-ion irradiation.

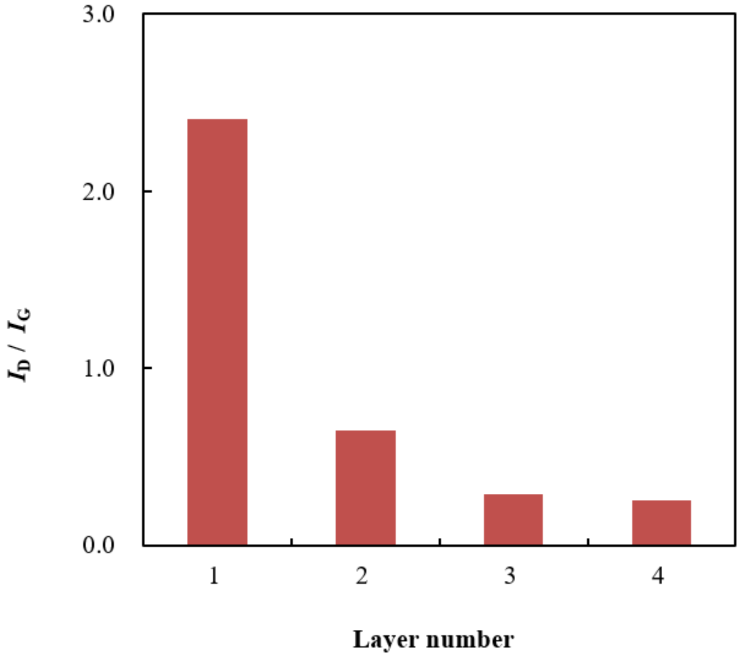

Fig. 3.4 I_D/I_G ratio of graphene after ZnO deposition

3.3.1.3 NaCl thin film

NaCl layer can be easily removed with hot water after deposited on the substrate with graphene samples. After the deposition and removal processes of Cr/NaCl sacrificial layer, the D band was negligible, and only minor change appears in the characteristic of graphene Raman spectra, as shown in Table 3.2 and Fig. 3.5 (a).

Table 3.2 Raman Spectra of graphene before/after NaCl deposition

	G position (cm^{-1})	I_D/I_G	$I_{G'}/I_G$	FWHM
Before	1582.7	0	5.26	6.12
After	1582.3	0.05	4.58	8.52

Additionally, because graphene has remarkable change in its electronic states even due to very tiny amount of atomic or molecular adsorption, a back gate type FET is usually used to evaluate the electronic properties of graphene, and hole doping into graphene is reported by introducing oxygen molecules as a guest [38]. Fig. 3.5 (b) shows the gate voltage dependence of the electric conductivity of graphene before deposition and after removal of Cr/NaCl layer. The V_{CNP} and mobility of the transfer curve has almost no change, indicating that the electronic properties of graphene are not affected by the deposition or removal process of Cr/NaCl layer [61].

Both Raman and FET conductivity measurement suggest that the deposition and removing of NaCl would not affect the electronic properties of graphene. From the above, NaCl is the most appropriate material for sacrificial layer and was applied to protect graphene from ion-beam irradiation. Also, we found that NaCl is also proper sacrificial layer material for MoS_2 and TaS_2 in the case of high-energy irradiation.

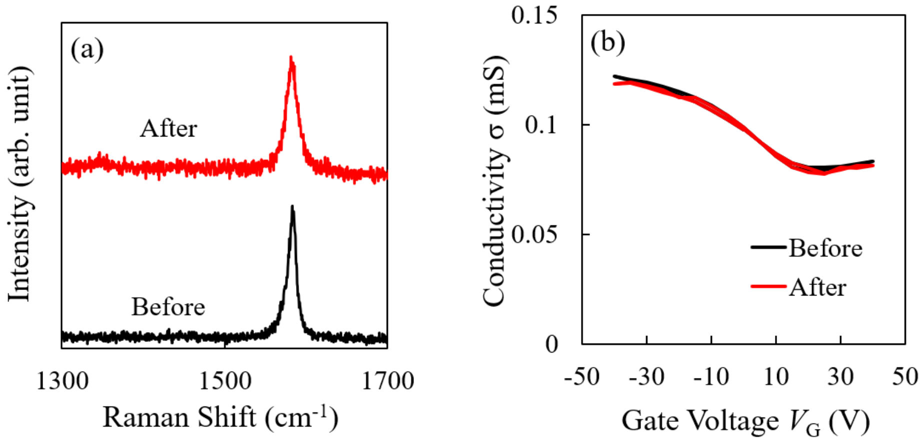

Fig 3.5 (a)Raman spectra and (b) electron conductivity of graphene before NaCl deposition and after removal [61]

3.3.2 TRIM simulation

Fig. 3.6 shows the simulation result of 200 keV Au- and I-ion irradiation to a Cr (10 nm)/NaCl (200 nm)/C (0.3 nm)/SiO_2 (285 nm) target by TRIM program, for estimation of stopping range of Au and I ions in the Cr/NaCl sacrificial layer and graphene based on classical atomic collisions. The Si layer in target is not considered here since all the ions stopped before the rear end of SiO_2 layer, so Si layer does not affect the simulation result. Ion range (distribution of incident ions) and damage distribution (density of vacancy created when the target atom has a collision with incident ion or recoil atom) of Au or I ion demonstrate that the optimal thickness for NaCl layer is 200 nm in our condition. With this film thickness, the layer can keep the ion distribution at the graphene position, and the avoidance of damage on the graphene sample due to the formation of vacancies can be estimated.

The optimal thickness for the NaCl layer is estimated as 200 nm for both Au- and I-ion beam irradiations at 200 keV by calculating the stopping range of Au or I ion in the Cr/NaCl sacrificial layer and graphene based on classical atomic collisions using the TRIM program in the same manner as the previous study for irradiating B or N ion to graphene [61]. With this film thickness, the NaCl layer maintained the irradiated ion distribution at the graphene position and avoided damage to the graphene sample because of the formation of vacancies.

A thickness of only 200 nm is sufficient for decelerating Au and I ions with an energy of 200 keV, compared to B and N ions with the same ion acceleration energy studied in the past report, which require 1200 and 1000 nm of NaCl as sacrificial layers [61]. The difference is explained by the stopping power of the target materials against incident ions [89][42][90][91]. The energy loss of incident ions is mainly attributed to the electronic stopping power caused by the dynamic response of electrons inside target materials against the positive charge of penetrating ions for high-energy ion beams of approximately several million electron volts, which are applied to the chemical modifications of materials. However, the electronic stopping power is proportional to the total charge of the nuclei and the velocity of the incident ion, which results in more minor contribution and similar orders of magnitude of the stopping powers in the B, N, Au, and I ions at a fixed acceleration voltage of 200 keV. On the other hand, the nuclear stopping power induced by elastic collisions between the incident ions and atoms of the target materials is significantly larger for heavier ions, which becomes significant at a beam energy scale of 200 keV. The nuclear stopping power is almost an order of magnitude larger than the electronic stopping power for Au and I ions at ~200 keV, which is in contrast to the smaller nuclear stopping power for B and N ions in the same energy range. The considerably larger nuclear stopping powers of the heavier Au and I ions indicate more collisions and the formation of vacancies in the lattice of the target materials. Indeed, the vacancies of C atoms were formed in the graphene position with Au- or I-ion irradiation, which is in contrast to the negligible (approximately three orders of the smaller ratio to the density of introduced ions, as shown in Table 3.3) vacancy formation in the simulation results for B- and N-ions irradiation. This implies a higher possibility of defect introduction into graphene for heavier Au- or I-ion irradiation.

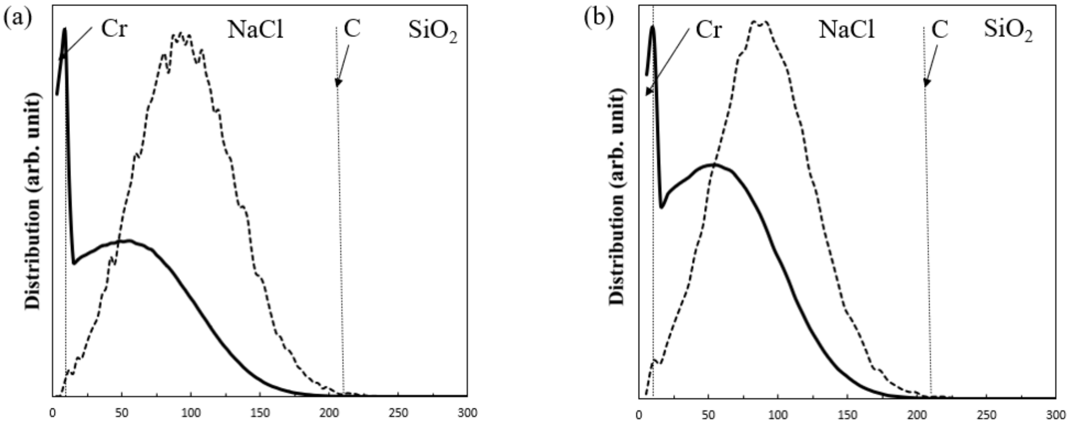

Fig. 3.6 Distribution of ions (solid curve) and vacancies (dotted curve) vs depth from the target sample surface with (a) Au- and (b) I-ion beams with beam energy of 200 keV, calculated by TRIM simulation. The vertical dashed lines denote the boundaries of each target layer.

Table 3.3 Ion and vacancy density at graphene position

Ion species	B	N	Au	I
Ion density	8.00E+02	9.20E+02	9.20E+02	4.90E+02
Vacancy	1.60E-05	3.70E-05	1.40E-02	4.00E-03
Vacancy/Ion	2.00E-08	4.00E-08	1.60E-05	8.20E-06

3.3.3 RBS

Fig. 3.7 shows the RBS spectra measured for the graphene samples on the Si/SiO_2 substrate irradiated with Au or I ion at a dose of 10^{14} cm^{-2}, where the contribution of graphene was not detectable because of the large detection area of the measurement (beam diameter: ~ 2 mm), when compared with the size of graphene flakes. Noticeable peaks appeared on the high-energy side for both the Au and I conditions. The peaks at approximately 1400 keV and 1300 keV represent energies reflected by the Au and I atoms, respectively. The charges of injected ions in the sample are neutralized simultaneously on irradiation with a beam current flowing through the sample holder and instruments, regardless of the sign of the charge of the irradiated ions [42]. Further, the wide energy band below 1200 keV indicates the presence of Cu, which could have originated from the Cu sample holder and pressing sticks for fixation. Here, it should be noted that the RBS measurements for Au- and I-ion-irradiated substrate are performed under different experimental parameters due to the maintenance and adjustment of the instrument. The raw spectra are different even for the same material, and they cannot be compared with each other directly. After the irradiation of both Au and I ions into the sample covered with the optimized thickness of the NaCl sacrificial layer (200 nm) at doses of 10^{14} cm^{-2}, approximately 2.1×10^{13} cm^{-2} of Au atoms and 1.2×10^{13} cm^{-2} of I atoms were detected by RBS on the sample surface after removing the NaCl layers. We assume that 2.1×10^{12} cm^{-2} of Au atoms at the graphene surface at an Au-ion dose of 10^{13} cm^{-2} because the number of atoms reaching the sample surface is proportional to the total number of atoms.

The absolute value of the exact number of ions that arrive at the sample in the actual experiment of ion-beam irradiation was unknown in a previous study although the number of ions is mandatory information for the discussion to comprehensively investigate the effects of the introduced ions. Heavier ions are used in this study for beam irradiation, and therefore, using the RBS to measure the density of ions remaining on the surface of the substrate becomes possible because of its higher reflected energy, which can be separated from the substrate material.

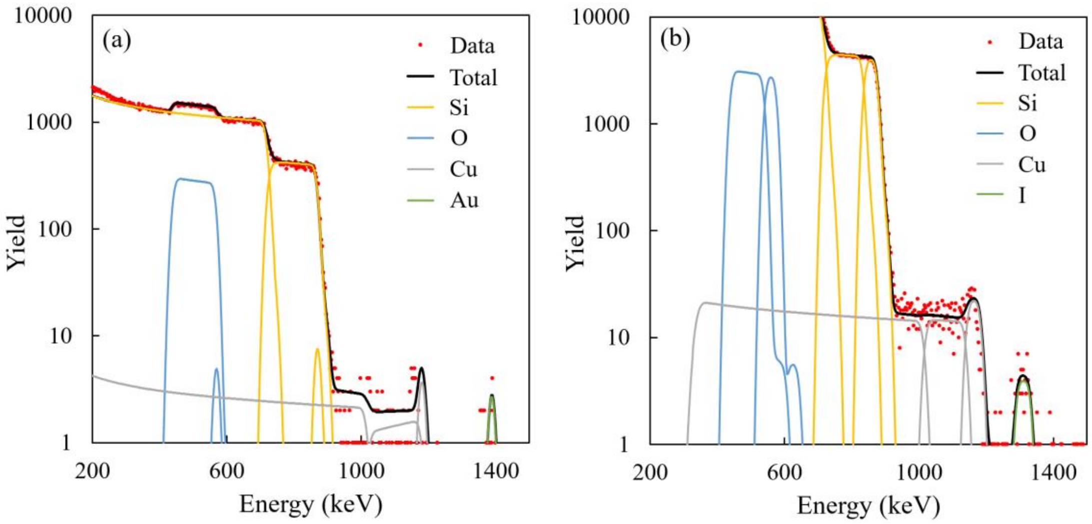

Fig. 3.7 RBS spectra of (a) Au- and (b) I-ion-irradiated substrate. Yellow-, blue- and grey-colored lines denote the fitting curves for Si, O, and Cu atoms, respectively. The

isolated peak at the high energy side (1300 keV and 1400 keV) fitted by green line in (a) and (b) represents Au and I atoms, respectively.

3.3.4 Raman spectroscopy

The Raman spectra of graphene before and after Au-ion irradiation at doses of 10^{13} and 10^{14} cm^{-2}, and I-ion irradiation at a dose of 10^{14} cm^{-2} are shown in Fig. 3.8. The G (at ~1580 cm^{-1}) and G' (at ~2670 cm^{-1}) bands peculiar to graphene were observed clearly even after Au- or I-ion irradiation, which confirmed that graphene was modified by Au- or I-ion irradiation while maintaining the basic structure of the graphene honeycomb lattice. The presence of lattice vacancies and ionic impurities provide a sharp and shallow scattering potential for conduction carriers in graphene, which causes D (at ~1340 cm^{-1}) and D' (at ~1622 cm^{-1}) bands in the Raman spectrum, in addition to the G and G' bands [41]. The Raman spectra of graphene after Au- or I-ion irradiation exhibited both D and D' bands, thereby indicating the introduction of not only charged Au or I species as impurities but also vacancies. The D and D' bands in the Raman spectra were small or unnoticeable after irradiating B or N ion, which implies that these elemental species were introduced successfully into the graphene layer without creating vacancies [61]. The slow-light elemental ions reach graphene without introducing vacancies because their stopping power is decreased significantly. However, a significant D band appeared after heavier Au- or I-ion irradiation, and it can be attributed to the considerably heavier Au or I atoms. These results agree well with the TRIM simulation results.

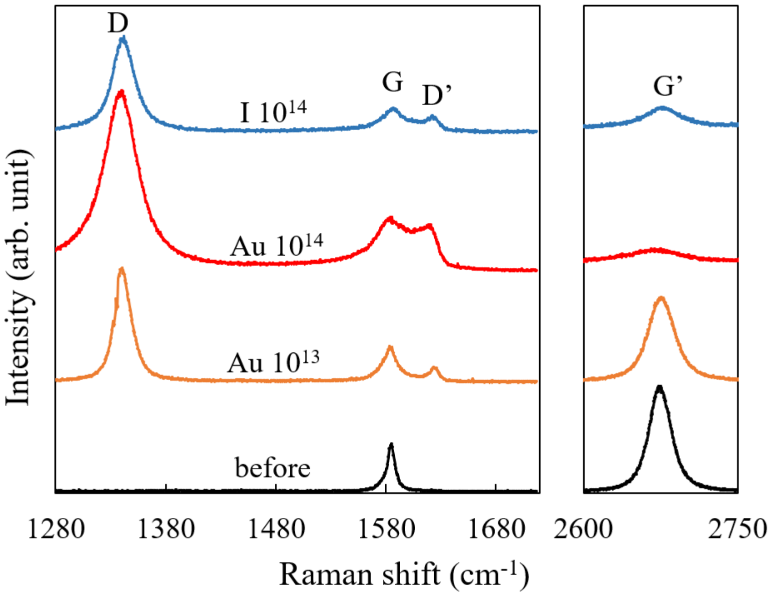

Fig. 3.8 Raman spectra in the G/D band regions (left) and G' band region (right) of graphene before irradiation (before), after Au-ion irradiation at a dose of 10^{13} cm^{-2} (Au 10^{13}), after Au-ion irradiation at a dose of 10^{14} cm^{-2} (Au 10^{14}), and after I-ion irradiation at a dose of 10^{14} cm^{-2} (I 10^{14}). The vertical axes are shifted in each spectrum for clarity.

Figs. 3.9 (a) and (b) show the averaged G band position and full width at half maximum (FWHM) before and after Au- or I-ion irradiation at doses of 10^{13} and 10^{14} cm^{-2}. The G band position of the Au-ion-irradiated graphene at both doses caused a downward shift, and the FWHM increased to over twice that of the pristine sample after irradiation at a dose of 10^{13} cm^{-2}. It was over five times larger than that of the pristine sample after Au-ion irradiation at a dose of 10^{14} cm^{-2}. For I-ion irradiation, the G-band position seems slightly upshifted; however, its FWHM was over four times larger than that of the pristine sample. These results are reminiscent of the changes in the Fermi level after irradiation; however, graphene with hole or electron doping exhibits an upward shift in the G-band position and a large decrease in linewidth [41], and the observed Raman results seem contradictory. In addition, the ratio of the G' band to the G band shown in Fig. 3.9 (c) increases after irradiation with Au ion at a dose of 10^{13} cm^{-2}, which should be lowered by the carrier doping of graphene. This behavior can be attributed to the softening of the graphene honeycomb lattice by the strain introduced by the ion-beam irradiation [56][61]. Indeed, the ratio of the G' band to the G band significantly reduced after a larger irradiation dose of Au or I ion at 10^{14} cm^{-2}, which suggests that the significant introduction of the lattice deformation suppresses the G' band, which is more sensitive to the presence of the disorder in the graphene honeycomb lattice than G band [3]. The effects of the strain in graphene introduced by Au- or I-ion irradiation on the G and G' bands of the Raman spectra is more than that of the doping by introduced Au or I species, which screens out more minor influences caused by charge doping. The slight upshift in the G-band position in the I-ion-irradiated graphene suggests a less strain and more doping effects than those in the case of Au-ion irradiation. This is also supported by that the D' band caused by the shallow scattering potentials by charged dopant impurities is the largest in the I-ion-irradiated graphene, as shown in Fig. 3.9 (d).

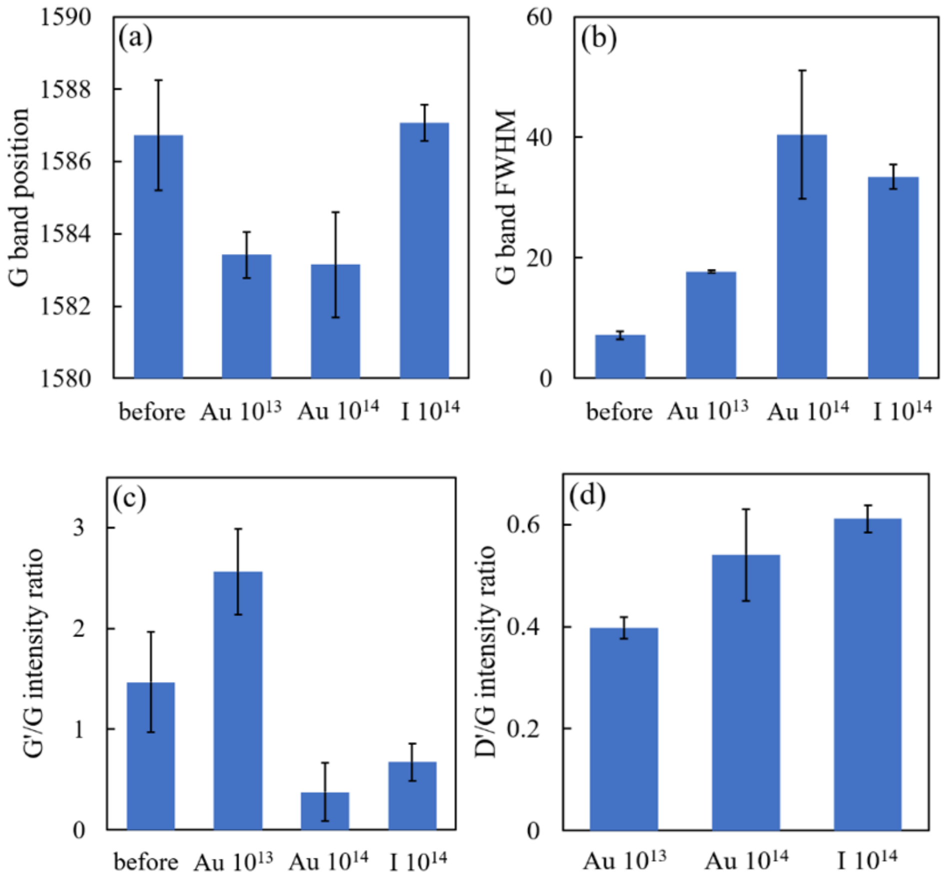

Fig. 3.9 Raman peak fitting parameters of graphene before irradiation (before), after Au-ion irradiation at a dose of 10^{13} cm^{-2} (Au 10^{13}), after Au-ion irradiation at a dose of 10^{14} cm^{-2} (Au 10^{14}), and after I-ion irradiation at a dose of 10^{14} cm^{-2} (I 10^{14}) for (a) G band position, (b) G band full width half maximum (FWHM), (c) ratio of the G' band to the G band intensity, (d) ratio of the D' band to the G band intensity

3.3.5 FET Conductivity

The actual change in Fermi energy caused by the charge doping of graphene upon ion-beam irradiation was clarified by the electrical conductivity. Fig. 3.10 shows the gate voltage dependence of electric conductivity for graphene before and after Au- or I-ion irradiation. After irradiation at a dose of 10^{13} cm^{-2}, graphene showed a hole-doping behavior with a 30 V positive shift in the charge neutral point V_{CNP} compared to that of pristine graphene before irradiation. Moreover, it causes a higher positive shift in graphene irradiated by the Au- or I-ion beam at a dose of 10^{14} cm^{-2}, where V_{CNP} corresponding to the position of the Dirac point of the electronic band structure of graphene is out of the ±40 V range of the gate voltage, which is experimentally observable, indicating the larger degree of hole-doping nature at a dose of 10^{14} cm^{-2}.

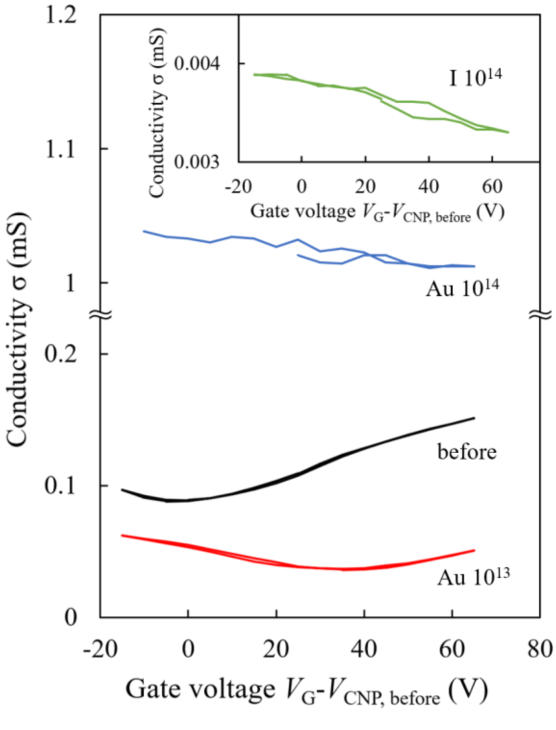

Fig. 3.10 Electrical conductivity σ versus gate voltage shift $V_g - V_{\mathrm{CNP,\,before}}$ of graphene FET before irradiation (before), after Au-ion irradiation at a dose of 10^{13} cm^{-2} (Au 10^{13}), and after Au-ion irradiation at a dose of 10^{14} cm^{-2} (Au ion 10^{14}). The inset shows the graphene after I-ion irradiation at a dose of 10^{14} cm^{-2} (I 10^{14}). The conductivity for Au-ion-irradiated graphene at a dose of 10^{14} cm^{-2} that appears considerably up shifted because of the differences in the contact resistance among the two-terminals FET devices, which provides the shift of baselines.

The doped carrier density n by the ion-beam irradiation can be calculated using the value of the shift of the gate voltage ΔV_{CNP} as

$$n = \frac{C_{\mathrm{g}}}{e} \Delta V_{\mathrm{CNP}} = \alpha \Delta V_{\mathrm{CNP}}, \tag{3.1}$$

where e, C_{g} represent the elementary charge, the capacitance of the gate per unit area calculated by $\varepsilon_0 \varepsilon_{\mathrm{r}} / t_{\mathrm{ox}}$, where ε_0 represents the vacuum permittivity; ε_{r} and t_{ox} represent the relative permittivity and the thickness of the gate dielectric material (285 nm of SiO_2 in this study), respectively; $\alpha = 7.56 \times 10^{10}$ $\mathrm{cm}^{-2}\mathrm{V}^{-1}$; and n is calculated to be 2.3×10^{12} cm^{-2} for graphene irradiated by a Au-ion beam at 10^{13} cm^{-2}, which agree well with the observed RBS results. Here, it should be noted that the positive and negative n corresponds to the number density of hole and electron carriers. Further, we estimate the lower limit of the carrier density for irradiating graphene by Au or I ion at a dose of 10^{14} cm^{-2}. The carrier density of graphene irradiated by Au- or I-ion beam at a dose of 10^{14} cm^{-2} was estimated to be higher than 4.9×10^{12} cm^{-2} when using the highest gate voltages in the observed data as the lower limit of V_{CNP}.

We assume that the Fermi energy E_{F} of graphene before ion-beam irradiation is at the Dirac point. Thus, the shift of the Fermi energy ΔE_{F} by carrier doping caused by the Au- or I-ion irradiation can be calculated from ΔV_{CNP} [3] using

$$n = \frac{4}{3\pi {\gamma_0}^2 a^2} {E_{\mathrm{F}}}^2, \tag{3.2}$$

where $\gamma_0 \approx 3.15\,\mathrm{eV}$ represents the resonance integral that corresponds to the electronic interaction between the nearest neighbor carbon atoms; $a = 0.246\,\mathrm{nm}$ represents the lattice constant of the honeycomb lattice of graphene; and n represents the carrier density. ΔE_{F} is 0.179 eV for the irradiated graphene at a dose of 10^{13} cm^{-2} for Au ion and it was larger than 0.264 eV at a dose of 10^{14} cm^{-2} for both Au and I ions.

The larger shift of the Fermi energies in graphene irradiated at 10^{14} cm^{-2} is consistent with the larger D' band intensity, which is attributed to the Coulomb scattering of carriers by charged dopants, as shown in Fig. 3.9 (d). For the origin of the observed hole doping by I-ion irradiation, the theoretical study of the graphene-doping mechanism by I atoms was reported previously [92], wherein the band structure of graphene and low concentration (2.00 %) of I atoms adsorbed on graphene was calculated. The Dirac point appeared above the Fermi level by 0.45 eV for I-adsorbed graphene, with a localized band attributed to the 5p states of I below the Fermi level, which indicates an electron transfer from the graphene p orbital to the unoccupied 5p orbital of the I atom, which becomes an anion. This is reasonable considering the stronger electronegativity of the I atom compared to that of carbon.

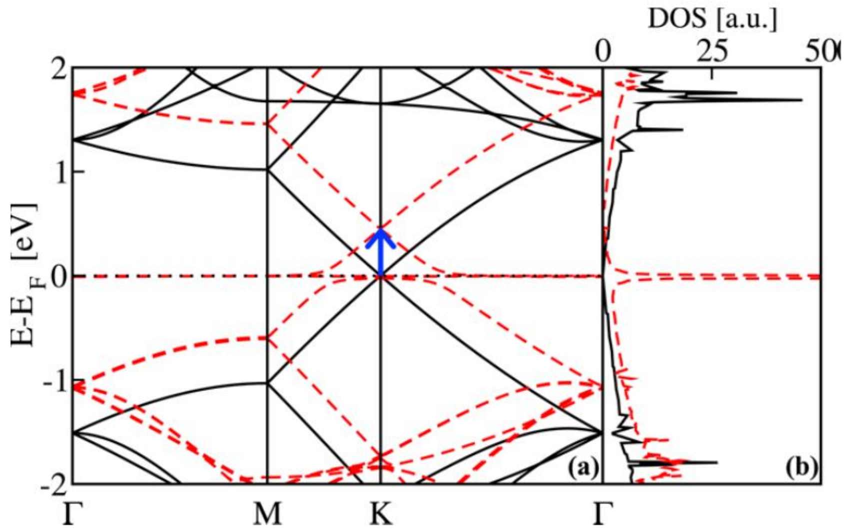

Fig. 3.11 Band structure (a) and total electronic density of states (b) of isolated graphene layer (black line) and with halogen atoms adsorbed on graphene layer (red dashed line) at low iodine concentration (2.00%) [92]. The blue arrow shows the shift of the Dirac point. The Fermi level is at zero energy.

On the other hand, the hole doping observed by Au-ion irradiation is tricky. First, an atomic Au state can be considered as an introduced impurity chemical species, which is similar to the case reported in semiconductors, where irradiated ions are present as interstitial atoms. The unoccupied 6s orbital of the Au atom is located at 11.3 eV far below the work function of graphene 4.6 eV, it has a higher electron affinity than the C atom, and it can accept an electron from graphene. However, electron doping has been reported for Au-deposited graphene in a photoemission study [93], and for graphene deposited with atom or nanoparticle of Au in an electric conductivity measurement [94]. Moreover, the Au-ion species do not exist as atomic cations but as halide anions under typical chemical conditions. Here, we need to pay attention to the presence of a NaCl sacrificial layer upon Au-ion irradiation. High-energy ions interact significantly with atoms inside the target materials and can cause chemical reactions during their penetration through the target. Especially for alkali halide targets such as NaCl, the selective release of halogen atoms such as chlorine on the beam irradiation of charged particles such as electrons has been reported for a long time [95]. Gold halide anions generated by chemical reactions during the Au-ion irradiation of the NaCl sacrificial layer are probable origins of the hole dopant in Au-ion-irradiated graphene samples. In fact, stage-1 $AuCl_3$–graphite intercalation compounds (GICs) are the most heavily hole-doped ones among acceptor-type GICs [96]. The larger contribution of the strain in the Au-ion-irradiated graphene was seen as the larger downshift of the G band and the smaller D' band shown in Fig. 3.9 (a) and (d) compared to that of the I-ion-irradiated graphene. The presence of larger chemical species such as $AuCl_3$ anions as impurities causes more strain effects on the graphene lattice in comparison with atomic anion species such as I anions.

The career mobility of graphene obtained by calculating the carrier mobility from the gradient of the transfer curves (Table 3.4) decreased from 87 cm^2/Vs to 57 cm^2/Vs and 0.11 cm^2/Vs by 10^{13} cm^{-2} and 10^{14} cm^{-2} Au-ion irradiation, respectively. This suggests that the defects and Au ion introduced by irradiation act as new scattering sources.

Table 3.4 Mobility of graphene FET before irradiation (before), after Au-ion irradiation at a dose of 10^{13} cm^{-2} (Au 10^{13}), after Au-ion irradiation at a dose of 10^{14} cm^{-2} (Au 10^{14}), and after I-ion irradiation at a dose of 10^{14} cm^{-2} (I 10^{14})

Dose (cm^{-2})	Before	Au 10^{13}	Au 10^{14}	I 10^{14}
Mobility (cm^2/Vs)	87	57	0.11	0.03

3.3.6 D-band Discussion

Finally, we discuss the D band of ion-beam-irradiated graphene caused by the intervalley scattering of carriers. Fig. 3.12 (e) shows the ratios of the D-band intensity to the G-band intensity (I_D/I_G) for graphene irradiated at doses of 10^{13} Au ion, 10^{14} cm^{-2} Au or I ion where I_D/I_G is calculated as 3.4, 2.9, and 4.5, respectively. The intensity of the D band caused by the elastic scattering of photoexcited carriers in a Raman process does not necessarily correspond to the carrier mobility observed in the electric conductivity, wherein the scattering of the lower-energy carriers is dominated in different manners, which includes significant effects of intra-valley scattering that yields no D band, as we reported in the previous study [61].

Eq. 3.3 shows a model of the I_D/I_G ratio proposed in a previous study, in which only vacancies without charged impurities were introduced into graphene using Ar-ion irradiation with a beam energy of 90 eV [19]. In this model, the modification of the graphene sheet by a single impact of an ion is represented by two length scales, r_A and r_S ($r_A > r_S$), which are the radii of the two circular areas measured from the ion impact point as shown in Fig. 3.12 (f).

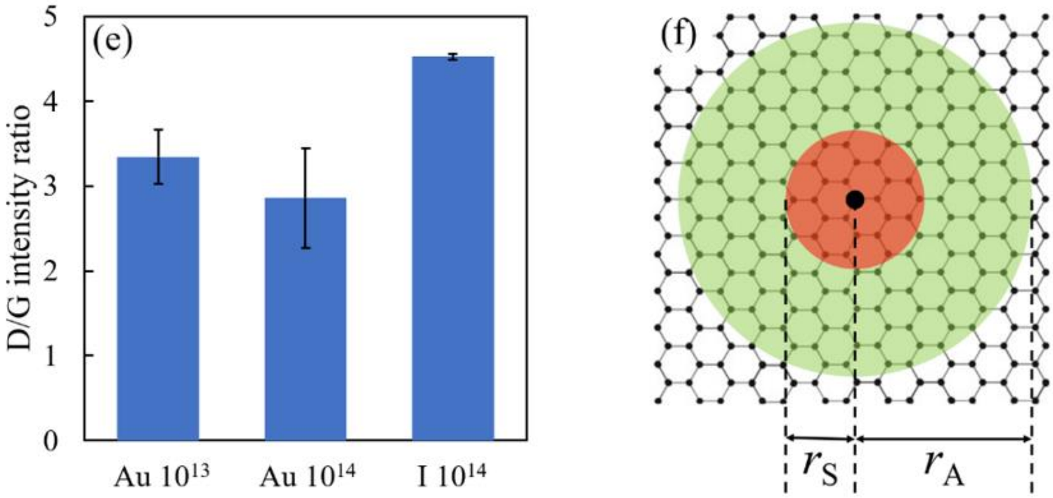

Fig. 3.12 (e) Raman peak fitting parameters of graphene after Au-ion irradiation at a dose of 10^{13} cm^{-2} (Au 10^{13}), after Au-ion irradiation at a dose of 10^{14} cm^{-2} (Au 10^{14}), and after I-ion irradiation at a dose of 10^{14} cm^{-2} (I 10^{14}) for ratio of the D band to the G band intensity. (f) is schematic model of a single impact of an ion on the graphene sheet with two length scales r_A and r_S.

The shorter radius r_S denotes a structurally disordered region (S) near the point of impact, where the graphene honeycomb lattice structure is completely destroyed, and only a weak scattering light contribution appears in the D-band region in the Raman spectrum. In such an atomically disordered sp^2 carbon system, breaking the translational symmetry relaxes the momentum conservation rule in the Raman scattering process, wherein the large phonon density of states at the K point yields weaker components in the

D-band region of the spectrum without a graphene honeycomb structure [97][98]. For an area with distances larger than r_{S} but shorter than r_{A} from the impact point, which is called the activated region (A), the graphene honeycomb lattice remained and exhibited a D-band signal by the double-resonance Raman process caused by the elastic scattering of carriers because of the presence of the defective S region [41].

$$\frac{I_{\mathrm{D}}}{I_{\mathrm{G}}} = C_{\mathrm{A}}\frac{r_{\mathrm{A}}^2-r_{\mathrm{S}}^2}{r_{\mathrm{A}}^2-2r_{\mathrm{S}}^2}\left[\exp\left(-\frac{\pi r_{\mathrm{S}}^2}{L_{\mathrm{D}}^2}\right)-\exp\left(-\frac{\pi(r_{\mathrm{A}}^2-r_{\mathrm{S}}^2)}{L_{\mathrm{D}}^2}\right)\right]+C_{\mathrm{S}}\left[1-\exp\left(-\frac{\pi r_{\mathrm{S}}^2}{L_{\mathrm{D}}^2}\right)\right], \tag{3.3}$$

where C_{A} and C_{S}, represent the probability of causing the D band for one impact point for the double resonance process in the A region and for the weak emission in the destroyed S region, respectively, and L_{D} is the mean distance between the defects. r_{S} is reported to be 1 nm for the surrounding area of one vacancy formed by the ion irradiation process, consistent with STM observation studies [99][19]. C_{S} was estimated to be 0.87 as a typical value for the emission probability of an atomically disordered sp^2 carbon system in the D-band region of the Raman spectra. Further, r_{A} was determined to be 3 nm based on the evaluation of the relaxation length of the excited electrons in the double-resonance Raman process in graphene with a 532 nm excitation at room temperature [19].

In our study, the mean distance of vacancy L_{D} was not directly obtained from the observed results, and it was estimated from the density of ions introduced to graphene, which was obtained by RBS. According to the fundamental theory of vacancy creation during ion-beam irradiation [61][90][91], the stopping power decreases significantly for slow ions before stopping inside the target material. The irradiated ion penetrates deeply without creating vacancies in the region of the deeper-side edge of the ion distribution after its kinetic energy becomes sufficiently low to avoid displacing the atoms of the lattice in the target materials. Therefore, a maximum of the same number of vacancies as the ions introduced into the graphene can be generated. L_{D} are estimated as 7.8, 2.5, and 3.3 nm from the introduced ion density 2.1×10^{12} cm^{-2}, 2.1×10^{13} cm^{-2}, and 1.2×10^{13} cm^{-2} for graphene irradiated at Au-ion doses of 10^{13} cm^{-2}, 10^{14} cm^{-2}, and at an I-ion dose of 10^{14} cm^{-2}, respectively.

C_{A} is calculated as 10.2 by applying the model with the observed $I_{\mathrm{D}}/I_{\mathrm{G}} = 3.4$ for graphene irradiated at an Au-ion dose of 10^{13} cm^{-2}, which is about twice larger than $C_{\mathrm{A}} = 4.2$ reported for the Ar-ion irradiation [19]. Here we should note that a larger vacancy density results in a smaller C_{A} in this model. We now use the upper-limit value of the vacancy density introduced by ion-beam irradiation, and $C_{\mathrm{A}} = 10.2$ represents the minimum limit value estimated by the observed results. Thus, the double-resonance Raman process for the D band is significantly enhanced for Au-ion irradiation which simultaneously introduces both lattice vacancies that yield the D band and charged impurities giving the D' band, compared to that for the Ar-ion-irradiated graphene, where only vacancies are introduced.

We considered the Fermi energy dependence of the carrier scattering probability for vacancies in graphene to understand the higher D-band probability for vacancies introduced by Au-ion irradiation than that for Ar-ion irradiation. We can assume C_{A} to be proportional to the inverse of the carrier relaxation rate τ_{tr}^{-1} determined by the presence of vacancy in graphene considering that the probability of the double resonance Raman process corresponds to the degree of carrier scattering by the presence of vacancy. According to the analytical theory based on a $\boldsymbol{k}\cdot\boldsymbol{p}$ perturbation for carrier scattering by a strong and short-range potential like the vacancy introduced into the graphene honeycomb lattice [100], τ_{tr}^{-1} is proportional to the square of the effective scattering potential V_{S}, and it calculated by

$$C_A \propto \frac{1}{\tau tr} \equiv \frac{2\pi}{\hbar} V_S^2 \frac{1}{2} \sum_{v,v'} \int \frac{\mathrm{d}\boldsymbol{k}'}{(2\pi)^2} \delta\left(\epsilon_{s,\boldsymbol{k}} - \epsilon_{s,\boldsymbol{k}'}\right), \qquad (3.4)$$

where v, v' and $\boldsymbol{k}$, $\boldsymbol{k}'$ denote the K, K' points in the Brillouin zone of graphene and wave vectors of the Bloch states of graphene, respectively; $s = +1$ and -1 for the conduction and valence bands, respectively; and ϵ_{sk} represents the energy eigen value for a Bloch state with $\boldsymbol{k}$ in s.

The numerical calculation results for the Fermi energy dependence of V_{S} are provided in a previous theoretical study [100], which indicate a monotonic increase in V_{S} as the Fermi energy decreases toward the hole-doping side from the Dirac point when the site energy of the vacancy is less than 6 eV, where the site energy is measured from the p orbital energy level of carbon atoms in graphene. Here, it is better to specify the rough estimates of the site energies in practical cases. The site energies measured from the carbon p orbitals are +2.3 eV and −2.5 eV when a site of the honeycomb-lattice graphene is substituted with B and N atoms. In the theoretical study, the site energies of the hydrogenated or fluorinated carbon sites in which the p electron states disappear because of hybridization are supposed to become larger than those of B or N substitution; however, it is certainly not considerably larger.

It is presumed that the site energy of Au substitution would become larger than those of B or N substitution and similar to those in the case of hydrogenation and fluorination. However, the site energy becomes more considerably larger than that of the p orbitals of the carbon atoms when there are vacancies without atoms in the graphene lattice. We assumed the work function of graphene (4.8 eV) as a rough estimate of the site energy for a vacancy in the honeycomb lattice. The effective potential V_S varies by 10 times when the site energy doubles by referring to the numerical calculation results in the theoretical study. According to Eq. 3.4, the probability of the D band by the double resonance Raman process C_A strongly depends on the effective potential (the square of V_S). Therefore, the contribution to the D band by introduced impurities such as Au, N, and B is negligible [61]. The increase in the D band in the case of Au- or I-ion irradiation is attributed to the formation of vacancies occurs simultaneously in graphene.

According to Eq. 3.3, the D band generating probability C_A of Au-ion-irradiated graphene is approximately twice larger than that of Ar-ion-irradiated graphene which introduced only vacancies. This is explained by carrier injection via irradiation with the Au-ion beam. The introduced Au species such as $AuCl_3$ extract electrons from graphene, which causes hole doping and leads to a decrease in the Fermi energy as seen in the Fig. 3.10. Considering the work function of 4.8 eV as a rough estimate of the site energy for a vacancy in the honeycomb lattice, by referring to the numerical calculation results in the theoretical paper, V_S^2 proportional to C_A becomes a little less than the double value when the Fermi energy is downshifted by −0.179 eV from the Dirac point observed in the conductivity for graphene irradiated by Au-ion beam at a dose of 10^{13} cm^{-2}. This explains a twice larger C_A observed in the case of irradiation of Au-ion beam at 10^{13} cm^{-2} as in Fig. 3.13. However, the values of C_A obtained for the Au- or I-ion-irradiated graphene were 3.8 and 5.8, respectively, when applying the model with the observed $I_D/I_G = 2.9$ and 4.5 for graphene irradiated with Au or I ion at 10^{14} cm^{-2}. It showed a considerably less probability for the D band than that of the Au-ion-irradiated graphene at 10^{13} cm^{-2}. The ion-beam-irradiated graphene at 10^{14} cm^{-2} are considerably more downshifted in the Fermi energy as observed in the electronic conductivity, which indicates a considerably higher enhancement in the C_A. One reason for the contradiction is attributed to the extremely high vacancy density for 10^{14} cm^{-2} samples, which leads to the L_D of 2–3 nm, where a major part of the graphene sheet belongs to the so-called structurally disordered regions (S) yielding only a weak D band based on $r_S = 1$ nm. A smaller fraction of the so-called (A) region, which corresponds to the D band in the sample, can cause a larger error in the estimation of C_A.

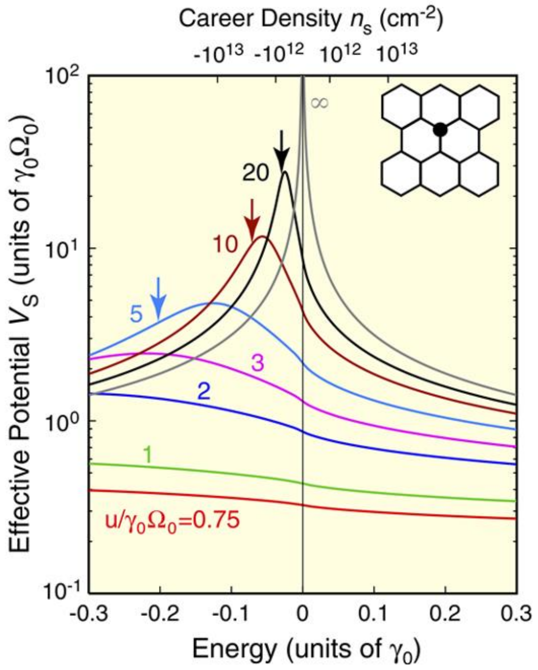

Fig.3.13 Effective potential V_S of defect as a function of energy [100]

3.4 Conclusion

There are several challenges in using the NaCl sacrificial layer for achieving intrinsic defect engineering in 2D materials by ion implantation. A NaCl sacrificial method was performed to investigate the effect of Au- or I-ion species on graphene in the case of high-energy Au- or I-ion irradiation. We showed that using heavier ions for chemical modification by ion-beam irradiation is useful and enables the measurement of the density of ions remaining on the surface of the substrate by RBS because of their higher reflected energy, which can be separated from the substrate material. Both Au- and I-ion irradiation for graphene introduced negatively charged impurities, which provide a D' band through intra-valley scattering in the Raman spectra and hole carriers in the electron transport, wherein Au species exist in a chloride form such as $AuCl_3$ as a product of chemical reactions between Au and Cl atoms during the penetration of Au ion in the NaCl sacrificial layer. The E_F downshift of –0.179 eV in graphene irradiated by the Au-ion beam at 10^{13} cm^{-2} caused by the hole doping of the introduced charged impurities is suggested to promote the double resonance process for the D band in the Raman spectrum by enhancing the effective scattering potential of the introduced vacancies. However, the effects of the E_F downshift on the D band of the Raman spectra become obscure in graphene irradiated at a higher dosage, where the destructive nature of the honeycomb lattice and reduced ability of vacancy introduction at higher dosage conditions could be a probable reason.

This study provides a functional method to perform high-energy beam irradiation on graphene or other 2D materials and gives a valuable reference to the research and application of graphene in the field of electronic devices. However, the detection of residue NaCl is difficult in this study due to the low reflect energy. To avoid this problem and effect of interaction between ions and sacrificial layer, other materials such as CsI should be considered in the future work.

Chapter 4 Fe-ion irradiation on monolayer MoS_2

4.1 Introduction

Spin–valley coupling is one of the most important features in the electronic structure and emission of monolayer MoS_2. In monolayer MoS_2, in addition to the spin-orbit interaction, the parity symmetry is broken; therefore, an inversion center does not exist; moreover, the K valleys of different directions in the 2D hexagonal Brillouin zone are no longer equivalent; therefore, two types of K valleys exist. In fact, the electron spin in the split valence band at the K point is exactly the opposite at the K' point, and the valley and spin degrees of freedom are strongly coupled. Monolayer MoS_2 can be expected to be applied to spin–valley electronics, which utilizes this spin–valley polarized state as an information carrier, which is different from conventional electronics that utilize only the charge degree of freedom of electrons [3]. In spin–valley electronics, only one valley must be selectively excited, which can be achieved using circularly polarized light.

The selective valley polarization in monolayer MoS_2 is affected by strain, magnetic fields, and optical pumping with circularly polarized light [10]. As the orbital angular momentum of the valence and conduction bands differs by +1 or −1, depending on the valley, according to the law of conservation of angular momentum, optical excitation is achieved via right-handed (σ^+) or left-handed (σ^-) circularly polarized light. Only one of the K and K' valleys can be selectively excited [10]. In fact, the polarization degree of the circularly polarized light-resolved PL at 14 K proposed by K. F. Mak is nearly 100%, and research has revealed that valley polarization has a significantly long spin–valley relaxation time (Fig. 4.1) [10].

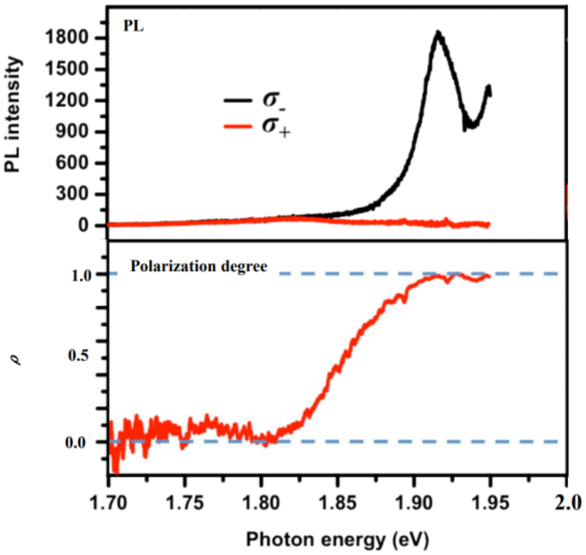

Fig. 4.1 σ+ and σ- resolved PL spectra of 1L-MoS_2 and the corresponding polarization degree ρ [10]

In the previous study, obvious polarization by excitation at A peak could be observed with 1.96 eV (633 nm) excitation; however, off resonance was observed with both A- and B-exciton PL via excitation with 2.33 eV (532 nm). This implies that the selective valley polarization is also strongly affected by the energy of excitation.

4.1.1 Circular polarization

A waveplate is fabricated using a type of crystal that exhibits different light speeds at different directions, with a fast axis in the direction with highest light speed and slow axis in the direction perpendicular to the fast axis with the lowest light speed. When light penetrates a waveplate, its vibration along the fast axis is faster than that in the slow direction. In this case, by adjusting the thickness of the waveplate, it can be adjusted that how much the wave phase in the direction of the slow axis behind the which in the fast axis.

A half-waveplate can rotate the polarization direction by inverting the wave phase in the direction of the slow axis, because of the wave phase in the direction of the slow axis will behind which in the fast axis by half a cycle. In the case of a quarter-waveplate, the wave phase in the direction of the slow axis will behind which in the fast axis by one-quarters of a cycle. After penetrating the quarter-waveplate, the vibrations in the two directions are no longer synchronized, and the synthesized light is rotated around the light direction. By aligning the fast axis by 45° or −45° to the direction of laser polarization, which implies that the components are identical along both the fast and slow axes, the light becomes a circularly polarized light, as shown in Fig. 4.2.

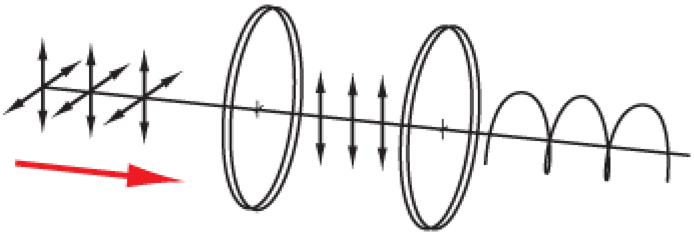

Fig. 4.2 Schematic diagram of polymer circular polarizer [101]

The direction of circularization is dependent on whether the polarization direction of the incident linear polarized light is 45° or −45° toward the fast axis.

4.1.2 Helicity parameter

To quantify the degree of PL polarization, the helicity parameter

$$\rho = \frac{|I_+ - I_-|}{I_+ + I_-} \tag{4.1}$$

is used to evaluate the level of polarization. Here, I_+ and I_- denote the intensity of the circularly polarized PL in σ^+ and σ^- with the same excitation, respectively. Notably, if either intensity is 0, then $\rho = 1$, indicating a fully circular-polarized PL; conversely, if $I_+ = I_-$, then $\rho = 0$, indicating that selective valley polarization does not appears.

4.1.3 Distortion of circular polarization in optical path

Normally, circularly polarized light and its polarization direction can be obtained and detected, respectively, using two pairs of linear polarizers and quarter-waveplates. However, as the presence of any other element inside the optical path can distort the polarization properties of light, another half-waveplate should be added to the path to compensate for the distortion [102].

4.1.4 Objective of chapter 4

As the selective valley polarization in monolayer MoS_2 is affected by the internal magnetic fields, the Fe atom, a magnetic atom, can be used to modify the valley polarization properties of MoS_2 by introducing spin scattering source.

In this study, a circularly polarized PL measurement system was developed by modifying the optical systems of an existing Raman/PL spectrometer unit, on which a hand-made cryogenic stage was also attached to obtain the stable sample temperature necessary for circularly polarized PL measurement, which is not achievable using the existing flow-type cryostat. Raman spectroscopy and circularly polarized PL measurements were performed for 1L-MoS_2 after Fe-ion irradiation, where the NaCl sacrificial layer method developed for Au- or I-ion irradiation was similarly applied to stop ions on 1L-MoS_2 with atomic-scale thickness as described in Chapter 3.

4.2 Experimental

4.2.1 Sample fabrication

Monolayer MoS_2 was prepared by mechanical exfoliation from the surface of bulk crystal MoS_2, then transferred to the surface of a silicon substrate coated with a 285 nm thick SiO_2 layer. The number of layers was determined based on the brightness contrast in the optical image and confirmed via Raman spectroscopy. The typical scale of the monolayer sample was 10–20 μm [7].

Cr/NaCl sacrificial layer was used to decelerate the Fe ion during ion-beam irradiation. It was deposited in vacuum condition with the optimized thickness of 10/250 nm, which was simulated using the SRIM-2013 program. After irradiation, the sacrificial layer was removed using boiling deionized water [51].

4.2.2 Development of the polarization instrument

Generally, a circularly polarized laser can be generated by passing a linearly polarized light through a quarter-waveplate with its fast axis at 45° to the laser polarization axis. However, in a real instrument, other elements in the optical path such as mirror and beam splitter prism will deeply distort the properties of a laser beam. For example, the circular-polarization properties of inserted laser at the sample position changed from circular to elliptical after inserting a camera module with beam splitter prism; moreover, the intensity decreased from approximately 800 to 140 μW (532 nm, 25mW, neutral density filter with 25% average transmission). In fact, even the direction of liner polarization of a laser was rotated by the camera module.

Circularly polarized PL measurements were performed by combining a polarizing element (Thorlabs, Inc.) (Fig. 4.3) [102]. First, the shift in linearly polarized light was adjusted using a linear polarizer and half-waveplate, and then separated into left and right circularly polarized components using a quarter-waveplate, which was then incident on the sample. The PL emitted from the sample was measured by converting each circularly polarized light into mutually orthogonal linearly polarized light using a quarter-waveplate, and passing only one component through the detector using a linear polarizer.

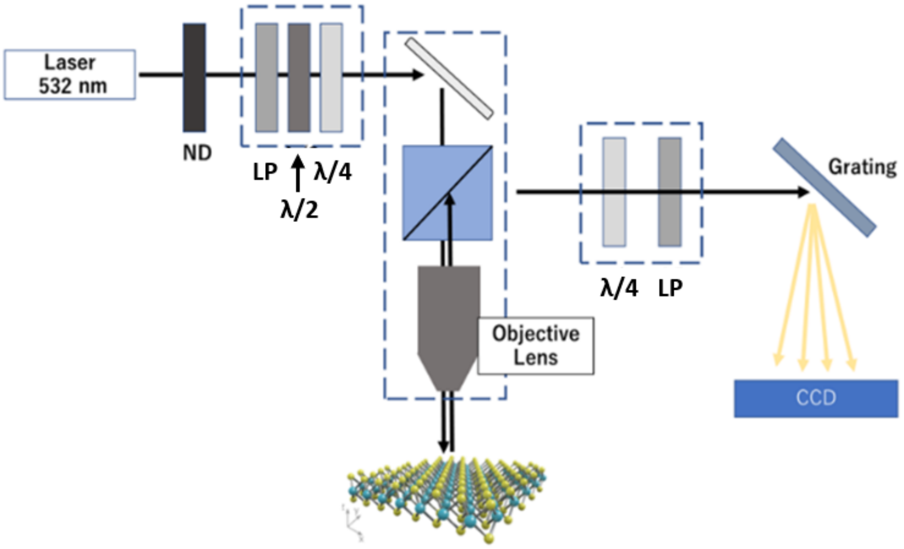

Fig. 4.3 Schematic diagram of the instrument for circular-polarization measurements.

LP: liner polarizer; λ/2: half-waveplate; λ/4: quarter-waveplate

The left and right rotations of circular polarization was confirmed using a combination of linear polarizer and quarter-waveplate. In previous research, σ^+ and σ^- was assumed to be incident when the quarter-waveplate was aligned at 268° and 358°, respectively. However, that is regardless of the distortion inside the optical path. In this experiment, we detected the property of laser at sample stage by using a liner polarizer and power meter. In this case, the same laser intensity at every horizontal direction meaning high circular polarization.

We found that the best angle set of LP, λ/2, λ/4 at incident side is 330°, 34°, 251° for σ^+, and 330°, 80°, 252° for σ^-. Similarly, we determined the angle set of λ/4, LP at scattering side is 47°, 88° for σ^+, and 47°, 359° for σ^-. Moreover, the data obtained when σ^+ is incident and σ^+ is passed through the detector were denoted as σ^+/σ^+. Similarly, the other three types of data were measured as σ^+/σ^-, σ^-/σ^-, σ^-/σ^+.

The special designed cryostat system for low-temperature measurements is shown in Fig. 4.4. The sample was mounted on a 14 mm thick copper plate and placed in an insulated container filled with liquid nitrogen. To measure the temperature of the substrate surface, a leaf spring was used on the surface and a thermocouple was brought into direct contact with the substrate. To prevent outside air from entering, the container was covered with a heat insulating sheet, and a hole was created in the sheet at the beam spot position to perform measurements.

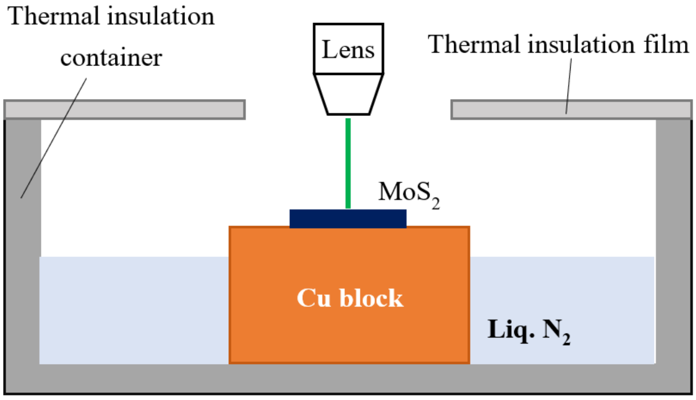

Fig. 4.4 Schematic diagram of the cryostat system for low-temperature circular-polarization measurements

4.2.3 Fe-ion irradiation

A tandem accelerator (Research Center of Ion Beam Technology, Hosei University) was used for irradiating Fe ions at an acceleration voltage of 200 keV, which is the lowest energy condition for the practical usage of the beam in this system, at doses of 10^{12}–10^{15} cm^{-2} [51].

4.2.4 Sample characterization

Raman spectroscopy and PL analyses were performed using a microscopic spectrometer (LabRAM HR Evolution, HORIBA) at an excitation laser wavelength of 532 nm. In the low-temperature PL measurement, the sample was measured at 77 K using the cryostat system with liquid N_2 [7].

4.3 Results and discussion

4.3.1 Evaluation of the sacrificial layer

The optimal value of the sacrificial layer thickness was estimated via Monte Carlo simulation of the range of Fe ion in the material using SRIM-2013. The Cr/NaCl sacrificial layer with thickness of 10/250 nm is the optimum value obtained using classical Monte Carlo simulation. The Fe ions that were irradiated with an accelerating voltage of 200 keV lost energy by colliding with the sacrificial layer, and most of it stopped within the sacrificial layer. The remaining ions stopped near the SiO_2 surface, while minimizing the generation of vacancies in the SiO_2 layer. From this, we predicted that the film thickness that was set could maintain the maximum Fe-ion distribution while suppressing damage caused by vacancy formation at the MoS_2 position.

Fig. 4.5 shows the Raman spectra before and after removing the Cr/NaCl layer. The characteristic peaks of the crystalline lattice of MoS_2, which are E' (~397.1 cm^{-1}, in-plane vibrational mode of S atoms) and A'_1 (~408.5 cm^{-1}, out-of-plane vibrational mode of S atoms), can be observed. A peak corresponding to the 2LA band related to a double-resonance Raman process with inter-valley scattering of two LA phonons can be observed at approximately 450 cm^{-1}. Moreover, a small peak near 305 cm^{-1} originates from the second-order transverse acoustic mode of the Si substrate [103]. No change is observed in the E' and A'_1 peaks before and after removing the Cr/NaCl layer, and no LA peak appeared around 227 cm^{-1}. The LA peak is related to the LA mode at the edge of the Brillouin zone, which is forbidden in an ideal MoS_2, but occurs owing to the inter-valley elastic scattering of carriers caused by the presence of defects [61]. The small hump that appears around 227 cm^{-1} in Fig. 4.5 can be seen even before the sacrificial layer was deposited, but this is thought to be due to defects being introduced into the MoS_2 lattice during the peeling process. After removing the Cr/NaCl layer, no changes in the shapes of E', A'_1, and 2LA are observed, and no new peaks, including LA, are exhibited. This indicates that the formation of the Cr/NaCl sacrificial layer has no effect on the structure of MoS_2.

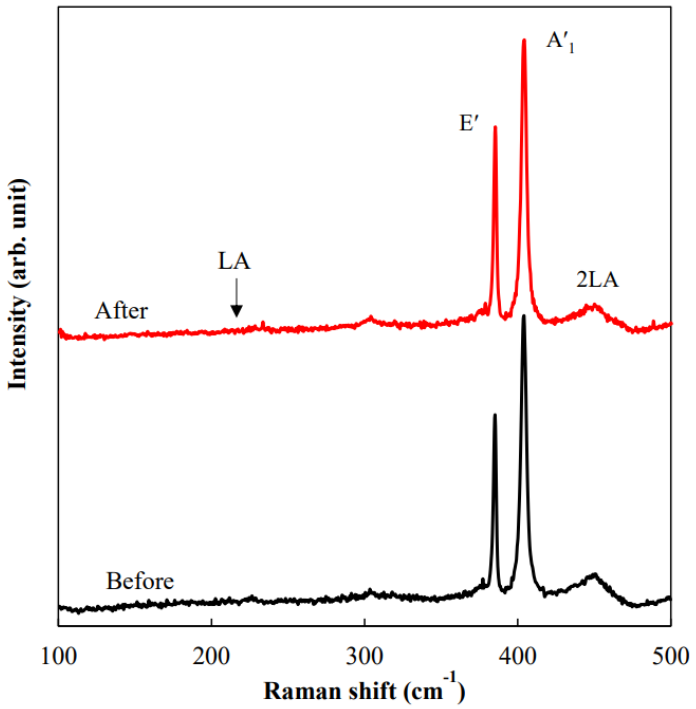

Fig. 4.5 Raman spectra of 1L-MoS$_2$ before deposition and after removal of Cr/NaCl sacrificial layer

Fig. 4.6 shows the PL spectra before and after removing the Cr/NaCl layer. Peaks corresponding to the A (1.84–1.88 eV) and B (2.02 eV) peaks, which are characteristic peaks of the PL of MoS$_2$, can be observed. Moreover, the A peak shifts to the higher-energy side by approximately 0.01 eV. This is thought to be caused by a significantly small amount of hole doping caused by physically adsorbed water during water immersion during the Cr/NaCl layer removal process [104].

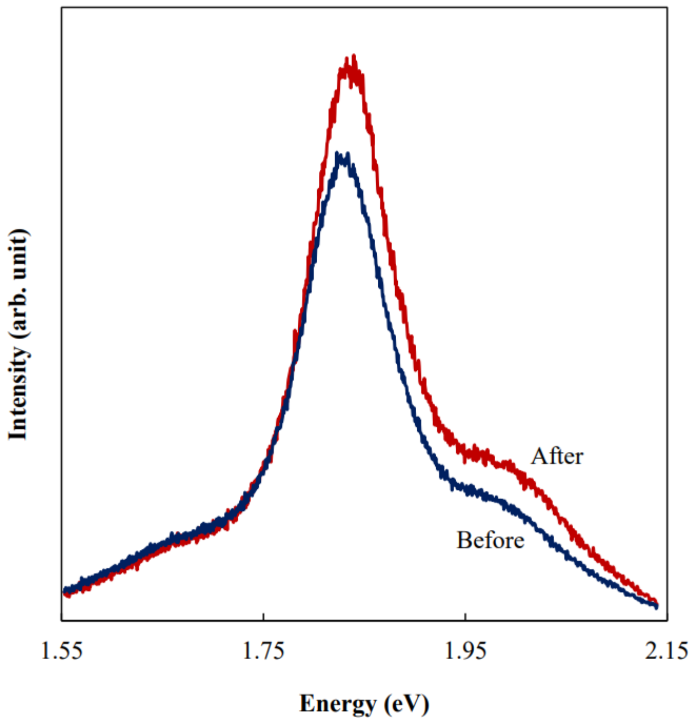

Fig. 4.6 PL spectra of 1L-MoS_2 before deposition and after removal of Cr/NaCl

4.3.2 Raman spectroscopy

Fig. 4.7 shows the Raman spectra of MoS_2 before and after Fe-ion irradiation. No change in the shape of E' and A'_1 is observed in the MoS_2 Raman spectrum up to approximately 10^{13} cm^{-2} of irradiation; however, for greater irradiation doses, the intensity of E' and A'_1 decreased rapidly, and at 10^{15} cm^{-2}, 2LA mode is observed. The three peaks including this peak almost disappears. Furthermore, after Fe-ion irradiation, the line widths of the E' and A'_1 peaks increases as the irradiation dose increases.

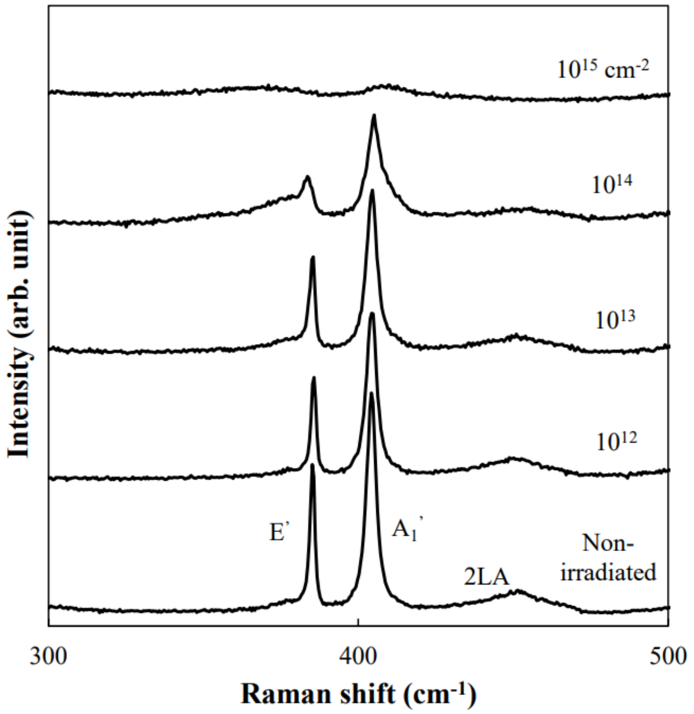

Fig. 4.7 Raman spectra of 1L-MoS_2 before and after irradiation by Fe ion at doses of 10^{12}–10^{15} cm^{-2}

Here, we discuss the dose dependence in the structure of MoS_2 using Raman spectra. Fig. 4.8 shows the changes in the intensity of the E', A'_1, and 2LA peaks with respect to the irradiation dose. In the MoS_2 Raman spectra up to approximately 10^{13} cm^{-2} of irradiation, only a marginal decrease in the intensity of E' and A'_1 is observed, which can be attributed to the use of the sacrificial layer, which resulted in the implantation of ions while maintaining the basic structure of MoS_2. Furthermore, the defect species introduced into MoS_2 are primarily thought to be S site defects, Mo site defects, and MoS_6 cluster defects [6]; however, the rapid decrease in E' and A'_1 at the dose of 10^{14} cm^{-2} can be attributed to the increase in Mo defects at this dosage; finally, at the maximum irradiation dose, structural defects larger than the MoS_6 cluster defects occur, resulting in a large decrease in the amount of MoS_2 itself.

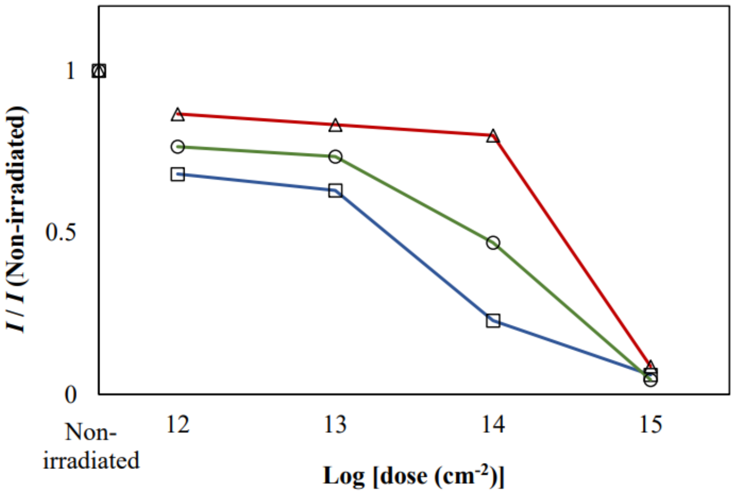

Fig. 4.8 Changes in E' (square), A'_1 (circle), and D peak (triangle) intensities before and after Fe-ion irradiation

4.3.3 PL

Fig. 4.9 shows the PL spectra of MoS_2 at different Fe-ion irradiation doses. The intensity decreases rapidly as the Fe-ion irradiation dose increases. The peak shape changes significantly even at 10^{13} cm^{-2}, where there was almost no change in the Raman spectrum, and almost no emission is observed when Fe ions are irradiated at 10^{15} cm^{-2}. The magnified PL spectra of MoS_2 before and after Fe-ion irradiation (10^{12}, 10^{13} cm^{-2}) are shown in Figs. 4.10 and 4.11. For both ion-beam doses, peaks corresponding to the A (1.84–1.88 eV) and B (2.02 eV) peaks, which are characteristic peaks of the PL of MoS_2, appear as shown by the fitting curves in Fig. 4.10. As the irradiation dose increases, the intensity of the A peak decreases, and a tail of the peak appears from 1.8 eV to the lower-energy side. Moreover, the A peak shifts to a lower energy at both 10^{12} and 10^{13} cm^{-2}, and the amount of shift increases as the irradiation dose increases. Furthermore, an increase in the intensity of the B peak is observed after Fe-ion irradiation.

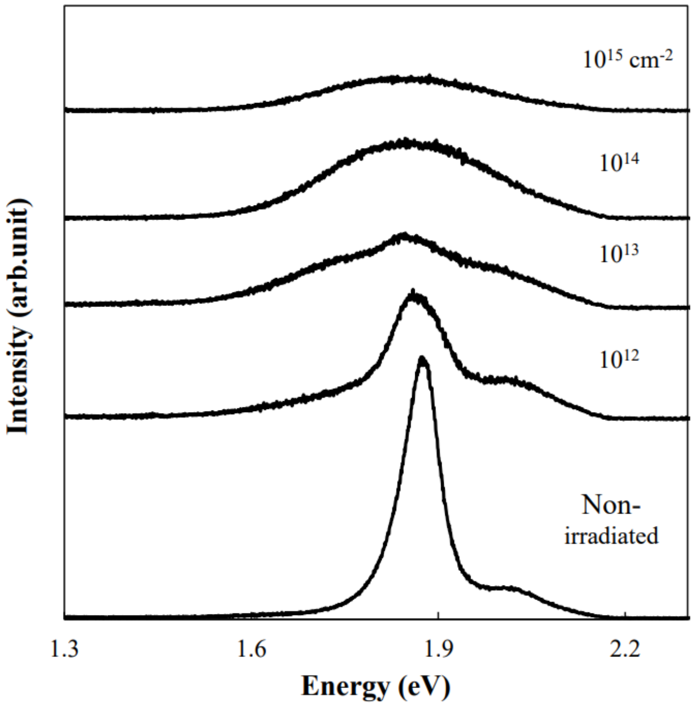

Fig. 4.9 PL spectra of 1L-MoS_2 before and after irradiation of Fe ion at doses of 10^{12}–10^{15} cm^{-2}

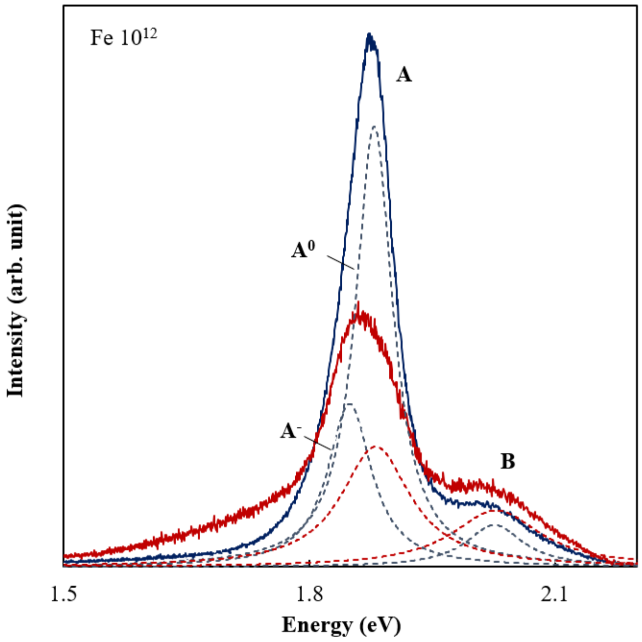

Fig. 4.10 PL spectra of 1L-MoS_2 before and after Fe-ion irradiation at a dose of 10^{12} cm^{-2}

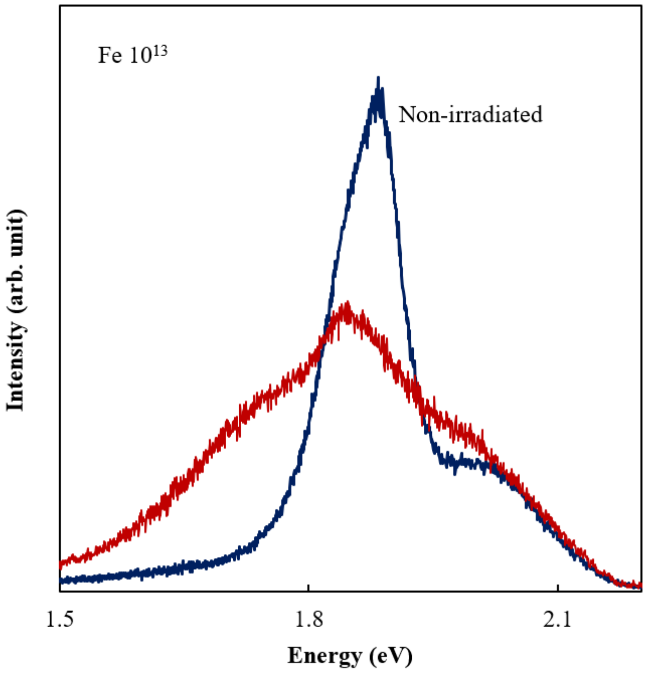

Fig. 4.11 PL spectra of 1L-MoS_2 before and after Fe-ion irradiation at a dose of 10^{13} cm^{-2}

The decrease in the A-peak intensity and appearance of a tail on the low-energy side of the peak caused by Fe-ion irradiation are common results with Ar-ion irradiation, which is described in Chapter 2. This occurs because, when defects are introduced into MoS_2, new defect levels with various energy eigenvalues are generated within the gap, and the radiative transition of thermally relaxed electrons causes a wide energy range with no clear peak [7]. This is thought to be due to the fact that luminescence was observed across the range. Furthermore, the lower-energy shift of the A peak observed with Fe-ion irradiation was not observed with Ar-ion irradiation, as described in Chapter 2. The energy shift of the A peak is caused by changes in the emission intensities of the neutral exciton A_0 and charged exciton A^- (trion) [105]. Fig. 4.12 shows that the emission intensity ratio $A^-/(A_0 + A^-)$ before and after ion irradiation does not change with Ar ion, whereas the ratio increases up to 0.57 after Fe-ion irradiation at 10^{12} cm^{-2}, in contrast to 0.31 in the non-irradiation case, indicating that the luminescence component derived from trions increased. This suggests that Ar-ion does not react with MoS_2 and cannot remain in the sample after irradiation, and desorbs and generates only vacancies, whereas Fe ion is introduced into the MoS_2 surface after irradiation, causing electron doping.

Furthermore, as the amount of shift increases further when the irradiation dose increases to 10^{13} cm^{-2}, it is clear that the injected Fe ion causes charge transfer.

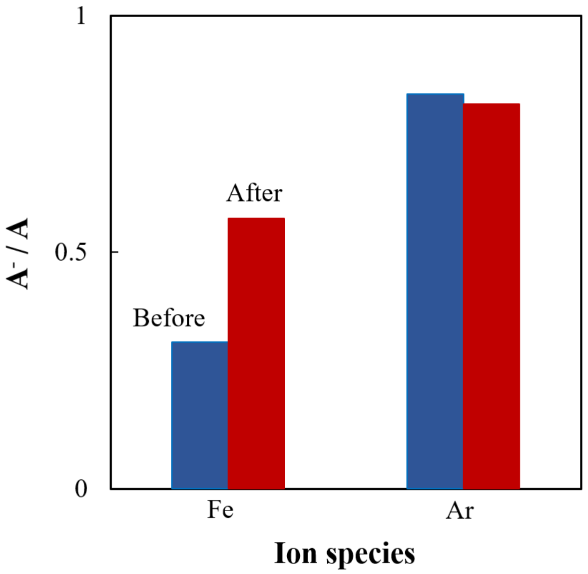

Fig. 4.12 Change of A^-/A ratio in A peak before and after irradiation of Fe and Ar ions

The intensity ratio ΔI_B of the B peak before and after Fe-ion irradiation was 1.35, indicating an increase in B-peak intensity (Table 4.1). Conversely, in the results shown in Chapter 2, when chemically inert Ar ion was irradiated, almost no increase in the B peak was observed ($\Delta I_B = 1.16$). This suggests that the introduced Fe ion caused spin scattering in MoS_2. This can be explained by the following process: the implanted Fe ions exist as ferromagnetic species, and the presence of the ions causes the local electric field and strain applied to MoS_2 to break the symmetry of the K and K' points. In this case, the spin direction of the excited electrons is reversed and polarized owing to spin scattering by Fe ions; consequently, instead of falling into the valence band, where the excited electrons were originally supposed to fall, these excited electrons fall into the lower-energy band split by spin-orbit interaction.

Table 4.1 Changes in the intensity of B peak ΔI_B before and after irradiation of Fe and Ar ions

Ion	ΔI_B
Ar	1.16
Fe	1.35

4.3.4 Evaluation by circularly polarized PL

Single-layer MoS_2 has direct gaps at the K and K' points on the reciprocal lattice space. By making the incident light circularly polarized in the clockwise (σ^+) and counterclockwise (σ^-) directions, the K and K' valleys can be selectively excited. Ideally the degree of polarization ρ that is estimated from the circularly polarized light emission is 1 [10]. Circularly polarized PL spectra of MoS_2 before and after Fe-ion irradiation (10^{12}, 10^{13} cm^{-2}) are shown in Figs. 4.13–4.18. The polarization degree ρ is calculated using the PL intensity I_+ (I_-) of right-handed (left-handed) circularly polarized light using Eq. 4.1. The moving average of ρ is plotted in the graph. For all samples, the degree of polarization increased by lowering the temperature from room temperature to a lower temperature. Furthermore, focusing on the degree of polarization at low temperatures (77 K), the polarization of the A peak was almost relaxed after irradiation with Fe ion of 10^{12} cm^{-2}. Conversely, the polarization of the B peak remained unchanged. Furthermore, when focusing on the A_0 and A^- peaks that make up the A peak, the polarization of the A^- peak is almost relaxed, whereas the A_0 peak maintains a slight polarization. This suggests that trions have a higher scattering probability than neutral excitons. Moreover, polarization of the peak around 1.7 eV for the defect states (D peak), which was not seen in previous studies, was observed.

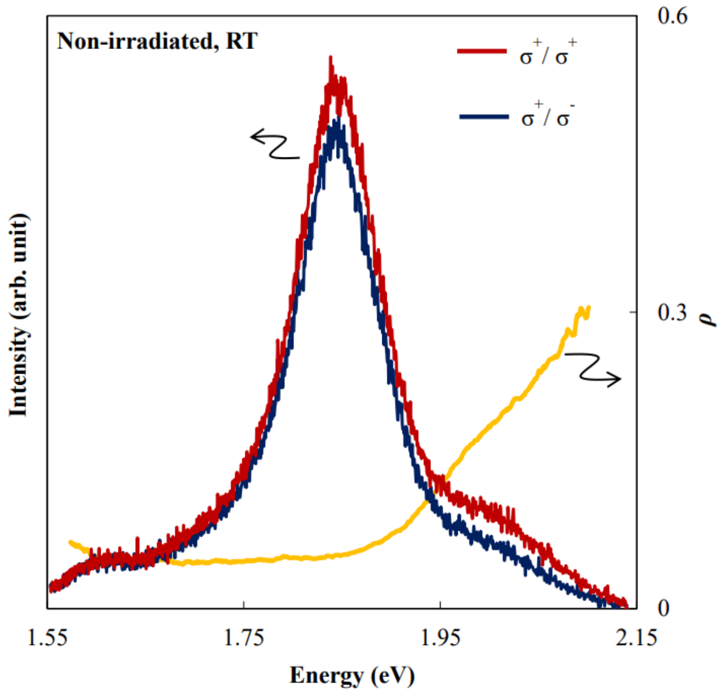

Fig. 4.13 PL spectra of non-irradiated 1L-MoS$_2$ using circularly polarized light excitation at room temperature (RT)

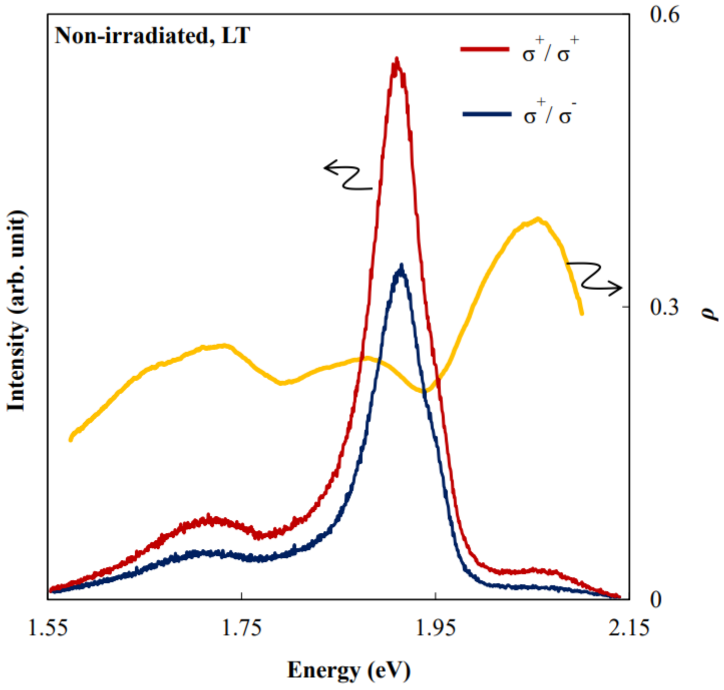

Fig. 4.14 PL spectra of non-irradiated 1L-MoS$_2$ using circularly polarized light excitation at 77 K (LT)

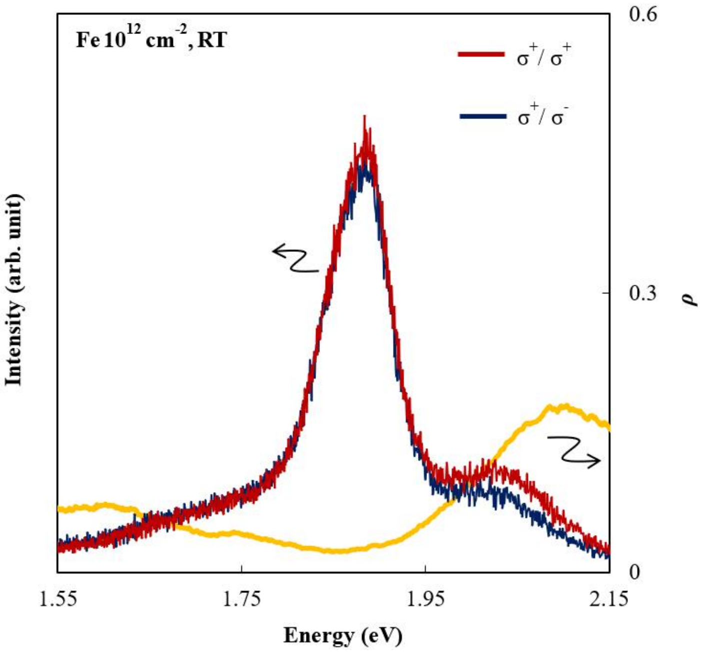

Fig. 4.15 PL spectra of 1L-MoS2 before and after Fe-ion irradiation (10^{12} cm^{-2}) using circularly polarized light excitation at RT

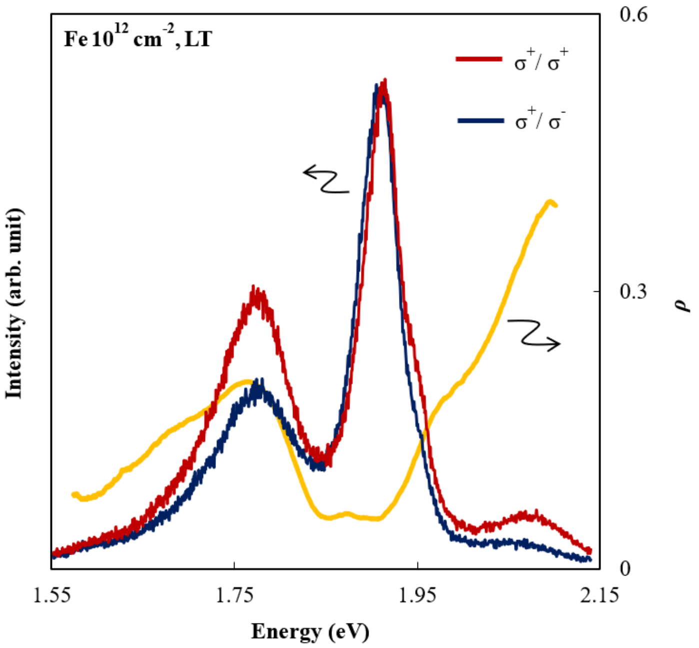

Fig. 4.16 PL spectra of 1L-MoS2 before and after Fe-ion irradiation (10^{12} cm^{-2}) using circularly polarized light excitation at 77 K

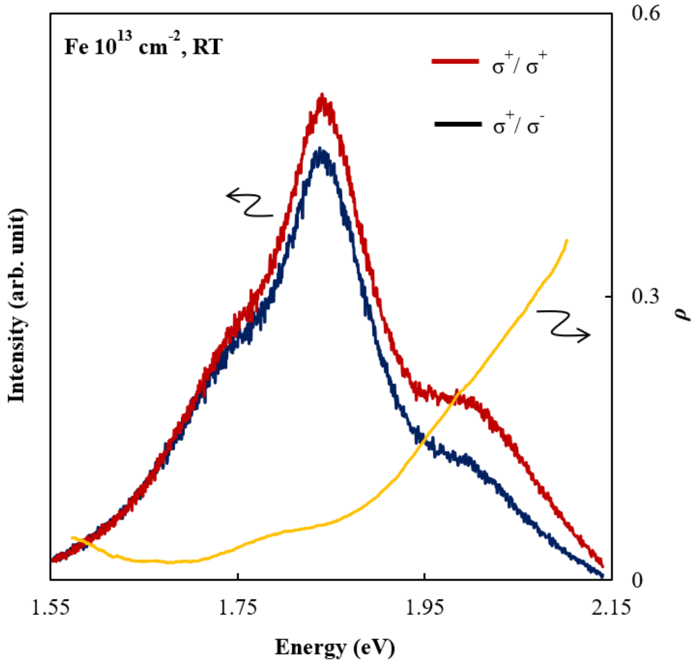

Fig. 4.17 PL spectra of 1L-MoS2 before and after Fe-ion irradiation (10^{13} cm^{-2}) using circularly polarized light excitation at RT

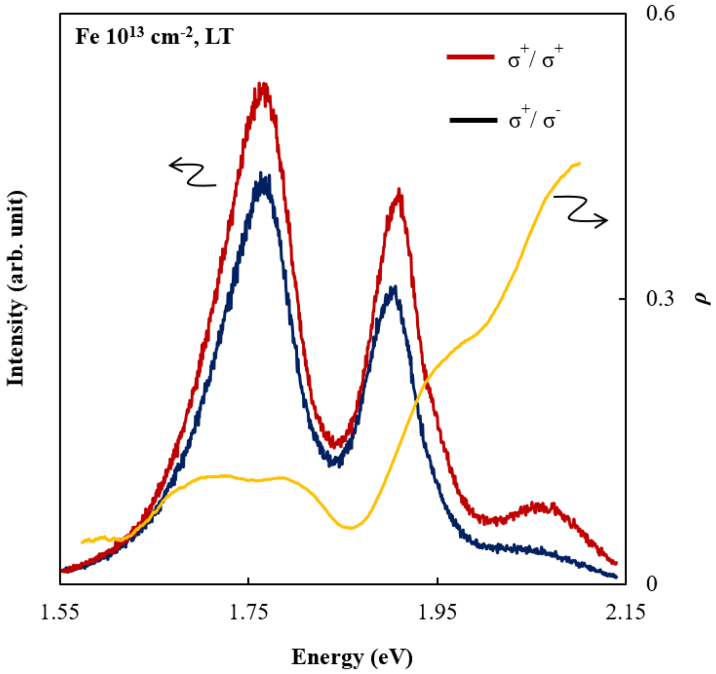

Fig. 4.18 PL spectra of 1L-MoS2 before and after Fe-ion irradiation (10^{13} cm^{-2}) using circularly polarized light excitation at 77 K

Comparisons of the degree of polarization of circularly polarized PL spectra before and after irradiation (10^{12} and 10^{13} cm^{-2}) are shown in Figs. 4.19–4.21. Table 4.2 lists the degree of polarization under each condition of temperature and irradiation amount. In low-temperature measurements, the degree of polarization is improved as compared to that at room temperature, which indicates the existence of valley relaxation caused by phonon scattering. Furthermore, while the A peak was valley relaxed by Fe-ion irradiation, the polarization of the B peak was not relaxed even when the irradiation dose increased. This shows that inter-valley scattering is likely to occur for A excitons, whereas scattering due to introduced defects is less likely to occur for B excitons originating from occupied levels. Moreover, a large degree of polarization was also observed in the D peak, which is originally in a localized state and is expected to have no dependence on the circular polarization of the excitation light; however, this may be because of the overlap between high-concentration impurity levels or hybridization with the bulk state. This suggests the possibility of the existence of a defect-related level.

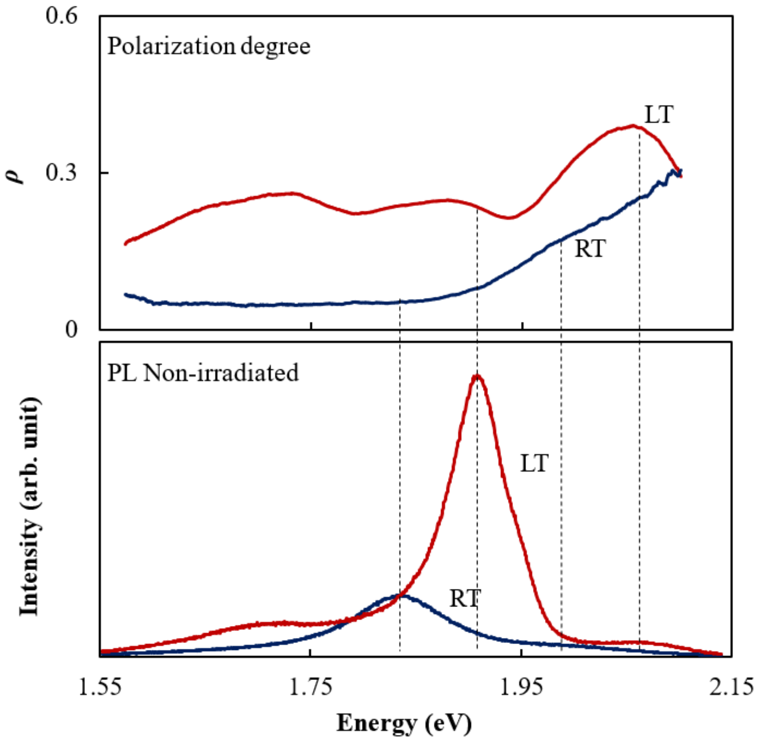

Fig. 4.19 Comparison of polarization degree at RT and 77K (LT) for non-irradiated 1L-MoS_2

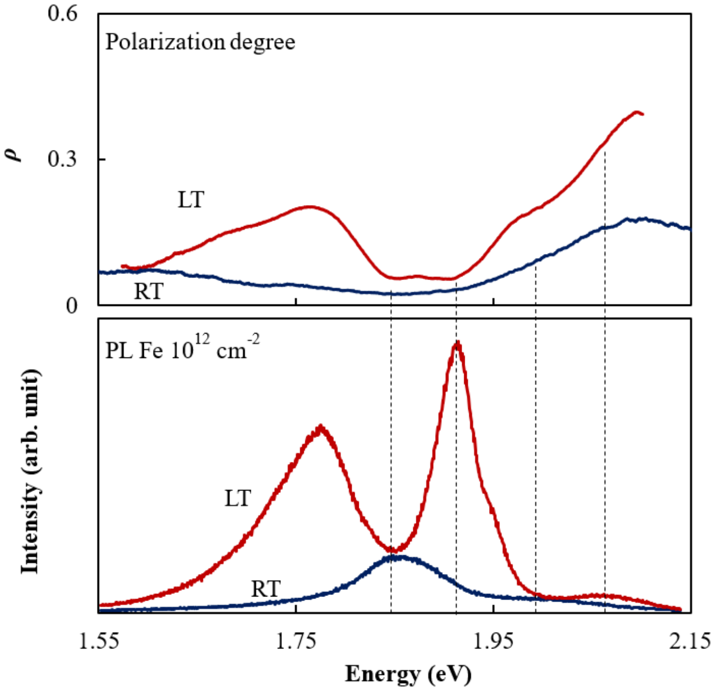

Fig. 4.20 Comparison of polarization degree at RT and LT for 1L-MoS_2 after Fe-ion irradiation at a dose of 10^{12} cm^{-2}

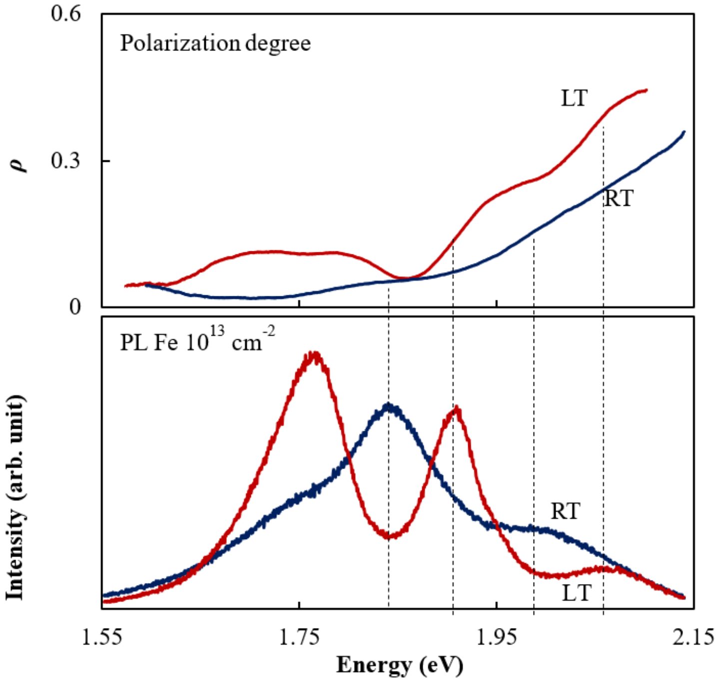

Fig. 4.21 Comparison of polarization degree at RT and LT for 1L-MoS_2 after Fe-ion irradiation at a dose of 10^{13} cm^{-2}

Table 4.2 polarization degree at room and low temperatures in MoS_2 before and after Fe-ion irradiation

		RT				LT				
		A	A^-	A^0	B	A	A^-	A^0	B	D
Before	Position (eV)	1.84	1.83	1.86	1.99	1.91	1.91	1.94	2.07	1.72
	ρ	0.054	0.051	0.055	0.018	0.234	0.234	0.215	0.339	0.258
Fe-10^{12}	Position (eV)	1.86	1.85	1.88	2.03	1.91	1.91	1.95	2.07	1.78
	ρ	0.023	0.023	0.026	0.125	0.058	0.058	0.120	0.210	0.197
Fe-10^{13}	Position (eV)	1.86	-	-	2.07	1.91	1.91	1.95	2.07	1.77
	ρ	0.056	-	-	0.256	0.139	0.139	0.226	0.406	0.110

4.4 Conclusion

Due to selective valley polarization as an information carrier, 1L-MoS_2 is expected to be applied to spintronics. However, its mechanism is still unclear and needs to be investigated. In this study, Fe-ion irradiation was performed as a magnetic impurity, causing spin scattering on 1L-MoS_2 using a NaCl sacrificial layer. From Raman spectroscopy measurements, it can be estimated that the surface of MoS_2 was modified with Fe ions while maintaining its basic structure at low irradiation dose conditions. The increase in trion-derived emission components in the PL-A spectrum revealed that Fe ion introduced onto the MoS_2 surface causes electron doping. In addition, a decrease in the helicity of circular polarization ρ of the A peak was observed by circularly polarized PL measurements, suggesting that Fe-ion irradiation induced spin scattering in 1L-MoS_2 and promoted the relaxation of valley polarization. Furthermore, the helicity increased at a low temperature of 77K. The circularly polarized PL measurements show that although spin scattering is introduced by Fe-ion irradiation, valley relaxation is still derived from lattice vibration.

This study investigates the mechanism of introduced Fe species on 1L-MoS_2 and its effect on selective valley polarization of photoluminescence, giving a valuable reference to the electron transport measurements with magnetic field application are expected to evaluate the effects on spin-orbit effects, which will lead to the development of next-generation spintronics materials by heavy-ion beam irradiation of 2D materials.

Chapter 5 Hydrogen adsorption and Ar-ion irradiation for 1T-phase TaS_2

5.1 Introduction

Finally, we focus on another 2D material, that is, thin-layer TaS_2, which is type of TMD with a 2D structure that is similar to that of MoS_2. TaS_2 has a metallic property when compared to those of graphene and MoS_2, which exhibit semiconductor properties. It has a CDW phase transition that must be investigated.

5.1.1 TaS_2

TaS_2 in the 1T-polytype structural phase is a type of metallic 2D TMD. 1T-phase TaS_2 (1T-TaS_2) at ambient pressure exhibits a metallic phase at high temperatures (>550 K), an ICCDW phase below 550 K, a NCCDW phase below 350 K, and a CCDW phase including a Mott phase below ~180 K [106][107]. The layers are combined by van der Waals-like force and can be exfoliated into few-layers.

Several research groups have confirmed changes in the phase diagram of 1T-TaS_2 resulting from exfoliation. TaS_2 has multiple CDWs that vary depending on temperature, and unprecedented modulation of optical properties is expected because of the generation of structural defects through annealing and adsorption of gas molecules [11]. TaS_2 can be used for devices that require significantly efficient and fast switching at low temperatures [108] and in CDW oscillator and for thermally driven GHz modulation of the CDW state at room temperature [109][110].

5.1.2 Hydrogen adsorption in 2D materials

Because 2D materials have a structure in which all atoms are exposed on the surface, a tiny amount of molecular adsorption or impurity attachment can significantly change the electronic state of the material, and attempts have been made to add new functionality through host-guest interactions using 2D materials as hosts. It should be noted here that the influence of the electrode surface on the adsorption properties must be considered when measuring electrical conductivity. However, the influence has been reported to be small [111]. In an attempt to add new functionality to graphene as a two-dimensional material, the induction of hole doping by the adsorption of oxygen molecules on the graphene surface has been reported [38].

On the other hand, as for the adsorption of molecular hydrogen onto graphene, which is expected to be applied to hydrogen storage materials, it has been reported that electron doping into graphene occurs when hydrogen pressure is increased in a vacuum chamber [112]. However, only slight dissociative adsorption of molecular hydrogen on graphene has been reported.

5.1.3 Defects as adsorption sites in 2D materials

As we have already mentioned, introducing defects is one of the important strategies to modulate the physical properties of 2D materials. In particular, both theoretical and experimental studies have suggested that introducing defects into 2D materials increases the number of structures with broken translational symmetry, which leads to more pronounced changes in electronic states due to the adsorption of tiny amounts of molecules or impurities on the surface [113][114]. Namely, introducing defects into graphene is an effective method to increase the number of adsorption sites for foreign molecules without causing graphene structure destruction by controlling the defect density. A theory based on DFT calculations of molecular hydrogen adsorption on graphene before and after the introduction of defects has been reported [114]. Fig. 5.1 shows a molecular hydrogen adsorption calculation on graphene before introducing defects. The atomic structures of the calculated model are shown in the inserts. The energy of the IS is taken to be zero. The units of E_{bar} and E_{r} are eV, where E_{bar} is the energy barrier, and E_{r} is the reaction energy. The grey, black, and white atoms are saturated C, unsaturated C, and H, respectively [114].

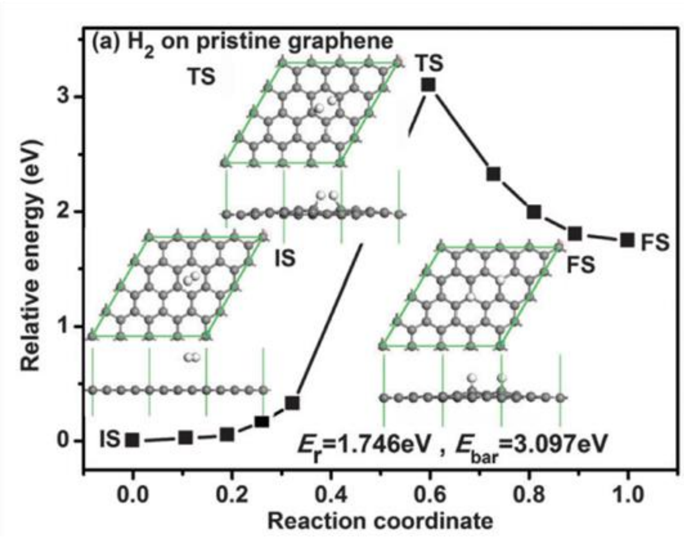

Fig. 5.1 The reaction pathway of H_2 molecule dissociative adsorption on pristine graphene [114]

Initially introduced hydrogen molecules are adsorbed on the hollow sites of graphene. Assuming that the hydrogen molecule then undergoes dissociative adsorption, the energy barrier for adsorption is as high as 3.097 eV, so dissociative adsorption is not expected to occur at room temperature. On the other hand, the calculation of molecular hydrogen adsorption on graphene with monatomic vacancies is shown in Fig. 5.2. The model structures are shown in the inserts. The energy of the IS is taken to be zero. The units of E_{bar} and E_r are eV, where E_{bar} is the energy barrier, and E_r is the reaction energy. The grey, black, and white atoms are saturated C, unsaturated C, and H, respectively [114].

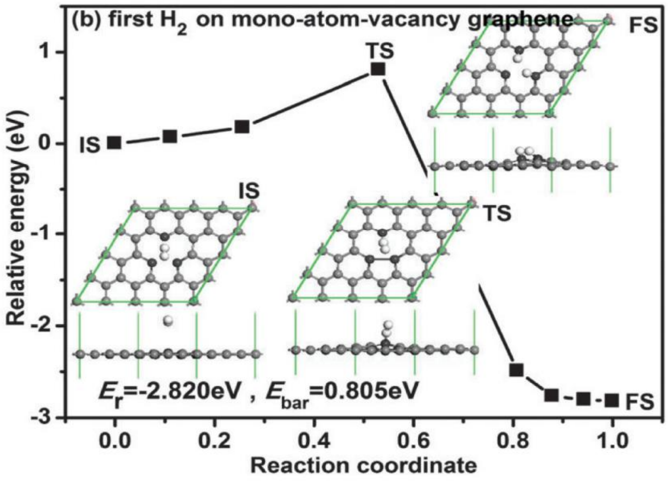

Fig. 5.2 The reaction pathway of H_2 molecule dissociative adsorption on graphene with a mono-atom-vacancy for the first H_2 molecule [114]

In this case, the barrier to dissociative adsorption of molecular hydrogen is 0.805 eV, which is smaller than the critical barrier of 0.91 eV. Since dissociative adsorption proceeds even at room temperature, the introduction of defects into a two-dimensional material is a useful technique for hydrogen storage material applications in that it provides additional hydrogen adsorption sites. However, it has been reported that only a small amount of molecular hydrogen is dissociatively adsorbed on graphene [112]. Therefore, it is expected that introducing defects in metallic 2D materials such as TaS_2, which is expected to react with a more significant amount of hydrogen, will lead to the development of materials that can absorb a larger amount of hydrogen.

5.1.4 Objective of chapter 5

Thin-layer TaS_2 is a promising 2D material in the field of material science and electronic devices but has yet to be well investigated yet compared with bulk TaS_2. In this study, we evaluated the structure and electronic state of TaS_2 on SiO_2 substrates by Raman spectroscopy to elucidate the layer number dependence for a fundamental understanding of the Raman spectrum of exfoliated thin-layer TaS_2 at first. The layer number dependence of Raman spectroscopy is investigated for TaS_2 as a layered material. Then, the hydrogen adsorption effects on the structure of TaS_2 were measured as a further interest. Also, The TaS_2 was irradiated by an Ar-ion beam to investigate the effect of ion-beam irradiation.

5.2 Experimental

5.2.1 Sample fabrication

An SiO_2 (285 nm) substrate was ultrasonically cleaned with acetone and ultrapure water for 5 min at high power ultrasonication. Thin-layers of TaS_2 were exfoliated using mechanical exfoliation method and transferred onto the cleaned SiO_2 substrate, and then ultrasonically cleaned for 1 min at lowest ultrasonication power using an acetone-isopropanol mixture followed by ultrapure water. The number of layers in the exfoliated sample was evaluated based on the contrast difference between the substrate and the sample via OM, and the results confirmed that the sample was a thin-layer.

5.2.2 Layer number evaluation

Using an optical microscope, the brightness contrast difference between the substrate and sample in the red (R) and green (G) wavelength regions was compared in 8-bit (0-255) tones using NIS-Elements software, and the number of layers in the exfoliated sample was evaluated. The specific number of layers of TaS_2 was evaluated based on the contrast difference from a previous study (Fig. 5.3) [115].

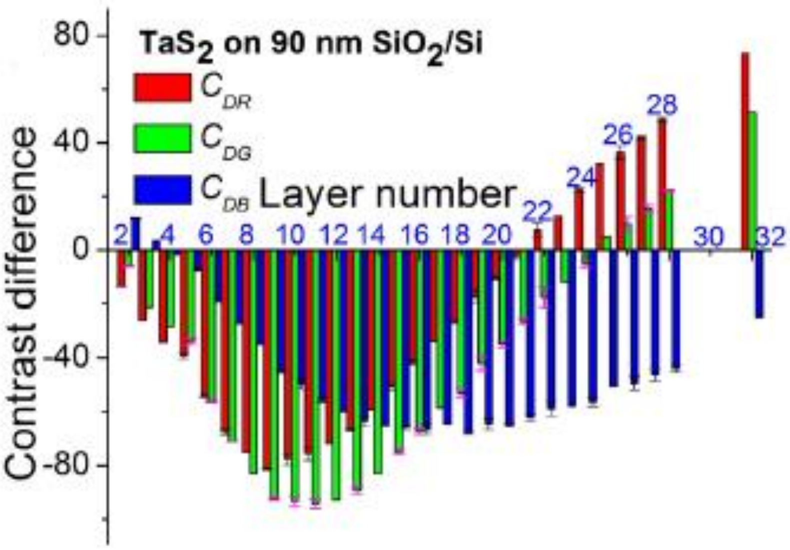

Fig. 5.3 Optical identification of thin-layer TaS_2 [115]

5.2.3 Ar-ion irradiation

Ar-ion beam was irradiated at a sufficiently large area to cover the entire MoS_2 sample. The samples were irradiated using an Ar-ion beam in a high-vacuum chamber at room temperature with an acceleration voltage of 500 eV [7].

5.2.4 Raman spectroscopy

Raman spectroscopy is a method of measuring inelastic scattering of light on the surface of a material, and the Raman spectrum is the intensity of scattered light expressed as a function of the energy difference (energy loss) between incident light and scattered light. Energy loss due to inelastic scattering is mainly caused by phonons, which are elementary excitations of lattice vibrations in solids (molecules). By investigating the energy of phonons using Raman spectroscopy, it is possible to observe changes in the electronic structure that correlate with phonons.

Raman spectroscopy was performed on 1T-TaS_2 on a SiO_2 substrate. Using a microlaser Raman spectrometer (LabRam HR Evolution, HORIBA JOBIN YVON) at an excitation wavelength of 532 nm, a grating of 1800 gr/mm with an objective lens of 100x magnification, an ND filter of 5%, and an exposure time of 30 s. This was done with 10 integrations. For hydrogen adsorption study, the spectra of the exfoliated 1T-TaS_2 thin films transferred onto a SiO_2 (285 nm)/Si substrate were measured before and after H_2 gas exposure at the pressure of 22 and 100 Pa at 523 K for 20 min. Baseline fitting was performed using Gaussian curves centered at 0 cm^{-1} with respect to the Raman spectra [12].

5.3 Results and discussion

5.3.1 Layer number dependence of TaS_2

Fig. 5.4 shows the Raman spectra of different thicknesses of TaS_2 and Figs. 5.5–5.8 show the layer number dependence of each Raman peak intensity for bulk and thin-layer TaS_2. TaS_2 exhibits two characteristic Raman vibrational modes, and the E_{2g} mode at 270 cm^{-1} corresponds to in-plane vibrations due to the bond between Ta and S atoms [32][116]. Conversely, the A_{1g} mode near 380 cm^{-1} corresponds to out-of-plane vibrations caused by S atoms, and the other peaks are due to electron density wave (CDW) order, and these results are in good agreement with values presented in known literature [32]. As shown in Fig. 5.4, the peak intensity was weaker in the bulk sample than that in the thin-layer sample. This is thought to be because TaS_2 is a metal in the bulk state; therefore, an excess of conduction electrons exist, which shield the electric field of the incident excitation light. When comparing the cleaved thin-layer and bulk samples, the intensity of each peak relative to the Si peak of the substrate decreased as the number of layers increased. This is speculated to be because TaS_2 is a metal, and as the thickness of the number of layers increases, the reflection intensity ratio becomes stronger. Conversely, in Figs. 5.7–5.8, no dependence on the number of layers was observed in terms of peak width and peak position. Regarding the spectrum shown in Fig. 5.6, the dependence of the relative peak heights of the CDW peaks at 305 and 242 cm^{-1} on A_{1g} based on the number of layers increased as the number of layers decreased. This is thought to be related to the fact that TaS_2 behaves similar to a semiconductor as the number of carriers decreases with the reduction in the number of layers [11].

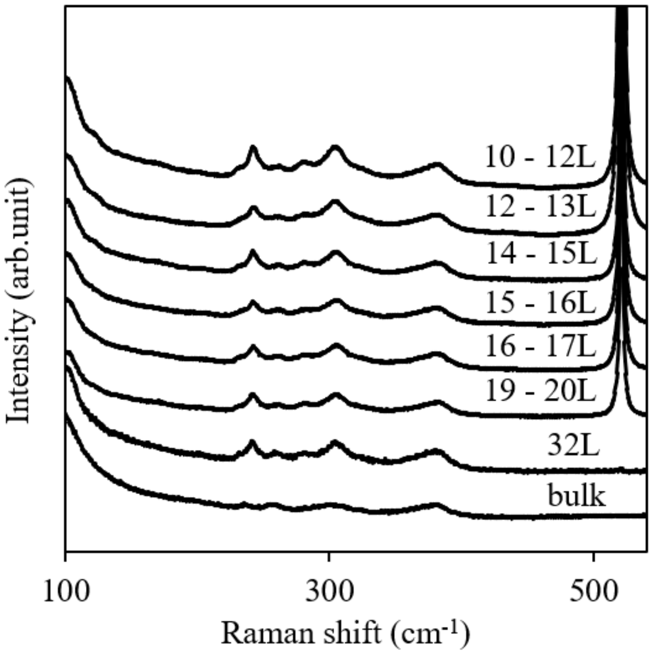

Fig. 5.4 Raman spectra of TaS_2 with different thicknesses.

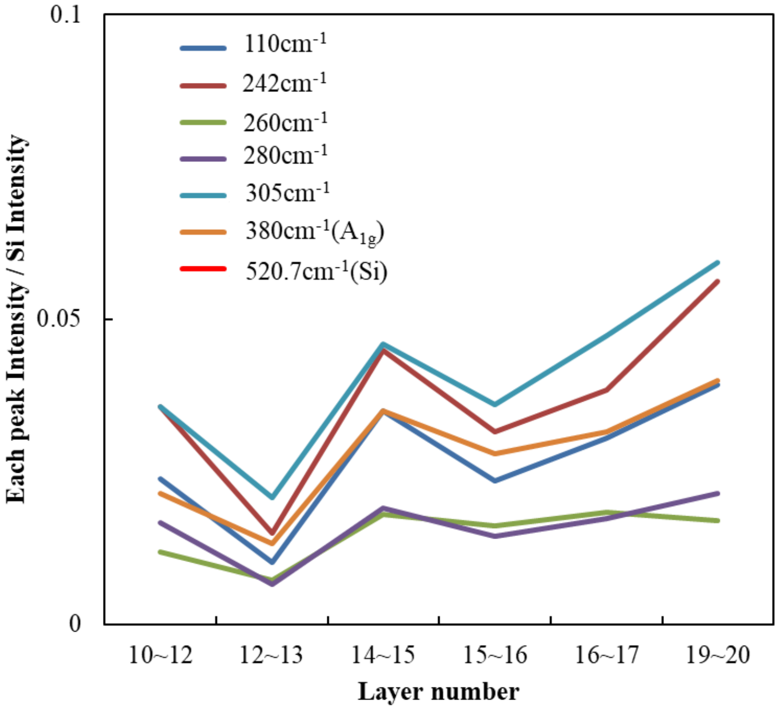

Fig. 5.5 Layer number dependence of ratio of each peak to Si peak for TaS_2

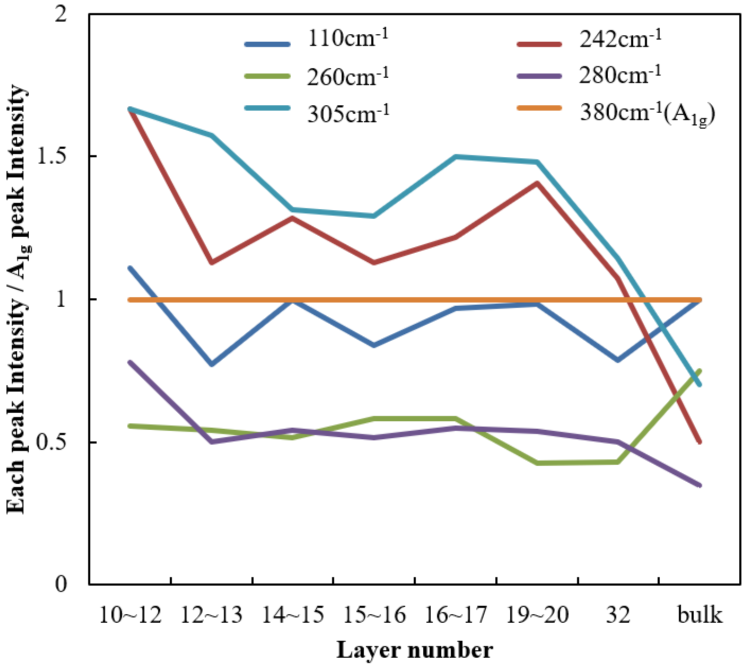

Fig. 5.6 Layer number dependence of ratio of each peak to A$_{1g}$ peak for TaS$_2$

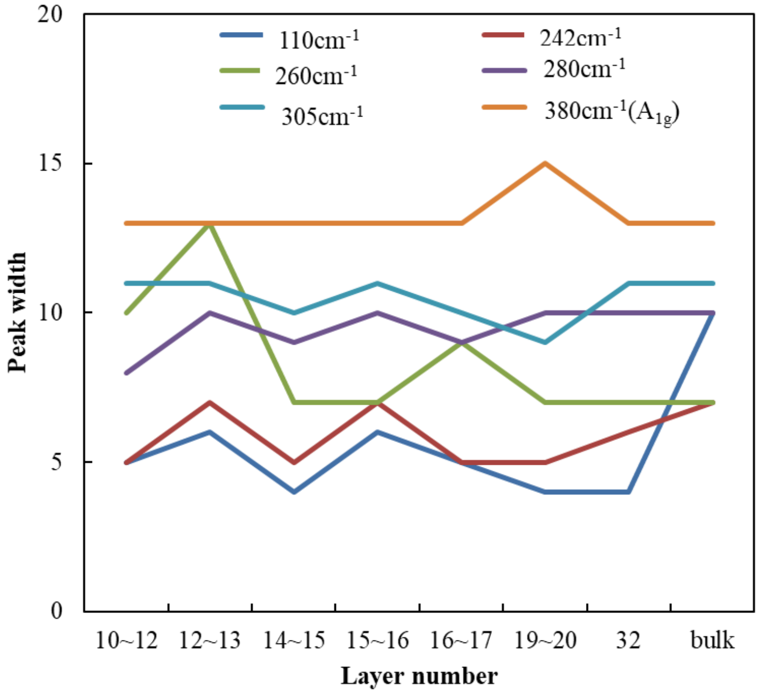

Fig. 5.7 Layer number dependence of peak width for TaS$_2$

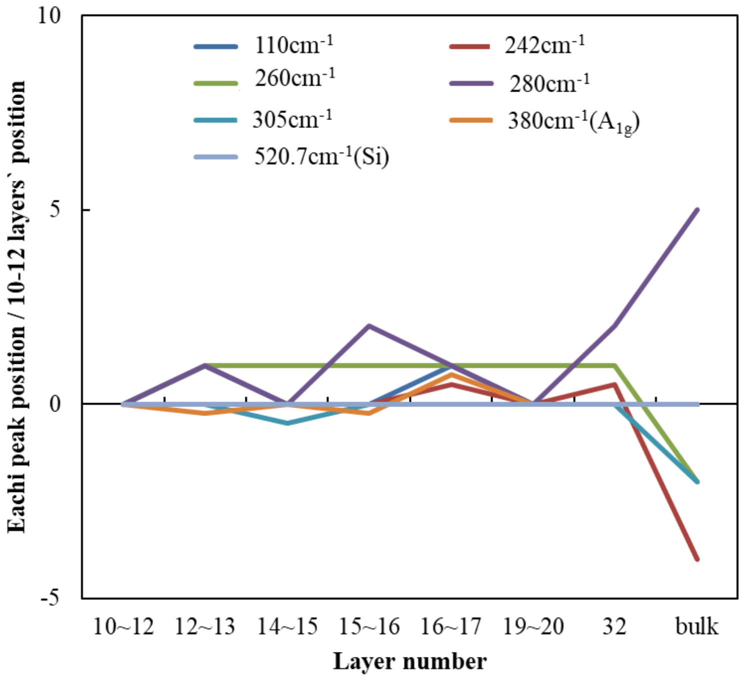

Fig.5.8 Layer number dependence of ratio of each peak position to peak position for TaS_2 with 10–12 layers

5.3.2 Effect of H_2 adsorption on TaS_2

Raman spectra for TaS_2 with ca. 14 layers were obtained before and after H_2 exposure, as shown in Fig. 5.9(a). The blue, black, and red lines in Fig. 5 9(a) are the spectra before H_2 exposure, after exposure to H_2 at 523 K, 22 Pa, and after exposure at 523 K, 100 Pa, respectively, where the reaction chamber was evacuated after 20 min of H_2 adsorption. Four large peaks near 102, 243, 306, and 374 cm^{-1} can be seen. Fig. 5.9(b) compares the peak heights around 243, 306, and 374 cm^{-1} between the samples (before H_2 exposure, after H^2 exposure at 22 Pa, and 100 Pa). The blue, black, and red–colored bars indicate the peak heights before H_2 exposure and after H_2 exposure at 22 Pa and 100 Pa, respectively. The peak heights are normalized to the height of the sample before H_2 exposure. The peak heights after H_2 exposure are almost the same as before H_2 exposure (the change ratio is within ± 5%). These positions are also unchanged before and after H_2 exposure, similar to the peak heights. These results indicate that the crystal structure of 1T-TaS_2 is not affected by H_2 adsorption and desorption. Further, these results suggest that the hydrogen gas is physically adsorbed on the 1T-TaS_2, and the structure of 1T-TaS_2

retains its original structure after H_2 evacuation [12].

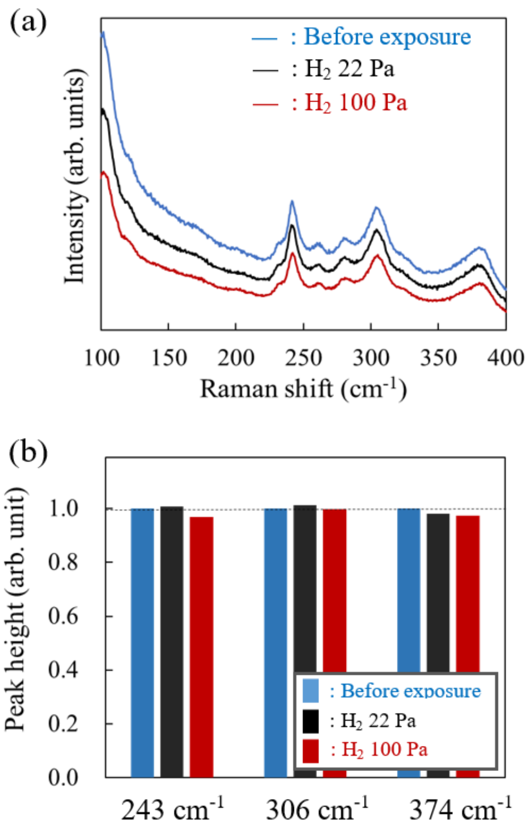

Fig. 5.9 Raman spectra of 1T-TaS_2 thin films having 14 layers in (a) before and after H_2 exposure and (b) comparison of the peak heights before and after H_2 exposure [12].

5.3.3 Effect of Ar-ion irradiation on TaS_2

The thin-layer TaS_2 sample was irradiated with Ar-ion beam irradiated at 500 eV acceleration voltage at a dose of 10^{15} cm^{-2}. TaS_2 is more resistant to radiation than MoS_2, where 100 eV Ar-ion irradiation does not affect the Raman spectra of TaS_2. This is considered due to the difference between Ta and Mo atoms. A theoretical study shows that different transition metals in transition metal disulfide can lead to different displacement threshold energies. The displacement threshold energy for WS_2 is higher than that for MoS_2, and both are higher than that for TiS_2 [117]. Considering that Ta has a similar atomic mass and electronic configuration with W, it has a higher threshold energy than 100 eV for vacancy introduction under Ar-ion irradiation. On the other hand, the TaS_2 sample is not monolayer, so it is more insensitive to the existence of vacancies. In this study, Ar-ion irradiation with a beam energy of 500 eV and high dose is performed for TaS_2.

After irradiation, almost all peaks became broader as shown in Fig. 5.10, suggesting that the growth of the region for the commensurate CDW ordering was hindered by the presence of defects introduced by the ion-beam irradiation, resulting in suppressed phase transition around room temperature.

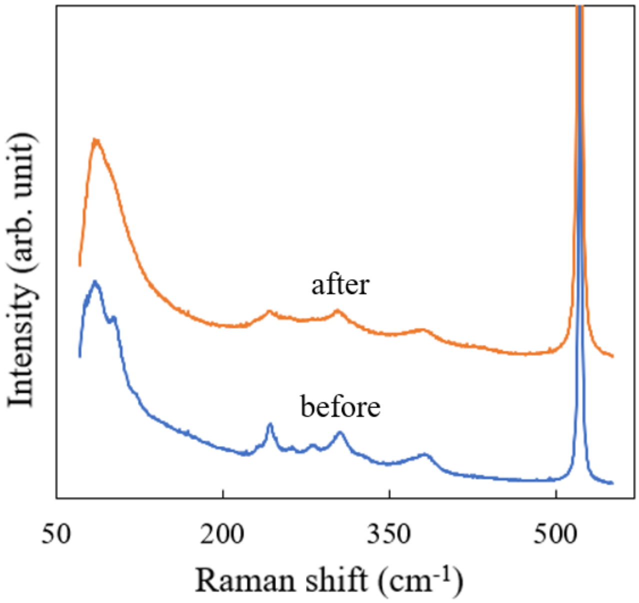

Fig. 5.10 Raman spectra of TaS_2 before (blue curve) and after (orange curve) Ar-ion irradiation.

5.4 Conclusion

To investigate the properties of thin-layer TaS_2, Raman spectroscopy measurements were performed in layer number, H_2 adsorption, and Ar-ion beam irradiation dependence. The layer number dependence measurements showed that peaks of TaS_2 are broadened as layer number increases and intensity decreases, owing to the screen effect of the electric field. The peak position and intensity are almost unchanged after H_2 exposure at several conditions, indicating that H_2 gas is physically adsorbed on the TaS_2. After Ar-ion beam irradiation at a dose of 10^{15} cm^{-2} with 500 eV of acceleration voltage, almost all peaks decreased and became broader, suggesting the transition of commensurate CDW ordering hindered by the introduced defects. Combining our conductivity measurement [12], a comprehensive study for thin-layer TaS_2 is provided, which could be a useful reference for future research applications such as gas sensors.

Chapter 6 Summary

2D materials have a 2D sheet structure in which atoms are arranged on a plane, which has received much attention recently. It has been expected to be applied as a new material that takes advantage of the unique properties derived from its two-dimensional structure. However, there are challenges in applying 2D materials, such as the existence of lattice vacancy, which is easy to be introduced during the fabrication, and difficulty in introducing impurities for chemical modification. In this study, the monolayer samples were modified by ion-beam irradiation to investigate the development of a new class of material. The novelty and effectiveness are in the following points.

2D materials with various electronic ground states, such as graphene (zero-gap semiconductor), MoS_2 (direct-gap semiconductor), and TaS_2 (metallic), were fabricated by mechanical exfoliation method and examined from the viewpoint of modifying and verifying the properties of 2D materials. Irradiation of the Ar-, Au-, I-, and Fe-ions beam, including Noble gas, nonmetallic, metallic, and magnetic elements, modified the 2D materials to introduce defects or impurities under a well-controlled condition.

Although there have been attempts to modulate the properties of 2D materials by ion-beam irradiation, they all involve direct irradiation of high-energy ion beams without sacrificial layers, which introduced vacancies and large-scale structural breakdown. In this study, to prevent high-energy ions from penetrating through the 2D material layer, an ultra-low energy ion beam below several hundreds of eV or NaCl thin-film sacrificial layer was fabricated in order to decrease the beam energy and distribute ions around the sample position. The properties of 2D materials on the structure were evaluated by Raman spectroscopy and Rutherford backscattering spectrometry, and the electronic properties were evaluated by photoluminescence and conductivity measurements using the field-effect transistor device structure.

We succeeded in intrinsically introducing irradiated ions as chemical species into a two-dimensional material, leading to the modulation of the degrees of freedom of charge and spin based on the irradiated ion species. In addition, by comprehensively evaluating zero-gap semiconductors, semiconductors, and metals as two-dimensional materials, we have provided broadly applicable material design guidelines for their application to electronic devices, environmentally friendly materials, and so on.

From this comprehensive study, the mechanism of ion-beam irradiation on 2D materials is investigated, and it will be a valuable tool for defect engineering in the fabrication process of devices based on 2D materials.

Research achievements

Journal Papers

1) Yangzhou Zhao, Yasushi Ishiguro, Kazuyuki Takai. Effect of low-energy ion-beam irradiation on the structure and electron transport of monolayer MoS_2. *Nuclear Inst. and Methods in Physics Research*, B, 543 (2023) 165095.
2) Yangzhou Zhao, Yasushi Ishiguro, Kosuke Nakamura, Hiroki Yoshimoto, Tomoaki Nishimura, Kazuyuki Takai. Effects of chemical modification using Au or I ion beam irradiation on the carrier transport properties of graphene. *Carbon Reports*, 3 (2024) 37-46.
3) Takumi Hidaka, Kosuke Nakamura, Hiroki Yoshimoto, Rintaro Suzuki, Yangzhou Zhao, Yasushi Ishiguro, Tomoaki Nishimura, Kazuyuki Takai. Changing the structural and electronic properties of graphene and related two-dimensional materials using ion beam irradiation with NaCl sacrificial layers. *Carbon Reports*, 1 (2022) 22-31.
4) Yasushi Ishiguro, Rintaro Suzuki, Yangzhou Zhao, Naoko Kodama, Kazuyuki Takai. Correlation between charge density wave phase transition and hydrogen adsorption in 1T-TaS_2 thin film devices. *Nanotechnology*, 34 (2023) 275701.

International Conference Presentations

1) Yangzhou Zhao, Hiroki Yokata, Haruna Ichikawa, Kazuyuki Takai. Effects of defect formation in monolayer MoS_2 by low energy Ar^+ ion beam irradiation. *The 11th International Conference on Recent Progress in Graphene Research*, 9P-31, October 2019.
2) Yangzhou Zhao, Hiroki Yokata, Haruna Ichikawa, Kazuyuki Takai. Ion-beam irradiation effects on the structure and electronic properties of MoS_2. *1&2DM 2020 International Conference*, No.7, January 2020.
3) Yangzhou Zhao, Yasushi Ishiguro, Hiroki Yokota, Haruna Ichikawa, Kazuyuki Takai. Effects of defect formation by low energy Ar^+ ion beam irradiation in monolayer

MoS_2. *International Conference on the Science and Application of Nanotubes and Low-Dimensional Materials 2021*, C-97, June 2021.

Domestic Conference Presentations

1) Yangzhou Zhao, Hiroki Yokata, Haruna Ichikawa, Kazuyuki Takai. Ion-beam irradiation effects on the structure and electronic properties of MoS_2. *Annual Meeting of the Japan Society of Vacuum and Surface Science 2019*, 1P-52, October 2019.
2) Yangzhou Zhao, Hiroki Yokata, Haruna Ichikawa, Kazuyuki Takai. Ion-beam irradiation effects on the structure and electronic properties of MoS_2. *The 38th Symposium on Materials Science and Engineering Research Center of Ion Beam Technology*, No.9, December 2019.
3) Yangzhou Zhao, Hiroki Yokata, Haruna Ichikawa, Yasushi Ishiguro, Kazuyuki Takai. Effects of defect formation in monolayer MoS_2 by low energy Ar^+ ion beam irradiation. *The 59th Fullerenes-Nanotubes-Graphene General Symposium*, 2P-24, September 2020.
4) Yangzhou Zhao, Hiroki Yokota, Haruna Ichikawa, Kazuyuki Takai. Effects of lattice vacancies introduced by ion-beam irradiation in monolayer MoS_2. *The 40th Symposium on Materials Science and Engineering Research Center of Ion Beam Technology*, No.21, December 2021.
5) Yangzhou Zhao, Hiroki Yokota, Haruna Ichikawa, Yasushi Ishiguro, Kazuyuki Takai. Introducing lattice vacancies as adsorption sites in monolayer MoS_2. *The 62nd Fullerenes-Nanotubes-Graphene General Symposium*, 1P-29, March 2022.
6) Yangzhou Zhao, Hiroki Yokota, Haruna Ichikawa, Kazuyuki Takai. Effects of lattice vacancies introduced by ion-beam irradiation in monolayer MoS_2. *The 69th JSAP Spring Meeting 2022*, 22p-P06-18, March 2022.
7) Yangzhou Zhao, Kosuke Nakamura, Hiroki Yoshimoto, Tomoaki Nishimura, Kazuyuki Takai. Tuning structure and electron transport properties of Graphene by chemical modification using Ion-beam irradiation. *The 41st Symposium on Materials Science and Engineering Research Center of Ion Beam Technology*, No.19, December 2022.
8) Yangzhou Zhao, Kosuke Nakamura, Hiroki Yoshimoto, Tomoaki Nishimura,

Kazuyuki Takai. Tuning structure and electron transport properties of 2D materials by chemical modification using Ion-beam irradiation. *The 64th Fullerenes-Nanotubes-Graphene General Symposium*, 1P-35, March 2023.

9) Yangzhou Zhao, Kosuke Nakamura, Hiroki Yoshimoto, Tomoaki Nishimura, Kazuyuki Takai. Tuning structure and electron transport properties of graphene by chemical modification using ion-beam irradiation. *50th Annual Meeting of The Carbon Society of Japan*, 2A03, November 2023.
10) Yangzhou Zhao, Hiroki Yokota, Haruna Ichikawa, Kosuke Nakamura, Hiroki Yoshimoto, Takumi Hidaka, Yasushi Ishiguro, Tomoaki Nishimura, Kazuyuki Takai. Tuning structure and electronic properties of 2D materials by ion-beam irradiation. *The 42nd Symposium on Materials Science and Engineering Research Center of Ion Beam Technology*, No.7, December 2023.

Acknowledgement

Throughout the journey of my Ph.D. research and dissertation writing, I wish to convey my sincere appreciation to all those who have contributed to my endeavors.

First and foremost, I would like to extend my heartfelt gratitude to my supervisor, Prof. Kazuyuki TAKAI, whose kindness, illuminating guidance, and profound knowledge have been invaluable. I am genuinely thankful for the support received not only in navigating the intricacies of my research topic but also in addressing a broader spectrum of scientific matters.

I would like to express my thanks to my dissertation referees, Prof. Hironori OGATA and Prof. Akihiro YAMASHITA, for their insightful feedback and constructive comments, which have greatly enhanced the quality of my academic work.

To my colleagues in Takai Lab, I appreciate not only your support in research but also in various aspects of life. Thank you very much. Additionally, I would like to extend my thanks to Dr. Ishiguro and Mr. Miyake for their flexible assistance, spanning both experimental support and the management of equipments.

Lastly, I convey my appreciation to my dearest family for their unwavering encouragement and generous support throughout this journey.

Reference

[1] K. S. Novoselov *et al.*, “Electric Field Effect in Atomically Thin Carbon Films,” *Science (1979)*, vol. 306, no. 5696, pp. 666–669, Oct. 2004, doi: 10.1126/science.1102896.

[2] X. Li and H. Zhu, “Two-dimensional MoS_2: Properties, preparation, and applications,” *Journal of Materiomics*, vol. 1, no. 1, pp. 33–44, Mar. 2015, doi: 10.1016/j.jmat.2015.03.003.

[3] K. Takai, S. Tsujimura, F. Kang, and M. Inagaki, *Graphene: Preparations, Properties, Applications, and Prospects*. Elsevier, 2019. doi: 10.1016/C2019-0-00212-9.

[4] A. H. Castro Neto, F. Guinea, N. M. R. Peres, K. S. Novoselov, and A. K. Geim, “The electronic properties of graphene,” *Rev Mod Phys*, vol. 81, no. 1, pp. 109–162, Jan. 2009, doi: 10.1103/RevModPhys.81.109.

[5] Y. Li, C.-Y. Xu, P. Hu, and L. Zhen, “Carrier Control of MoS_2 Nanoflakes by Functional Self-Assembled Monolayers,” *ACS Nano*, vol. 7, no. 9, pp. 7795–7804, Sep. 2013, doi: 10.1021/nn402682j.

[6] S. Bae, N. Sugiyama, T. Matsuo, H. Raebiger, K. Shudo, and K. Ohno, “Defect-induced vibration modes of Ar^+-irradiated MoS_2,” *Phys Rev Appl*, vol. 7, no. 2, p. 024001, Feb. 2017, doi: 10.1103/PhysRevApplied.7.024001.

[7] Y. Zhao, Y. Ishiguro, and K. Takai, “Effect of low-energy ion-beam irradiation on the structure and electron transport of monolayer MoS_2,” *Nucl Instrum Methods Phys Res B*, vol. 543, p. 165095, Oct. 2023, doi: 10.1016/j.nimb.2023.165095.

[8] A. Splendiani *et al.*, “Emerging Photoluminescence in Monolayer MoS_2,” *Nano Lett*, vol. 10, no. 4, pp. 1271–1275, Apr. 2010, doi: 10.1021/nl903868w.

[9] B. Chakraborty, A. Bera, D. V. S. Muthu, S. Bhowmick, U. V. Waghmare, and A. K. Sood, “Symmetry-dependent phonon renormalization in monolayer MoS_2 transistor,” *Phys Rev B*, vol. 85, no. 16, p. 161403, Apr. 2012, doi: 10.1103/PhysRevB.85.161403.

[10] K. F. Mak, K. He, J. Shan, and T. F. Heinz, “Control of valley polarization in monolayer MoS_2 by optical helicity,” *Nat Nanotechnol*, vol. 7, no.

8, pp. 494–498, Aug. 2012, doi: 10.1038/nnano.2012.96.

[11] Y. Ishiguro *et al.*, “Layer Number Dependence of Charge Density Wave Phase Transition Between Nearly-Commensurate and Incommensurate Phases in 1T-TaS$_2$,” *The Journal of Physical Chemistry C*, vol. 124, no. 49, pp. 27176–27184, Dec. 2020, doi: 10.1021/acs.jpcc.0c08414.

[12] Y. Ishiguro, R. Suzuki, Z. Yangzhou, N. Kodama, and K. Takai, “Correlation between charge density wave phase transition and hydrogen adsorption in 1T-TaS$_2$ thin film devices,” *Nanotechnology*, vol. 34, no. 27, p. 275701, Jul. 2023, doi: 10.1088/1361-6528/acc8db.

[13] P. Blake *et al.*, “Making graphene visible,” *Appl Phys Lett*, vol. 91, no. 6, p. 063124, Aug. 2007, doi: 10.1063/1.2768624.

[14] P. Ahlberg *et al.*, “Defect formation in graphene during low-energy ion bombardment,” *APL Mater*, vol. 4, no. 4, Apr. 2016, doi: 10.1063/1.4945587.

[15] Y. Chen *et al.*, “Tuning Electronic Structure of Single Layer MoS$_2$ through Defect and Interface Engineering,” *ACS Nano*, vol. 12, no. 3, pp. 2569–2579, Mar. 2018, doi: 10.1021/acsnano.7b08418.

[16] S. F. A. Rahman, A. M. Hashim, and S. Kasai, “Identification of Graphene Layer Numbers from Color Combination Contrast Image for Wide-Area Characterization,” *Jpn J Appl Phys*, vol. 51, no. 6S, p. 06FD09, Jun. 2012, doi: 10.1143/JJAP.51.06FD09.

[17] H. Li, J. Wu, Z. Yin, and H. Zhang, “Preparation and Applications of Mechanically Exfoliated Single-Layer and Multilayer MoS$_2$ and WSe$_2$ Nanosheets,” *Acc Chem Res*, vol. 47, no. 4, pp. 1067–1075, Apr. 2014, doi: 10.1021/ar4002312.

[18] X. Cong, X.-L. Liu, M.-L. Lin, and P.-H. Tan, “Application of Raman spectroscopy to probe fundamental properties of two-dimensional materials,” *NPJ 2D Mater Appl*, vol. 4, no. 1, p. 13, May 2020, doi: 10.1038/s41699-020-0140-4.

[19] M. M. Lucchese *et al.*, “Quantifying ion-induced defects and Raman relaxation length in graphene,” *Carbon N Y*, vol. 48, no. 5, pp. 1592–1597, Apr. 2010, doi: 10.1016/j.carbon.2009.12.057.

[20] V. Yu, “Optics and chemical vapour deposition of graphene monolayers on various substrates,” Ph.D. thesis, Mcgill University, 2010. [Online]. Available: https://escholarship.mcgill.ca/concern/theses/xp68kg570

[21] A. C. Ferrari *et al.*, “Raman Spectrum of Graphene and Graphene Layers,” *Phys Rev Lett*, vol. 97, no. 18, p. 187401, Oct. 2006, doi: 10.1103/PhysRevLett.97.187401.

[22] L. M. Malard, M. A. Pimenta, G. Dresselhaus, and M. S. Dresselhaus, “Raman spectroscopy in graphene,” *Phys Rep*, vol. 473, no. 5–6, pp. 51–87, Apr. 2009, doi: 10.1016/j.physrep.2009.02.003.

[23] C. Casiraghi and D. Prezzi, “Raman Spectroscopy of Graphene Nanoribbons: A Review,” in *In GraphITA: Selected papers from the Workshop on Synthesis, Characterization and Technological Exploitation of Graphene and 2D Materials Beyond Graphene*, 2017, pp. 19–30. doi: 10.1007/978-3-319-58134-7_2.

[24] J. Yan, Y. Zhang, P. Kim, and A. Pinczuk, “Electric Field Effect Tuning of Electron-Phonon Coupling in Graphene,” *Phys Rev Lett*, vol. 98, no. 16, p. 166802, Apr. 2007, doi: 10.1103/PhysRevLett.98.166802.

[25] A. Das *et al.*, “Monitoring dopants by Raman scattering in an electrochemically top-gated graphene transistor,” *Nat Nanotechnol*, vol. 3, no. 4, pp. 210–215, Apr. 2008, doi: 10.1038/nnano.2008.67.

[26] L. Liang and V. Meunier, “First-principles Raman spectra of MoS_2, WS_2 and their heterostructures,” *Nanoscale*, vol. 6, no. 10, p. 5394, 2014, doi: 10.1039/c3nr06906k.

[27] S. L. L. M. Ramos *et al.*, “Suppression of the commensurate charge density wave phase in ultrathin 1T-TaS_2 evidenced by Raman hyperspectral analysis,” *Phys Rev B*, vol. 100, no. 16, p. 165414, Oct. 2019, doi: 10.1103/PhysRevB.100.165414.

[28] W. Wen, Y. Zhu, C. Dang, W. Chen, and L. Xie, “Raman Spectroscopic and Dynamic Electrical Investigation of Multi-State Charge-Wave-Density Phase Transitions in 1T-TaS_2,” *Nano Lett*, vol. 19, no. 3, pp. 1805–1813, Mar. 2019, doi: 10.1021/acs.nanolett.8b04855.

[29] R. Zhao *et al.*, “Tuning Phase Transitions in 1T-TaS_2 via the Substrate,” *Nano Lett*, vol. 17, no. 6, pp. 3471–3477, Jun. 2017, doi: 10.1021/acs.nanolett.7b00418.

[30] O. R. Albertini *et al.*, “Zone-center phonons of bulk, few-layer, and monolayer 1T-TaS_2: Detection of commensurate charge density wave phase through Raman scattering,” *Phys Rev B*, vol. 93, no. 21, p. 214109, Jun. 2016, doi:

10.1103/PhysRevB.93.214109.

[31] C. Zhu *et al.*, “Light-Tunable 1T-TaS_2 Charge-Density-Wave Oscillators,” *ACS Nano*, vol. 12, no. 11, pp. 11203–11210, Nov. 2018, doi: 10.1021/acsnano.8b05756.

[32] T. Hirata and F. S. Ohuchi, “Temperature dependence of the Raman spectra of 1T-TaS_2,” *Solid State Commun*, vol. 117, no. 6, pp. 361–364, Jan. 2001, doi: 10.1016/S0038-1098(00)00468-3.

[33] J. Joshi *et al.*, “Short-range charge density wave order in 2H-TaS_2,” *Phys Rev B*, vol. 99, no. 24, p. 245144, Jun. 2019, doi: 10.1103/PhysRevB.99.245144.

[34] J. W. Christopher, B. B. Goldberg, and A. K. Swan, “Long tailed trions in monolayer MoS_2: Temperature dependent asymmetry and resulting red-shift of trion photoluminescence spectra,” *Sci Rep*, vol. 7, no. 1, p. 14062, Oct. 2017, doi: 10.1038/s41598-017-14378-w.

[35] K. F. Mak *et al.*, “Tightly bound trions in monolayer MoS_2,” *Nat Mater*, vol. 12, no. 3, pp. 207–211, Mar. 2013, doi: 10.1038/nmat3505.

[36] F. Junge, M. Auge, and H. Hofsäss, “Sputter hot filament hollow cathode ion source and its application to ultra-low energy ion implantation in 2D materials,” *Nucl Instrum Methods Phys Res B*, vol. 510, pp. 63–68, Jan. 2022, doi: 10.1016/j.nimb.2021.10.017.

[37] S. B. Mitta *et al.*, “Electrical characterization of 2D materials-based field-effect transistors,” *2d Mater*, vol. 8, no. 1, p. 012002, Jan. 2021, doi: 10.1088/2053-1583/abc187.

[38] Y. Sato, K. Takai, and T. Enoki, “Electrically Controlled Adsorption of Oxygen in Bilayer Graphene Devices,” *Nano Lett*, vol. 11, no. 8, pp. 3468–3475, Aug. 2011, doi: 10.1021/nl202002p.

[39] F. Schedin *et al.*, “Detection of individual gas molecules adsorbed on graphene,” *Nat Mater*, vol. 6, no. 9, pp. 652–655, Sep. 2007, doi: 10.1038/nmat1967.

[40] X. Zhang *et al.*, “Single-Atom Vacancy Doping in Two-Dimensional Transition Metal Dichalcogenides,” *Acc Mater Res*, vol. 2, no. 8, pp. 655–668, Aug. 2021, doi: 10.1021/accountsmr.1c00097.

[41] R. Saito, M. Hofmann, G. Dresselhaus, A. Jorio, and M. S. Dresselhaus,

"Raman spectroscopy of graphene and carbon nanotubes," *Adv Phys*, vol. 60, no. 3, pp. 413–550, Jun. 2011, doi: 10.1080/00018732.2011.582251.

[42] J. F. Gibbons, "Ion implantation in semiconductors—Part II: Damage production and annealing," *Proceedings of the IEEE*, vol. 60, no. 9, pp. 1062–1096, 1972, doi: 10.1109/PROC.1972.8854.

[43] O. Ochedowski *et al.*, "Radiation hardness of graphene and MoS_2 field effect devices against swift heavy ion irradiation," *J Appl Phys*, vol. 113, no. 21, Jun. 2013, doi: 10.1063/1.4808460.

[44] S. Kumar, A. Kumar, A. Tripathi, C. Tyagi, and D. K. Avasthi, "Engineering of electronic properties of single layer graphene by swift heavy ion irradiation," *J Appl Phys*, vol. 123, p. 161533, Apr. 2018, doi: 10.1063/1.4991990.

[45] Z. He *et al.*, "Spectroscopic investigation of defects mediated oxidization of single-layer MoS_2," *Sci China Technol Sci*, vol. 64, no. 3, pp. 611–619, Mar. 2021, doi: 10.1007/s11431-020-1593-4.

[46] B. Guo, Q. Liu, E. Chen, H. Zhu, L. Fang, and J. R. Gong, "Controllable N-Doping of Graphene," *Nano Lett*, vol. 10, no. 12, pp. 4975–4980, Dec. 2010, doi: 10.1021/nl103079j.

[47] M. Petrović *et al.*, "The mechanism of caesium intercalation of graphene," *Nat Commun*, vol. 4, no. 1, p. 2772, Nov. 2013, doi: 10.1038/ncomms3772.

[48] D. Wei, Y. Liu, Y. Wang, H. Zhang, L. Huang, and G. Yu, "Synthesis of N-Doped Graphene by Chemical Vapor Deposition and Its Electrical Properties," *Nano Lett*, vol. 9, no. 5, pp. 1752–1758, May 2009, doi: 10.1021/nl803279t.

[49] H. Qi *et al.*, "Fabrication of sub-nanometer pores on graphene membrane for ion selective transport," *Nanoscale*, vol. 10, no. 11, pp. 5350–5357, 2018, doi: 10.1039/C8NR00050F.

[50] Y. Kudo, M. Kiguchi, J. Takashiro, K. Takai, and T. Enoki, "Development of edge state on graphite surface induced by Ar^+ irradiation studied using near-edge X-ray absorption fine structure spectroscopy," *Carbon N Y*, vol. 72, pp. 152–159, Jun. 2014, doi: 10.1016/j.carbon.2014.01.067.

[51] Y. Zhao, Y. Ishiguro, K. Nakamura, H. Yoshimoto, T. Nishimura, and K. Takai, "Effects of chemical modification using Au or I ion beam irradiation on the carrier transport properties of graphene," *Carbon Reports*, vol. 3, no. 1, pp. 37–46,

2024, doi: 10.7209/carbon.030104.

[52] J. P. Biersack and L. G. Haggmark, “A Monte Carlo computer program for the transport of energetic ions in amorphous targets,” *Nuclear Instruments and Methods*, vol. 174, no. 1–2, pp. 257–269, Aug. 1980, doi: 10.1016/0029-554X(80)90440-1.

[53] F. Z. James, “James Ziegler - SRIM & TRIM.” [Online]. Available: http://www.srim.org/

[54] S. Agarwal, Y. Lin, C. Li, R. E. Stoller, and S. J. Zinkle, “On the use of SRIM for calculating vacancy production: Quick calculation and full-cascade options,” *Nucl Instrum Methods Phys Res B*, vol. 503, pp. 11–29, Sep. 2021, doi: 10.1016/j.nimb.2021.06.018.

[55] P. Baldez *et al.*, “Measurements of ^{252}Cf fission product energy loss through thin silicon nitride and carbon foils, and comparison with SRIM-2013 and MCNP6.2 simulations,” *Nucl Instrum Methods Phys Res B*, vol. 456, pp. 142–147, Oct. 2019, doi: 10.1016/j.nimb.2019.06.027.

[56] S.-M. He, C.-C. Huang, J.-W. Liou, W.-Y. Woon, and C.-Y. Su, “Spectroscopic and Electrical Characterizations of Low-Damage Phosphorous-Doped Graphene via Ion Implantation,” *ACS Appl Mater Interfaces*, vol. 11, no. 50, pp. 47289–47298, Dec. 2019, doi: 10.1021/acsami.9b18479.

[57] Y. Li, G. Kuang, Z. Jiao, L. Yao, and R. Duan, “Recent progress on the mechanical exfoliation of 2D transition metal dichalcogenides,” *Mater Res Express*, vol. 9, no. 12, p. 122001, Dec. 2022, doi: 10.1088/2053-1591/aca6c6.

[58] K. Yokota, K. Takai, Y. Kudo, Y. Sato, and T. Enoki, “Polaron coupling in graphene field effect transistors on patterned self-assembled monolayer,” *Physical Chemistry Chemical Physics*, vol. 16, no. 9, p. 4313, 2014, doi: 10.1039/c3cp54669a.

[59] G. Gawlik, P. Ciepielewski, J. Jagielski, and J. Baranowski, “Modification of graphene by ion beam,” *Nucl Instrum Methods Phys Res B*, vol. 406, pp. 683–688, Sep. 2017, doi: 10.1016/j.nimb.2017.04.054.

[60] Y. Zhang, X. Chen, H. Wang, J. Dai, J. Xue, and X. Guo, “Electronic Properties of Multilayer MoS_2 Field Effect Transistor with Unique Irradiation Resistance,” *The Journal of Physical Chemistry C*, vol. 125, no. 3, pp. 2089–2096, Jan. 2021, doi: 10.1021/acs.jpcc.0c09666.

[61] T. Hidaka *et al.*, “Changing the structural and electronic properties of graphene and related two-dimensional materials using ion beam irradiation with NaCl sacrificial layers,” *Carbon Reports*, vol. 1, no. 1, p. 22, Mar. 2022, doi: 10.7209/carbon.1.1_22.

[62] X. Wu, X. Zhu, and B. Lei, “Impact of ion beam irradiation on two-dimensional MoS_2 : a molecular dynamics simulation study,” *Journal of Physics: Condensed Matter*, vol. 34, no. 5, p. 055402, Feb. 2022, doi: 10.1088/1361-648X/ac31f9.

[63] K. Barthelmi *et al.*, “Atomistic defects as single-photon emitters in atomically thin MoS_2,” *Appl Phys Lett*, vol. 117, no. 7, Aug. 2020, doi: 10.1063/5.0018557.

[64] J. Klein *et al.*, “Engineering the Luminescence and Generation of Individual Defect Emitters in Atomically Thin MoS_2,” *ACS Photonics*, vol. 8, no. 2, pp. 669–677, Feb. 2021, doi: 10.1021/acsphotonics.0c01907.

[65] S. W. Han *et al.*, “Hole doping effect of MoS_2 via electron capture of He^+ ion irradiation,” *Sci Rep*, vol. 11, no. 1, p. 23590, Dec. 2021, doi: 10.1038/s41598-021-02932-6.

[66] S. W. Han, W. S. Yun, M. Kang, S. Lee, and J. Park, “Phase transition of a MoS_2 monolayer through top layer desulfurization by He^+ ion irradiation,” *J Appl Phys*, vol. 131, no. 22, Jun. 2022, doi: 10.1063/5.0092955.

[67] Y. Manzanares-Negro *et al.*, “Confined Crack Propagation in MoS_2 Monolayers by Creating Atomic Vacancies,” *ACS Nano*, vol. 15, no. 1, pp. 1210–1216, Jan. 2021, doi: 10.1021/acsnano.0c08235.

[68] X. Wu and X. Zhu, “Molecular dynamics simulations of ion beam irradiation on graphene/MoS_2 heterostructure,” *Sci Rep*, vol. 11, no. 1, p. 21113, Oct. 2021, doi: 10.1038/s41598-021-00582-2.

[69] J. A. Kropp, A. Sharma, W. Zhu, C. Ataca, and T. Gougousi, “Surface Defect Engineering of MoS_2 for Atomic Layer Deposition of TiO_2 Films,” *ACS Appl Mater Interfaces*, vol. 12, no. 42, pp. 48150–48160, Oct. 2020, doi: 10.1021/acsami.0c13095.

[70] P. Valerius *et al.*, “Reversible crystalline-to-amorphous phase transformation in monolayer MoS_2 under grazing ion irradiation,” *2d Mater*, vol. 7, no. 2, p. 025005, Jan. 2020, doi: 10.1088/2053-1583/ab5df4.

[71] X. Wu, R. Yang, X. Chen, and W. Liu, “Fabrication of Nanopore in MoS_2-Graphene vdW Heterostructure by Ion Beam Irradiation and the Mechanical Performance,” *Nanomaterials*, vol. 12, no. 2, p. 196, Jan. 2022, doi: 10.3390/nano12020196.

[72] S. Ahmed *et al.*, “Inducing High Coercivity in MoS_2 Nanosheets by Transition Element Doping,” *Chemistry of Materials*, vol. 29, no. 21, pp. 9066–9074, Nov. 2017, doi: 10.1021/acs.chemmater.7b02593.

[73] B. C. Windom, W. G. Sawyer, and D. W. Hahn, “A Raman Spectroscopic Study of MoS_2 and MoO_3: Applications to Tribological Systems,” *Tribol Lett*, vol. 42, no. 3, pp. 301–310, Jun. 2011, doi: 10.1007/s11249-011-9774-x.

[74] M. Ghorbani-Asl, S. Kretschmer, D. E. Spearot, and A. V Krasheninnikov, “Two-dimensional MoS_2 under ion irradiation: from controlled defect production to electronic structure engineering,” *2d Mater*, vol. 4, no. 2, p. 025078, Jun. 2017, doi: 10.1088/2053-1583/aa6b17.

[75] Z. Kou, A. Hashemi, M. J. Puska, A. V. Krasheninnikov, and H.-P. Komsa, “Simulating Raman spectra by combining first-principles and empirical potential approaches with application to defective MoS_2,” *NPJ Comput Mater*, vol. 6, no. 1, p. 59, May 2020, doi: 10.1038/s41524-020-0320-y.

[76] B. R. Carvalho *et al.*, “Intervalley scattering by acoustic phonons in two-dimensional MoS_2 revealed by double-resonance Raman spectroscopy,” *Nat Commun*, vol. 8, no. 1, p. 14670, Mar. 2017, doi: 10.1038/ncomms14670.

[77] J. F. Ziegler, M. D. Ziegler, and J. P. Biersack, “SRIM – The stopping and range of ions in matter (2010),” *Nucl Instrum Methods Phys Res B*, vol. 268, no. 11–12, pp. 1818–1823, Jun. 2010, doi: 10.1016/j.nimb.2010.02.091.

[78] M. Tangi *et al.*, “Anomalous photoluminescence thermal quenching of sandwiched single layer MoS_2,” *Opt Mater Express*, vol. 7, no. 10, p. 3697, Oct. 2017, doi: 10.1364/OME.7.003697.

[79] H. Nan *et al.*, “Strong Photoluminescence Enhancement of MoS_2 through Defect Engineering and Oxygen Bonding,” *ACS Nano*, vol. 8, no. 6, pp. 5738–5745, Jun. 2014, doi: 10.1021/nn500532f.

[80] H. Shibata, “Negative Thermal Quenching Curves in Photoluminescence of Solids,” *Jpn J Appl Phys*, vol. 37, no. 2R, p. 550, Feb. 1998,

doi: 10.1143/JJAP.37.550.

[81] F. Barakat, A. Laref, S. Alterary, S. Faraji, and M. Alsalhi, “Structural and optical behaviors of 2D-layered molybdenum disulfide thin film: experimental and ab-initio insights,” *Journal of Materials Research and Technology*, vol. 14, pp. 780–796, Sep. 2021, doi: 10.1016/j.jmrt.2021.06.059.

[82] X. Liao, X. Zhang, K. Takai, and T. Enoki, “Electric field induced sp^3-to-sp^2 conversion and nonlinear electron transport in iron-doped diamond-like carbon thin film,” *J Appl Phys*, vol. 107, no. 1, Jan. 2010, doi: 10.1063/1.3280037.

[83] K. Takai, T. Suzuki, T. Enoki, H. Nishihara, and T. Kyotani, “Structure and magnetic properties of curved graphene networks and the effects of bromine and potassium adsorption,” *Phys Rev B*, vol. 81, no. 20, p. 205420, May 2010, doi: 10.1103/PhysRevB.81.205420.

[84] K. Takai *et al.*, “Magnetic Potassium Clusters in a Nanographite Host System,” *Phys Rev Lett*, vol. 98, no. 1, p. 017203, Jan. 2007, doi: 10.1103/PhysRevLett.98.017203.

[85] K. Savaram *et al.*, “Dry microwave heating enables scalable fabrication of pristine holey graphene nanoplatelets and their catalysis in reductive hydrogen atom transfer reactions,” *Carbon N Y*, vol. 139, pp. 861–871, Nov. 2018, doi: 10.1016/j.carbon.2018.07.047.

[86] S. Hao, K. Takai, F. Kang, and T. Enoki, “Electronic and magnetic properties of acid-adsorbed nanoporous activated carbon fibers,” *Carbon N Y*, vol. 46, no. 1, pp. 110–116, Jan. 2008, doi: 10.1016/j.carbon.2007.10.037.

[87] A. G. Rybkin *et al.*, “Magneto-Spin–Orbit Graphene: Interplay between Exchange and Spin–Orbit Couplings,” *Nano Lett*, vol. 18, no. 3, pp. 1564–1574, Mar. 2018, doi: 10.1021/acs.nanolett.7b01548.

[88] M. Shiraishi and T. Ikoma, “Molecular spintronics,” *Physica E Low Dimens Syst Nanostruct*, vol. 43, no. 7, pp. 1295–1317, May 2011, doi: 10.1016/j.physe.2011.02.010.

[89] L. C. Feldman and J. W. Mayer, *Fundamentals of Surface Thin Film Analysis*. Prentice Hall, 1986.

[90] G. H. Kinchin and R. S. Pease, “The Displacement of Atoms in Solids by Radiation,” *Reports on Progress in Physics*, vol. 18, no. 1, p. 301, Jan. 1955, doi: 10.1088/0034-4885/18/1/301.

[91] M. J. Norgett, M. T. Robinson, and I. M. Torrens, “A proposed method of calculating displacement dose rates,” *Nuclear Engineering and Design*, vol. 33, no. 1, pp. 50–54, Aug. 1975, doi: 10.1016/0029-5493(75)90035-7.

[92] D. Tristant, P. Puech, and I. C. Gerber, “Theoretical Study of Graphene Doping Mechanism by Iodine Molecules,” *The Journal of Physical Chemistry C*, vol. 119, no. 21, pp. 12071–12078, May 2015, doi: 10.1021/acs.jpcc.5b03246.

[93] A. M. Shikin, G. V. Prudnikova, V. K. Adamchuk, F. Moresco, and K.-H. Rieder, “Surface intercalation of gold underneath a graphite monolayer on Ni(111) studied by angle-resolved photoemission and high-resolution electron-energy-loss spectroscopy,” *Phys Rev B*, vol. 62, no. 19, pp. 13202–13208, Nov. 2000, doi: 10.1103/PhysRevB.62.13202.

[94] Y. Wu *et al.*, “Tuning the Doping Type and Level of Graphene with Different Gold Configurations,” *Small*, vol. 8, no. 20, pp. 3129–3136, Oct. 2012, doi: 10.1002/smll.201200520.

[95] R. C. O’Rourke, “Absorption of Light by Trapped Electrons,” *Physical Review*, vol. 91, no. 2, pp. 265–270, Jul. 1953, doi: 10.1103/PhysRev.91.265.

[96] T. Ishii, M. Nakao, K. Suzuki, T. Enoki, R. Nishitani, and Y. Nishina, “Electronic properties of gold trichloride-graphite intercalation compounds ($AuCl_3$-GICs),” *Solid State Commun*, vol. 84, no. 11, pp. 1055–1059, Dec. 1992, doi: 10.1016/0038-1098(92)90439-G.

[97] A. C. Ferrari and J. Robertson, “Interpretation of Raman spectra of disordered and amorphous carbon,” *Phys Rev B*, vol. 61, no. 20, pp. 14095–14107, May 2000, doi: 10.1103/PhysRevB.61.14095.

[98] K. Takai *et al.*, “Structure and electronic properties of a nongraphitic disordered carbon system and its heat-treatment effects,” *Phys Rev B*, vol. 67, no. 21, p. 214202, Jun. 2003, doi: 10.1103/PhysRevB.67.214202.

[99] E. H. Martins Ferreira *et al.*, “Evolution of the Raman spectra from single-, few-, and many-layer graphene with increasing disorder,” *Phys Rev B*, vol. 82, no. 12, p. 125429, Sep. 2010, doi: 10.1103/PhysRevB.82.125429.

[100] A. Toyoda and T. Ando, “Theory of Electron Scattering by Lattice Defects in Monolayer Graphene,” *J Physical Soc Japan*, vol. 79, no. 9, p. 094708, Sep. 2010, doi: 10.1143/JPSJ.79.094708.

[101] Thorlabs, “Polymer Circular Polarizers (thorlabs.co.jp).” [Online].

Available: https://www.thorlabs.co.jp/newgrouppage9.cfm?objectgroup_id=10498

[102] S. Yoo and Q.-H. Park, “Polarimetric microscopy for optical control and high precision measurement of valley polarization,” *Review of Scientific Instruments*, vol. 89, no. 6, Jun. 2018, doi: 10.1063/1.5027517.

[103] S. Mignuzzi *et al.*, “Effect of disorder on Raman scattering of single-layer MoS_2,” *Phys Rev B*, vol. 91, no. 19, p. 195411, May 2015, doi: 10.1103/PhysRevB.91.195411.

[104] S. Tongay *et al.*, “Broad-Range Modulation of Light Emission in Two-Dimensional Semiconductors by Molecular Physisorption Gating,” *Nano Lett*, vol. 13, no. 6, pp. 2831–2836, Jun. 2013, doi: 10.1021/nl4011172.

[105] S. Mouri, Y. Miyauchi, and K. Matsuda, “Tunable Photoluminescence of Monolayer MoS_2 via Chemical Doping,” *Nano Lett*, vol. 13, no. 12, pp. 5944–5948, Dec. 2013, doi: 10.1021/nl403036h.

[106] J. A. Wilson, F. J. Di Salvo, and S. Mahajan, “Charge-density waves and superlattices in the metallic layered transition metal dichalcogenides,” *Adv Phys*, vol. 24, no. 2, pp. 117–201, Mar. 1975, doi: 10.1080/00018737500101391.

[107] K. Rossnagel, “On the origin of charge-density waves in select layered transition-metal dichalcogenides,” *Journal of Physics: Condensed Matter*, vol. 23, no. 21, p. 213001, Jun. 2011, doi: 10.1088/0953-8984/23/21/213001.

[108] D. Mihailovic, D. Svetin, I. Vaskivskyi, R. Venturini, B. Lipovšek, and A. Mraz, “Ultrafast non-thermal and thermal switching in charge configuration memory devices based on 1T-TaS_2,” *Appl Phys Lett*, vol. 119, no. 1, p. 013106, Jul. 2021, doi: 10.1063/5.0052311.

[109] G. Liu, B. Debnath, T. R. Pope, T. T. Salguero, R. K. Lake, and A. A. Balandin, “A charge-density-wave oscillator based on an integrated tantalum disulfide–boron nitride–graphene device operating at room temperature,” *Nat Nanotechnol*, vol. 11, no. 10, pp. 845–850, Oct. 2016, doi: 10.1038/nnano.2016.108.

[110] A. Mohammadzadeh, S. Baraghani, S. Yin, F. Kargar, J. P. Bird, and A. A. Balandin, “Evidence for a thermally driven charge-density-wave transition in 1T-TaS_2 thin-film devices: Prospects for GHz switching speed,” *Appl Phys Lett*, vol. 118, no. 9, Mar. 2021, doi: 10.1063/5.0044459.

[111] H. Xu *et al.*, “Properties of graphene-metal contacts probed by Raman spectroscopy,” *Carbon N Y*, vol. 127, pp. 491–497, Feb. 2018, doi: 10.1016/j.carbon.2017.11.035.

[112] B. H. Kim *et al.*, “N-type graphene induced by dissociative H_2 adsorption at room temperature,” *Sci Rep*, vol. 2, no. 1, p. 690, Sep. 2012, doi: 10.1038/srep00690.

[113] J.-H. Chen, L. Li, W. G. Cullen, E. D. Williams, and M. S. Fuhrer, “Tunable Kondo effect in graphene with defects,” *Nat Phys*, vol. 7, no. 7, pp. 535–538, Jul. 2011, doi: 10.1038/nphys1962.

[114] Q. G. Jiang, Z. M. Ao, W. T. Zheng, S. Li, and Q. Jiang, “Enhanced hydrogen sensing properties of graphene by introducing a mono-atom-vacancy,” *Physical Chemistry Chemical Physics*, vol. 15, no. 48, p. 21016, 2013, doi: 10.1039/c3cp52976b.

[115] A. Dużyńska *et al.*, “Temperature-induced phonon behavior in titanium disulfide (TiS_2) nanosheets,” *Journal of Raman Spectroscopy*, vol. 50, no. 8, pp. 1114–1119, Aug. 2019, doi: 10.1002/jrs.5637.

[116] J. R. Duffey, R. D. Kirby, and R. V. Coleman, “Raman scattering from 1T-TaS_2,” *Solid State Commun*, vol. 20, no. 6, pp. 617–621, Nov. 1976, doi: 10.1016/0038-1098(76)91073-5.

[117] H.-P. Komsa, J. Kotakoski, S. Kurasch, O. Lehtinen, U. Kaiser, and A. V. Krasheninnikov, “Two-Dimensional Transition Metal Dichalcogenides under Electron Irradiation: Defect Production and Doping,” *Phys Rev Lett*, vol. 109, no. 3, p. 035503, Jul. 2012, doi: 10.1103/PhysRevLett.109.035503.